

# **Qubit State Measurement Using a Microwave Photon Counter**

By

Alexander M. Opremcak

A dissertation submitted in partial fulfillment of  
the requirements for the degree of

Doctor of Philosophy  
(Physics)

at the

UNIVERSITY OF WISCONSIN-MADISON

2020

Date of final oral examination: 08/19/2020

The dissertation will hopefully be approved by the following members of the Final Oral Committee:

Robert F. McDermott, Professor, Physics

Victor W. Brar, Assistant Professor, Physics

Mark Saffman, Professor, Physics

Mikhail Kats, Assistant Professor, Electrical and Computer Engineering

Copyright © 2020  
by Alexander M. Opremcak

# Contents

<b>1</b>	<b>Superconducting Microwave Resonators</b>	<b>1</b>
1.1	External Loading Effects . . . . .	2
1.2	Photon Occupation Estimates . . . . .	10
1.3	Why $\kappa$ is not a Frequency . . . . .	12
1.4	The Classical Meaning of $g$ . . . . .	13
1.5	The ‘Purcell Effect’ for LC Circuits . . . . .	19
<b>2</b>	<b>Superconducting Quantum Circuits</b>	<b>23</b>
2.1	LC Circuit . . . . .	24
2.1.1	Driven LC Circuit . . . . .	26
2.2	Josephson Junctions . . . . .	28
2.3	Transmon . . . . .	31
2.3.1	Frequency Tunable Transmon . . . . .	36
2.4	Josephson Photomultiplier . . . . .	37
2.5	Dispersive Measurement Systems . . . . .	40
<b>3</b>	<b>JPM Experiment I</b>	<b>43</b>
3.1	Introduction . . . . .	44
3.2	Experimental Setup . . . . .	46
3.3	JPM Measurement Sequence . . . . .	49
3.4	Measurement Backaction and QNDness . . . . .	51
3.5	Conclusion . . . . .	53
<b>4</b>	<b>JPM Experiment II</b>	<b>57</b>
4.1	Introduction . . . . .	58
4.2	Circuit Design and Bring-up . . . . .	62
4.3	Pointer State Preparation . . . . .	68
4.4	Measurement Fidelity . . . . .	71
4.5	Backaction and Crosstalk . . . . .	74
4.6	Conclusion . . . . .	80

<b>A</b>	<b>Mathematical Derivations</b>	<b>83</b>
A.1	Introducing Branch Variables . . . . .	83
A.2	Hamiltonian for a Driven LC Circuit . . . . .	85
A.3	Hamiltonian for a Transmon . . . . .	87
A.4	From $\hat{Q}$ and $\hat{\Phi}$ to Pauli Matrices . . . . .	88
A.5	Resonant Drives and the RWA . . . . .	91
A.6	Dispersive Measurement Systems . . . . .	95
	A.6.1 Exact Solutions: the Eigenvalue Approach . . . . .	103
	A.6.2 Approximate Solutions: the Schrieffer–Wolff transformation . . . . .	110
<b>B</b>	<b>Supplementary Materials for JPM Experiment I</b>	<b>115</b>
B.1	JPM Theory . . . . .	115
B.2	JPM Fabrication . . . . .	117
B.3	Qubit Fabrication . . . . .	118
B.4	Experimental Setup . . . . .	118
B.5	Pointer State Transfer . . . . .	119
B.6	Window Functions for Pointer State Preparation . . . . .	122
B.7	Theoretical Detection Efficiency . . . . .	123
B.8	Estimates of Photon Occupation . . . . .	125
B.9	Tomography Fits . . . . .	126
<b>C</b>	<b>Supplementary Materials for JPM Experiment II</b>	<b>137</b>
C.1	Sample Fabrication . . . . .	137
C.2	Measurement Setup . . . . .	138
C.3	Stark Calibration . . . . .	139
C.4	Fidelity Budget . . . . .	140
C.5	JPM-Assisted Resonator and Qubit Reset . . . . .	143
	<b>Bibliography</b>	<b>147</b>

# Chapter 1

## Superconducting Microwave Resonators

Superconducting microwave resonators are critical elements in the design of any practical quantum circuit. These basic yet rich physical systems provide us with a testbed for studying topics such as dielectric and interface losses [1–4], nonequilibrium quasiparticles [5–7], two-level systems defects (TLS) [8, 9], and  $1/f$  magnetic flux noise [10]. In addition, microwave resonators form the basis of dispersive measurement systems – the most widely adopted and successful scheme for measuring the state of superconducting qubits. Finally, most of our intuition for superconducting qubits stems from our understanding of microwave resonators<sup>1</sup>, and not the other way around. It is for these reasons that I devote an entire chapter to the analysis of classical oscillators.

---

<sup>1</sup>Hereafter referred to as resonators, oscillators, or modes.

*May they continue to mystify generations of graduate students to come!*

This chapter begins with a brief review of the most common coupling schemes encountered when working with resonators. We show that for each of the coupling schemes considered, the system can be mapped onto an equivalent driven RLC circuit. From the differential equations governing the dynamics of these circuits, we derive expressions for the steady-state photon occupation in the resonator as a function of easily measured quantities. Lastly, we consider systems composed of coupled oscillators to show that both avoided level crossings and Purcell decay are purely classical phenomena.

## 1.1 External Loading Effects

When you couple a resonator to external circuitry, you change both its resonance frequency and quality factor, but by how much, and why? To understand these *loading effects*, we consider the circuits depicted in Fig. 1.1. In each of these systems, there is an ideal voltage source  $V_d(t)$  with an input impedance  $Z_0$  driving a resonator. In the absence of external coupling (i.e.  $C_d = M_d = 0$ ), the resonator is characterized by its capacitance  $C_r$ , inductance  $L_r$ , and internal resistance  $R_i$ . We define the internal quality factor of the resonator by

$$Q_i \equiv \omega_0 R_i C_r, \tag{1.1}$$

where  $\omega_0 = 1/\sqrt{L_r C_r}$  is the bare resonance frequency [11]. In addition, we define the impedance of the resonator by

$$Z_{\text{LC}} \equiv \sqrt{\frac{L_r}{C_r}} = \omega_0 L_r = \frac{1}{\omega_0 C_r}, \quad (1.2)$$

which is typically  $\sim 50 \Omega$  for standard coplanar waveguide (CPW) geometries [12, 13]. This value can increase substantially when the inductance per length is increased through the use of high kinetic inductance materials or Josephson junctions, which can improve or degrade the coupling quality factor as we will soon show.

The goal of this section is to describe methods for mapping the circuits shown in Fig. 1.1(a)-(e) onto equivalent driven RLC circuits which are described by linear second-order differential equations that can be solved algebraically. Armed with these expressions, we will then solve for the steady state current and voltage in the oscillator due to an applied resonant drive.

We begin with the circuit shown in Fig. 1.1(a). The most confusing part of this system is related to the coupled two-port network depicted in Fig. 1.2(a). In particular, how do we write down Kirchoff's laws without an explicit connection between circuit nodes? Using the definition of the impedance parameters, one can show that this network is equivalent to the circuit shown in Fig. 1.2(b). In this equivalent circuit, we have 'eliminated' the mutual inductance in favor of an explicit galvanic connection, which is often easier to think about and analyze. Applying this transformation to the circuit of interest (Fig. 1.1(a)), we arrive at the system shown in Fig. 1.2(c). Then,

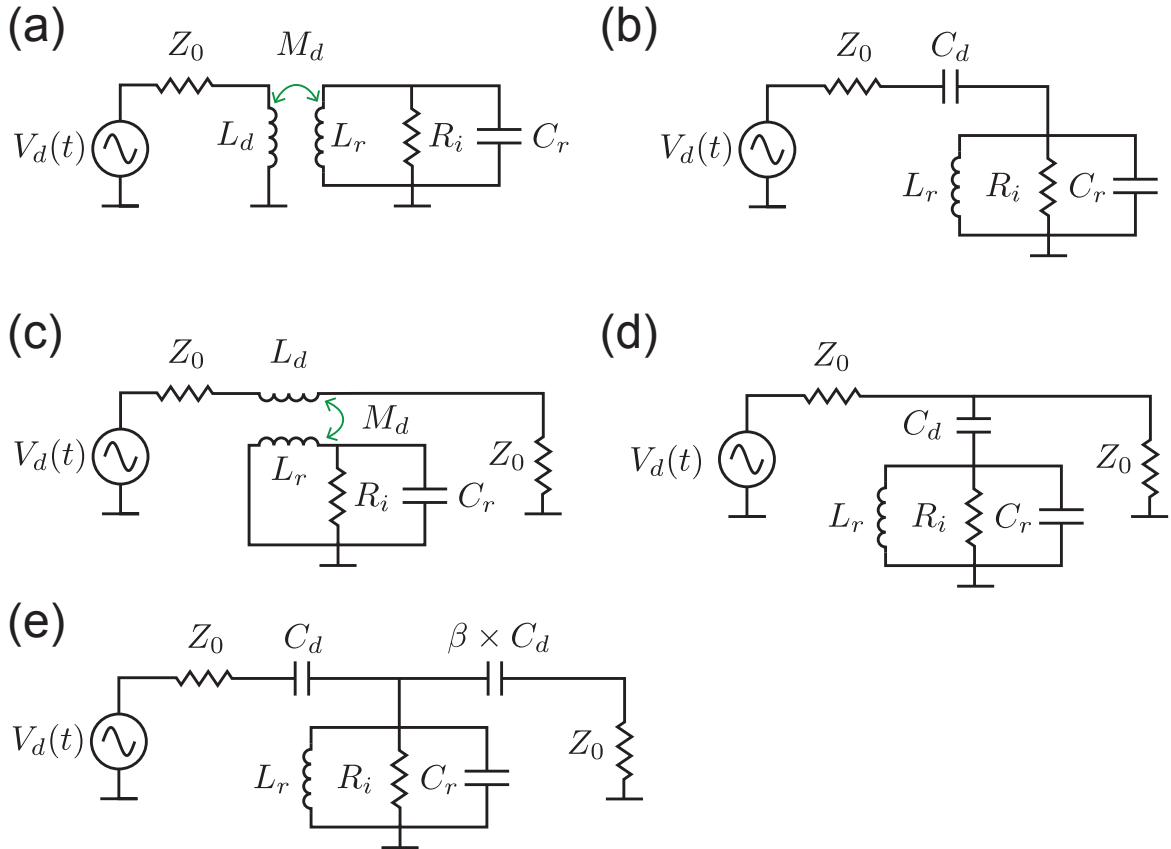


Figure 1.1: Common coupling schemes for microwave resonators. **(a)** An inductively driven RLC circuit coupled in reflection. **(b)** A capacitively driven RLC circuit coupled in reflection. **(c)** An inductively driven RLC circuit coupled to a feedline. **(d)** A capacitively driven RLC circuit coupled to a feedline. **(e)** A capacitively driven RLC tank circuit coupled in transmission.

by applying Kirchoff's Voltage Law (KVL) we obtain the system of equations below:

$$I_1 = \frac{V_d}{Z_0} \equiv I_d \quad (1.3)$$

$$(I_1 - I_2)Z_0 = j\omega_d(L_d - M_d)I_2 + j\omega_d M_d(I_2 - I_3) \quad (1.4)$$

$$j\omega_d M_d(I_2 - I_3) = j\omega_d(L_r - M_d)I_3 + R_i(I_3 - I_4) \quad (1.5)$$

$$R_i(I_3 - I_4) = \frac{1}{j\omega_d C_r} \times I_4. \quad (1.6)$$

Notice that we have replaced all derivatives (integrals) with  $j\omega_d$  ( $1/j\omega_d$ ), which is valid since we are interested in finding steady state solutions. Using Eq. (1.4), we solve for  $I_2$  in terms of the drive current  $I_d$  and the current through the inductor  $I_L \equiv I_3$  which yields the expression

$$I_2 = \frac{I_d Z_0 + j\omega_d M_d I_L}{j\omega_d L_d + Z_0} \simeq \left( I_d + \frac{j\omega M_d}{Z_0} I_L \right) \times \left( 1 - \frac{j\omega_d L_d}{Z_0} \right). \quad (1.7)$$

Similarly, using Eq. (1.6) we write  $I_4$  in terms of  $I_L$  as<sup>2</sup>

$$I_4 = \frac{R_i I_L}{R_i + \frac{1}{j\omega_d C_r}} \simeq I_L \left( 1 - \frac{1}{j\omega_d C_r R_i} - \frac{1}{(\omega_d C_r R_i)^2} \right).$$

We can rewrite the above expression as

$$R_i(I_L - I_4) = I_L \left( \frac{1}{j\omega_d C_r} + \frac{Z_{LC}^2}{R_i} \right). \quad (1.8)$$

Substituting Eqs. (1.7) and (1.8) into Eq. (1.5) yields

---

<sup>2</sup>Note that a first-order expansion in  $1/R_i$  would neglect internal loss mechanisms in later substitutions.

$$I_d \underbrace{\left( j\omega_d M_d + \frac{\omega_d^2 M_d L_d}{Z_0} \right)}_{\text{drive term}} = I_L \left( \underbrace{j\omega_d L_r + \frac{1}{j\omega_d C_r} + \frac{Z_{\text{LC}}^2}{R_i}}_{\text{uncoupled RLC Circuit}} + \underbrace{\frac{\omega_d^2 M_d^2}{Z_0}}_{\text{external loss}} - \underbrace{j \frac{\omega_d^3 M_d^2 L_d}{Z_0^2}}_{\text{frequency shift}} \right).$$

Neglecting the second portion of the drive term along with the small frequency shift<sup>3</sup>,

we arrive at the expression

$$I_L = I_d \frac{j\omega_d M_d}{j(\omega_d L_r - \frac{1}{\omega_d C_r}) + R_\Sigma}, \quad (1.9)$$

where

$$R_\Sigma = \omega_d^2 M_d^2 / Z_0 + Z_{\text{LC}}^2 / R_i. \quad (1.10)$$

We define the total quality factor of this circuit by

$$Q_{\text{tot}} \equiv \omega_d L_r / R_\Sigma = \begin{cases} \omega_d R_i C_r = Q_i & \text{as } M_d \rightarrow 0 \\ \left( \frac{L_r}{M_d} \right)^2 \left( \frac{Z_0}{Z_{\text{LC}}} \right) = Q_c & \text{as } R_i \rightarrow \infty. \end{cases} \quad (1.11)$$

Then, by setting  $\omega_d = \omega_0$  in Eq. (1.9), the magnitude of the current through the inductor is given by

$$\boxed{|I_L| = \frac{\omega_d M_d}{R_\Sigma} |I_d| = \left( \frac{M_d}{L_r} \right) \times Q_{\text{tot}} \times |I_d|}. \quad (1.12)$$

As a second example, consider the circuit shown in Fig. 1.1(b). Using the Thevenin-

---

<sup>3</sup>Assuming  $\omega_d/2\pi = 5$  GHz,  $M_d = 10$  pH,  $L_d = 500$  pH, and  $L_r = 1$  nH, we obtain a frequency shift  $\Delta\omega_0/2\pi \simeq 0.1$  MHz.

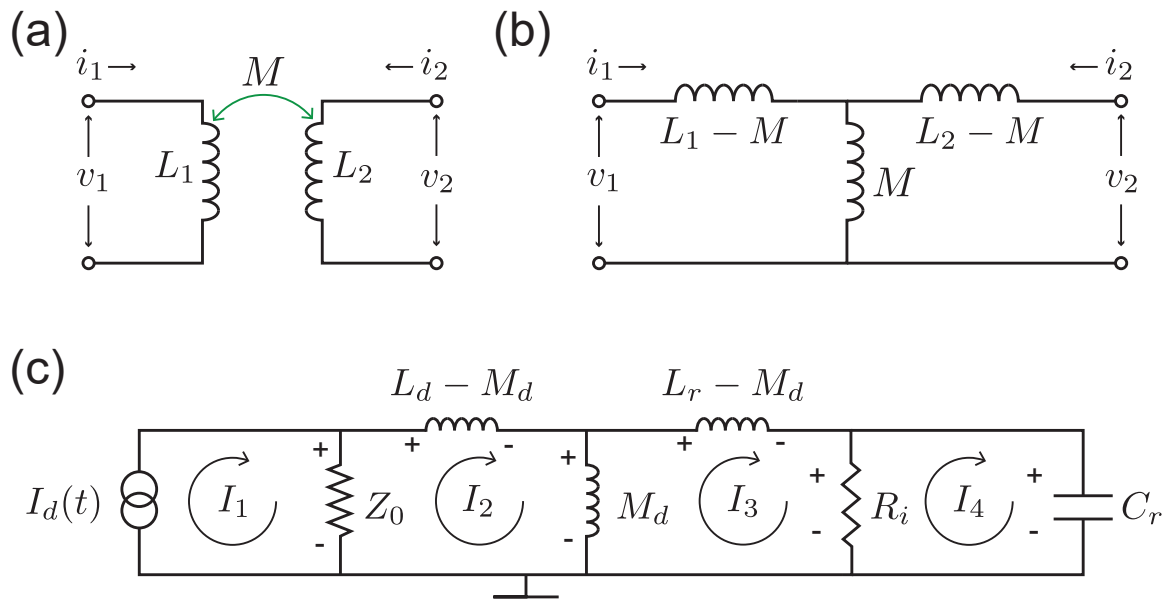


Figure 1.2: Circuit transformations for dealing with mutual inductance. **(a)** A coupled two-port network with self-inductances  $L_1$  and  $L_2$  coupled via mutual inductance  $M$ . **(b)** An equivalent circuit to part (a), but with galvanically coupled nodes. **(c)** The transformation from part (b) applied to the circuit depicted in Fig. 1.1(a). In addition, the voltage drive was transformed to a Norton equivalent current source  $I_d(t) = V_d(t)/Z_0$ .

to-Norton conversion, we replace the voltage source  $V_d$  in series with  $Z_0$  and  $C_d$  by an equivalent current source

$$I_d \equiv V_d/Z_{\text{branch}}$$

shunted by the branch impedance

$$Z_{\text{branch}^*} = Z_0 + 1/j\omega C_d.$$

Provided that  $Z_0 \ll 1/(\omega_d C_d)$ , one finds that

$$Y_{\text{branch}} = 1/Z_{\text{branch}} = \frac{j\omega C_d}{j\omega C_d Z_0 + 1} \simeq j\omega C_d + \underbrace{\frac{1}{(\omega C_d)^2 Z_0}}_{\equiv 1/R_d}. \quad (1.13)$$

This is (nearly) identical to the admittance of a capacitor  $C_d$  in parallel with a large frequency dependent resistance [14]. From current conservation

$$\begin{aligned} I_d &= \frac{V_C}{Z_{\text{branch}}} + \frac{1}{L_r} \int_{-\infty}^t V_C dt + j\omega_d C_r V_C + \frac{V_C}{R_i} \\ &\simeq j\omega_d (C_r + C_d) V_C + \frac{1}{L_r} \int_{-\infty}^t V_C dt + \frac{V_C}{R_{||}}, \end{aligned} \quad (1.14)$$

where

$$1/R_{||} = 1/R_i + (\omega_d C_d)^2 Z_0. \quad (1.15)$$

Noting that the current through the inductor  $I_L$  is related to the voltage across the capacitor  $V_C$  by

$$V_C = L_r \frac{dI_L}{dt},$$

we can rewrite Eq. (1.14) in terms of  $I_L$ . The result is that

$$\omega_0'^2 I_d = \left( \omega_0'^2 - \omega_d^2 + \frac{j\omega_d}{R_{\parallel} C_{\Sigma}} \right) I_L, \quad (1.16)$$

where  $C_{\Sigma} = C_r + C_d$  and  $\omega_0' \equiv 1/\sqrt{C_{\Sigma} L_r}$ <sup>4</sup>. For a resonant drive (i.e.  $\omega_d = \omega_0'$ ), the current through the inductor is given by

$$|I_L| = Q_{\text{tot}} |I_d| \simeq Q_{\text{tot}} \omega_0' C_d |V_d|, \quad (1.17)$$

where

$$\begin{aligned} Q_{\text{tot}} &\equiv \omega_0' R_{\parallel} C_{\Sigma} \\ &= \begin{cases} \omega_0 R_i C_r = Q_i & \text{as } C_d \rightarrow 0 \\ \left(\frac{C_{\Sigma}}{C_d}\right)^2 \left(\frac{Z'_{\text{LC}}}{Z_0}\right) = Q_c & \text{as } R_i \rightarrow \infty. \end{cases} \end{aligned} \quad (1.18)$$

In the above equation,  $Z'_{\text{LC}} = \sqrt{L_r/C_{\Sigma}}$ . Relating Eq. (1.17) to the voltage across the capacitor, one has that

$$\boxed{|V_C| = \omega_0' L_r |I_L| = \left(\frac{C_d}{C_{\Sigma}}\right) \times Q_{\text{tot}} \times |V_d|}. \quad (1.19)$$

Note the symmetry between Eqs. (1.12) and (1.19). We will use these expressions in the following section.

---

<sup>4</sup>The frequency shift due to a capacitive coupling cannot be ignored. Assuming  $\omega_d/2\pi = 5$  GHz,  $C_d = 10$  pF,  $C_r = 1$  pF, we find a frequency shift  $\Delta\omega_0/2\pi \simeq 25$  MHz.

## 1.2 Photon Occupation Estimates

The single photon power regime is important for characterizing the internal quality factor of a resonator at millikelvin temperatures [1, 15]. The reason is that the internal resistance  $R_i$  is never actually designed to be there – it is an effective resistance that models all other loss mechanisms in our distributed system (e.g. dielectric losses, quasiparticles, vortices, etc) – and varies strongly with applied drive power. So, if we plan on using the internal quality factors extracted from resonator measurements as a predictor of qubit performance, then we must do so at the single photon level. In addition, a typical dispersive measurement system operates with a few tens of photons in the resonator during a qubit measurement. However, when we are not measuring the qubit, we would like to shield the resonator from room-temperature electronic noise as much as possible. This is primarily accomplished using distributed attenuation, but how do we choose the right amount?

The following treatment is based on a semiclassical argument, and ignores many subtle effects (e.g., photon statistics, impedance mismatches, etc). Starting with the inductive case [see Fig. 1.1(a)], we can equate the energy stored in the inductor to the

number of photons in the resonator  $n_r$  multiplied by the photon energy as given below:

$$\begin{aligned}\hbar\omega_0 n_r &= \frac{1}{2} L_r |I_L|^2 = \frac{1}{2} \times \underbrace{\frac{Z_{\text{LC}}}{Z_0} \left(\frac{M_d}{L_r}\right)^2}_{=1/Q_c} \times Q_{\text{tot}}^2 \times \underbrace{|I_d|^2 Z_0 / \omega_0}_{=P_a} \\ &= \frac{1}{2} \frac{Q_{\text{tot}}^2}{Q_c} \times \frac{P_a}{\omega_0}.\end{aligned}$$

Rearranging this expression, one has that

$$\boxed{n_r = \frac{1}{2} \frac{Q_{\text{tot}}^2}{Q_c} \times \frac{P_a}{\hbar\omega_0^2}}. \quad (1.20)$$

Performing a similar calculation for the capacitive case [see Fig. 1.1(b)], one finds that

$$\begin{aligned}\hbar\omega'_0 n_r &= \frac{1}{2} C_\Sigma |V_C|^2 = \frac{1}{2} \times \underbrace{\frac{Z_0}{Z'_{\text{LC}}} \left(\frac{C_d}{C_\Sigma}\right)^2}_{=1/Q_c} \times Q_{\text{tot}}^2 \times \underbrace{|V_d|^2 / Z_0 / \omega'_0}_{=P_a} \\ &= \frac{1}{2} \frac{Q_{\text{tot}}^2}{Q_c} \times \frac{P_a}{\omega'_0}.\end{aligned}$$

This yields a nearly identical expression to Eq. (1.20), except for differences in the definitions of  $Q_{\text{tot}}$  and  $Q_c$  [compare Eqs. (1.11) and (1.18)]. In fact, the biggest difference overall stems from how  $Q_c$  scales with  $Z_{\text{LC}}/Z_0$ , which can be reasoned as follows. In the inductive case, it is the voltage drop induced by the resonator across the external bias circuitry that generates loss, and therefore the dissipated power  $P_{\text{diss}} = \langle V^2 \rangle / Z_0 = (\omega_0 M |I_L|)^2 / 2Z_0$ . Since the maximum energy stored in the inductor is given

by  $E_{\max} = L_r |I_L|^2 / 2$ , from the definition of the quality factor, we have that

$$Q_c = \omega_0 E_{\max} / P_{\text{diss}} = \left( \frac{Z_0}{Z_{\text{LC}}} \right) \left( \frac{L_r}{M_d} \right)^2 \propto Z_0. \quad (1.21)$$

In the capacitive case, it is the current flowing through  $Z_0$  that generates loss, which is determined by  $C_d$  alone, and is given by  $I = V_C / Z_{\text{branch}} \simeq \omega'_0 C_d |V_C|$ . This means that the power dissipated in the resistor  $P_{\text{diss}} = \langle I^2 \rangle Z_0 = (\omega'_0 C_d |V_C|)^2 Z_0 / 2$ . Since the maximum energy stored in the capacitor is given by  $E_{\max} = C_\Sigma |V_C|^2 / 2$ , we have that

$$Q_c = \omega'_0 E_{\max} / P_{\text{diss}} = \left( \frac{Z'_{\text{LC}}}{Z_0} \right) \left( \frac{C_\Sigma}{C_d} \right)^2 \propto \frac{1}{Z_0}. \quad (1.22)$$

Eqs. (1.21) and (1.22) are critical design formulas for qubits and resonators.

### 1.3 Why $\kappa$ is not a Frequency

The energy decay rate of a resonator, typically denoted by  $\kappa$ , is an important design parameter for dispersive measurement systems, as it influences both measurement speed and qubit coherence times. However, you will often see this quantity reported in terms of a frequency, angular frequency, or even an inverse timescale – so which one is correct? To understand where the ambiguity about  $\kappa$  comes from, we recall that a common definition of the quality factor is

$$Q \equiv \frac{\omega_0}{\Delta\omega}, \quad (1.23)$$

where  $\omega_0$  is the *angular* resonance frequency and  $\Delta\omega$  is the full width at half maximum (FWHM), if measured in units of energy [Fig. 1.3(a)]. Typically, when we talk about

$\kappa$ , we are directly referring to  $\Delta\omega$  (i.e.  $\kappa = \Delta\omega$ ). Therefore, if we want to report  $\kappa$  in terms of frequency measured in the laboratory, then we must remember to divide by a factor  $2\pi$  [Fig. 1.3(b)]. But this is still very confusing, because  $\kappa$  has little to do with oscillations, and is best described as an inverse timescale for the exponential decay of energy. In other words, a value of  $\kappa = 1/(100 \text{ ns})$  leads to a  $1/e$  loss of energy stored in the resonator during free decay in 100 ns [Fig. 1.3(c)]. At any rate, we often quote the bandwidth of a resonator in terms of  $\kappa$ , so watch out for factors of  $2\pi$ .

## 1.4 The Classical Meaning of $g$

Coupled harmonic oscillators exhibit many of the same behaviors that qubit-resonator and qubit-qubit systems do, but can be analyzed using simple algebraic techniques. In what follows, we will derive expressions for the coupling strength  $g$  between capacitively (and inductively) coupled LC circuits. Consider the circuit shown in Fig. 1.4(a) with *bare* resonance frequencies  $\omega_1 = 1/\sqrt{L_1C_1}$  and  $\omega_2 = 1/\sqrt{L_2C_2}$ . The equations of motion for this system are

$$j\omega(C_1 + C_g)V_1 + \frac{V_1}{j\omega L_1} - j\omega C_g V_2 = 0 \quad (1.24)$$

$$j\omega(C_2 + C_g)V_2 + \frac{V_2}{j\omega L_2} - j\omega C_g V_1 = 0. \quad (1.25)$$

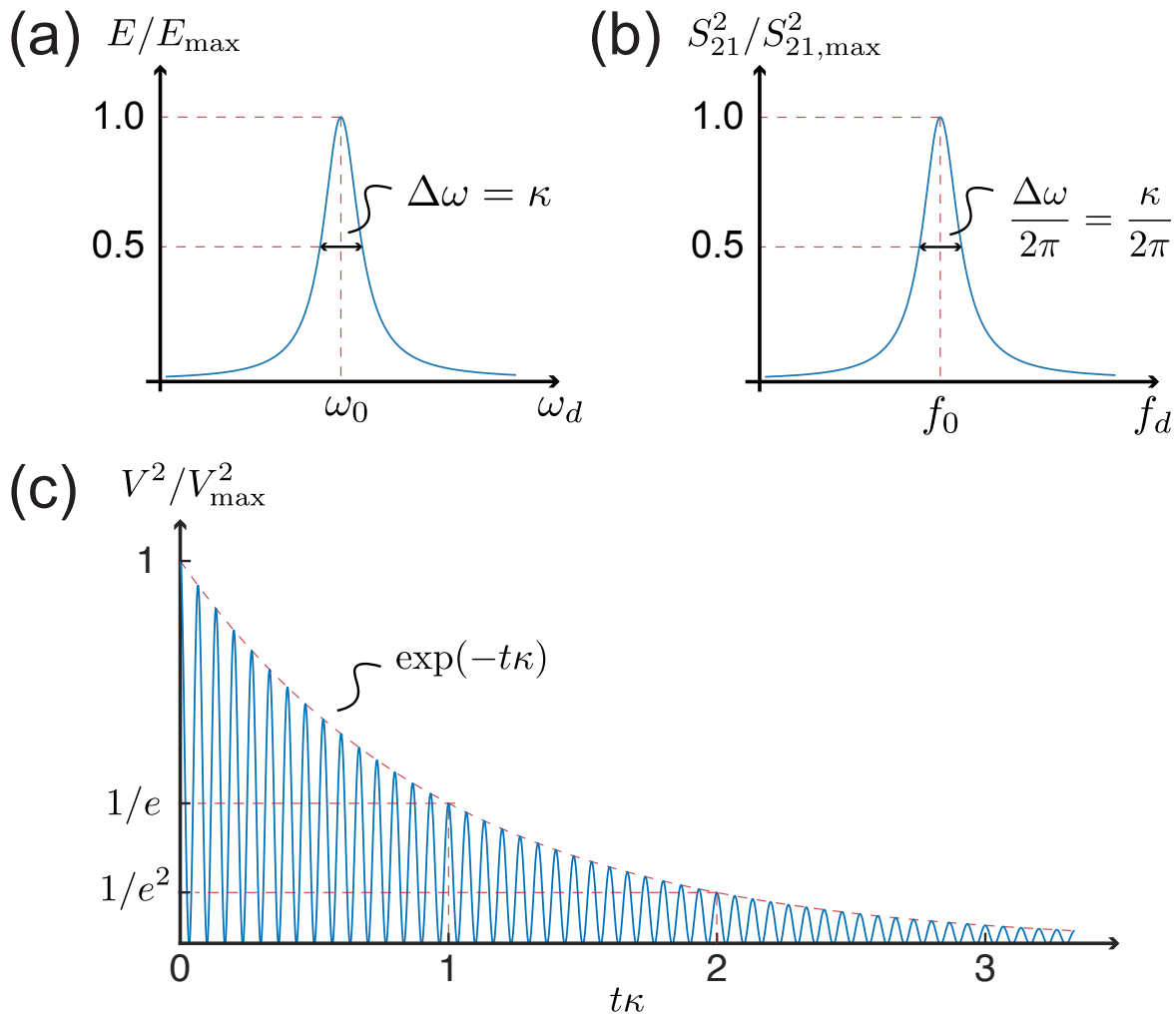


Figure 1.3: The multiple meanings of  $\kappa$ . (a) The steady state energy stored in the resonator as function of the *angular* drive frequency  $\omega_d$ . The FWHM  $\Delta\omega$  is defined as the *angular* bandwidth over which the stored energy is greater than half the value on resonance. Under this definition  $\Delta\omega = \kappa$ . (b) The energy response of a resonator measured with the scattering parameter  $S_{21}$  in the laboratory versus drive frequency  $f_d$ . When measured in units of Hertz, the FWHM is given by  $\kappa/2\pi$ . This is particularly critical for comparisons of  $\kappa$  with the dispersive shift, where factors  $\sim 2\pi$  will lead to a grossly inefficient readout systems. (c) Free decay of energy stored in the resonator. The exponential decay of  $V^2$  occurs with a characteristic timescale of  $1/\kappa$ . The same holds during resonator ring-up – the transients decay with characteristic timescale of  $1/\kappa$ .

Introducing the notation  $\beta_i = C_g/(C_i + C_g)$  (where  $\beta_i \ll 1$ ) and identifying the new resonance frequencies  $\omega'_i = 1/\sqrt{L_i(C_i + C_g)}$ , the equations of motion can be written in matrix form as

$$\begin{bmatrix} \omega_1'^2 - \omega^2 & \omega^2 \beta_1 \\ \omega^2 \beta_2 & \omega_2'^2 - \omega^2 \end{bmatrix} \begin{bmatrix} V_1 \\ V_2 \end{bmatrix} = \begin{bmatrix} 0 \\ 0 \end{bmatrix}. \quad (1.26)$$

Setting the determinant of this 2 x 2 matrix to zero yields the eigenfrequencies

$$\omega_{\pm} = \sqrt{\frac{(\omega_1'^2 + \omega_2'^2) \pm \sqrt{(\omega_1'^2 - \omega_2'^2)^2 + 4\omega_1'^2 \omega_2'^2 \beta_1 \beta_2}}{2(1 - \beta_1 \beta_2)}}, \quad (1.27)$$

which is a bit too complicated to remember. However, if we set  $\omega_1' = \omega_2' = \omega_0$  we find that

$$\omega_{\pm} \simeq \omega_0 \sqrt{1 \pm \sqrt{\beta_1 \beta_2}} \simeq \omega_0 \pm \frac{\omega_0}{2} \underbrace{\frac{C_c}{\sqrt{(C_1 + C_g)(C_2 + C_g)}}}_{=g}. \quad (1.28)$$

We will arrive a very similar expression for the coupling strength between a qubit and resonator in our study of dispersive measurement systems. A plot of the eigenfrequencies from Eq. (1.27) is shown in Fig. 1.5(a) using the parameters listed in Table 1.1. We note that avoided level crossings correspond to the resonant energy transfer between modes #1 and #2 in the time domain with a beat period of  $\pi/g$ .

Table 1.1: Avoided Level Crossing Parameters

Variable	Value
$\omega_1/2\pi$	5 GHz
$\omega_2/2\pi$	$\in (4.0, 6.0) \times \text{GHz}$
$\beta_1$	0.05
$\beta_2$	0.05

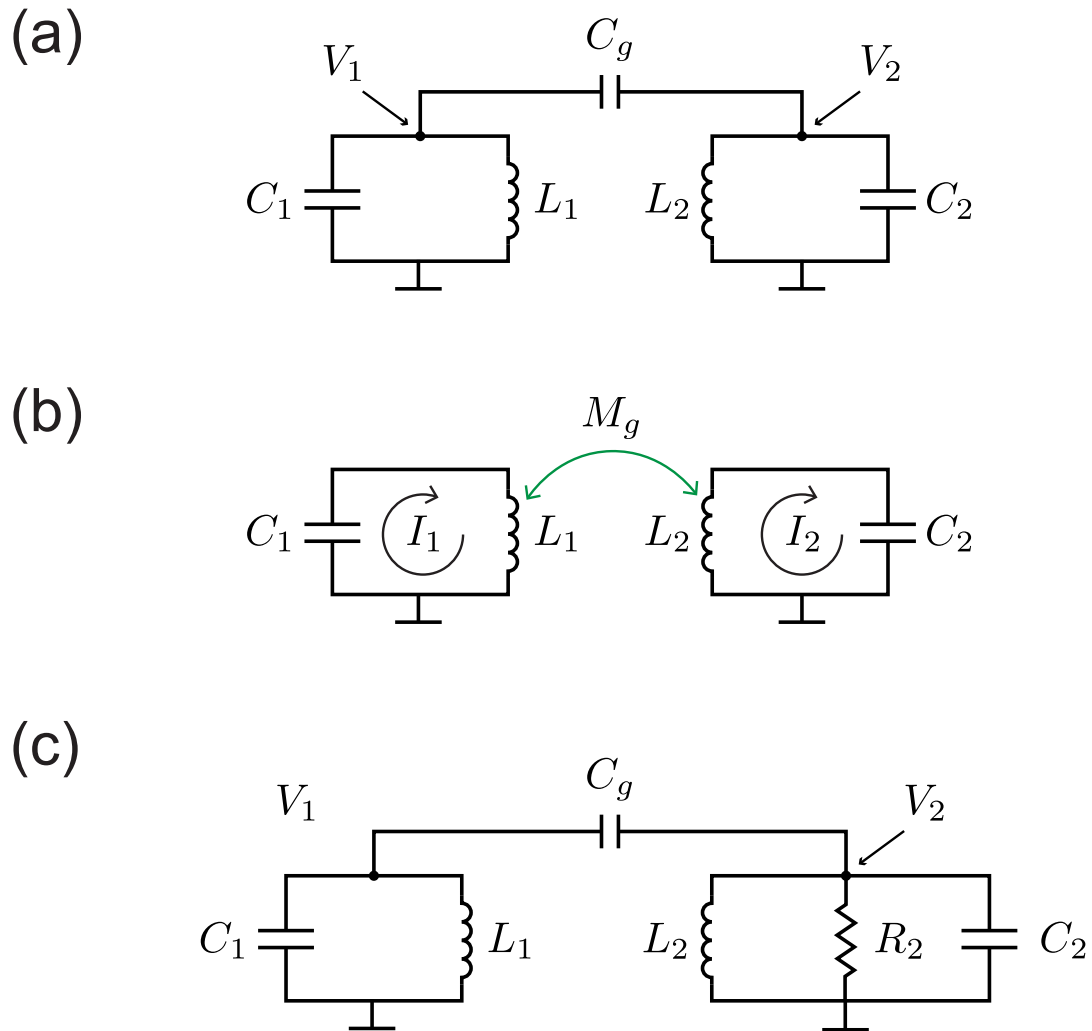


Figure 1.4: Common coupling schemes for oscillators. (a) Capacitively coupled LC circuits, coupled via series capacitance  $C_g$  with node voltages  $V_1$  and  $V_2$ . (b) Inductively coupled LC circuits, coupled via mutual inductance  $M_g$  with loop currents  $I_1$  and  $I_2$ . (c) As in part (a), but with an internal shunt resistance  $R_2$  added to mode #2.

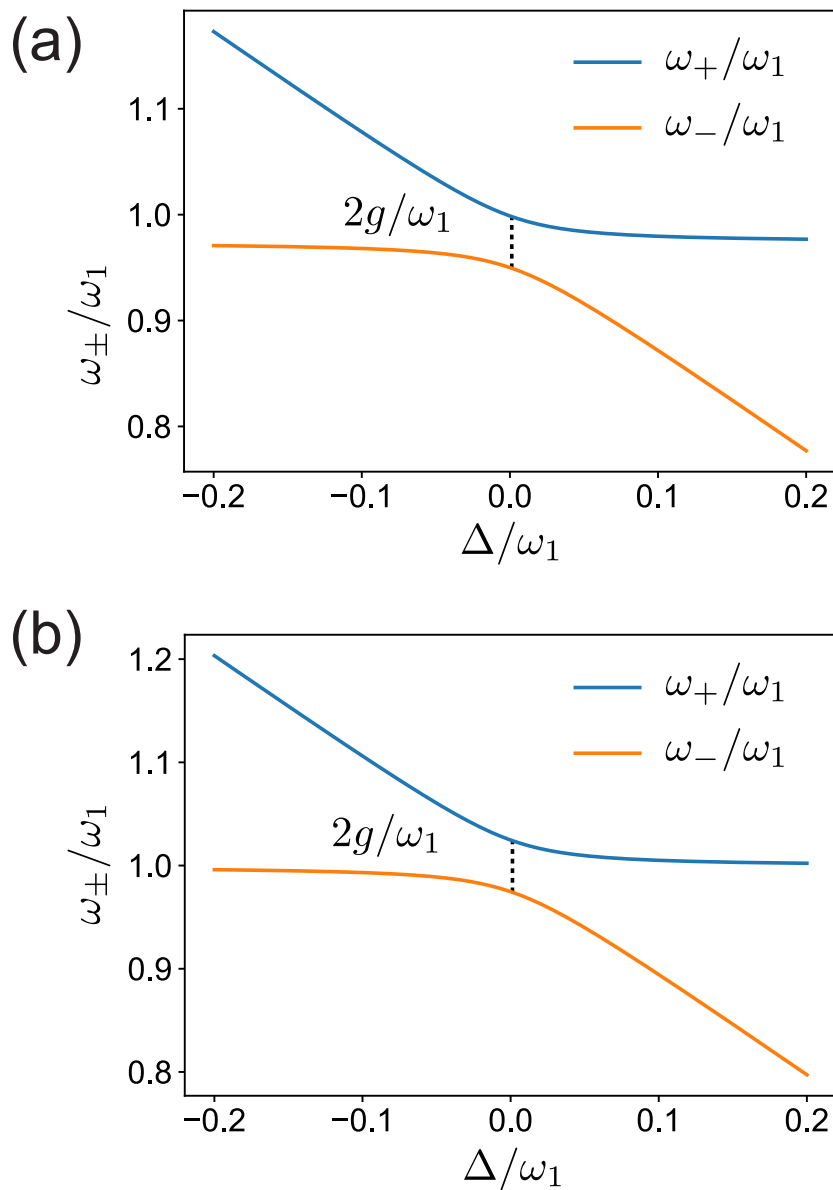


Figure 1.5: Avoided level crossings for coupled LC circuits. **(a)** Eigenfrequencies for capacitively coupled LC circuits [Eq. (1.27)] plotted versus the detuning  $\Delta = \omega_1 - \omega_2$ . All axes in are normalized by the bare resonance frequency  $\omega_1 = 1/\sqrt{L_1 C_1}$ . At large detunings, both modes decouple and tend to the shifted resonance frequencies  $\omega'_1$  and  $\omega'_2$ . **(b)** Eigenfrequencies for inductively coupled LC circuits [Eq. (1.32)] versus detuning. At large detunings, both modes decouple, but tend to the bare resonance frequencies  $\omega_1$  and  $\omega_2$ . At intermediate detunings, the modes repel by approximately  $g^2/\Delta$ .

The analogous system with a mutual inductive coupling is given in Fig. 1.4(b). Making use of the transformation described in Fig. 1.2 (a)-(b), we arrive at the equations of motion

$$\frac{I_1}{j\omega C_1} + j\omega L_1 I_1 - j\omega M_g I_2 = 0 \quad (1.29)$$

$$\frac{I_2}{j\omega C_2} + j\omega L_2 I_2 - j\omega M_g I_1 = 0. \quad (1.30)$$

Multiplying Eq. (1.29) by  $j\omega/L_1$  [and Eq. (1.30) by  $j\omega/L_2$ ], we find that

$$\begin{bmatrix} \omega^2 - \omega_1^2 & -\omega^2 \beta_1 \\ -\omega^2 \beta_2 & \omega^2 - \omega_2^2 \end{bmatrix} \begin{bmatrix} I_1 \\ I_2 \end{bmatrix} = \begin{bmatrix} 0 \\ 0 \end{bmatrix}, \quad (1.31)$$

where  $\beta_i = M_g/L_i$  and  $\omega_i = 1/\sqrt{L_i C_i}$ . Setting the determinant of this 2 x 2 matrix to zero yields the eigenfrequencies

$$\omega_{\pm} = \sqrt{\frac{(\omega_1^2 + \omega_2^2) \pm \sqrt{(\omega_1^2 - \omega_2^2)^2 + 4\omega_1^2 \omega_2^2 \beta_1 \beta_2}}{2(1 - \beta_1 \beta_2)}}, \quad (1.32)$$

which is again too cumbersome to be useful. However, by setting  $\omega_1 = \omega_2 = \omega_0$  and neglecting terms  $\mathcal{O}(\beta^2)$ , one has that

$$\omega_{\pm} \simeq \omega_0 \pm \underbrace{\frac{\omega_0}{2} \frac{M_g}{\sqrt{L_1 L_2}}}_{=g}. \quad (1.33)$$

A plot of the eigenfrequencies from Eq. (1.32) are shown in Fig. 1.5(b) using the parameters reported in Table 1.1.

## 1.5 The ‘Purcell Effect’ for LC Circuits

Our estimates of loaded quality factors discussed in Section 1.1 can be summarized in a useful and compact form as

$$T_{1,r} = \frac{C_\Sigma}{\text{Re}\{Y(\omega_0)\}}, \quad (1.34)$$

where  $C_\Sigma$  is the total capacitance of resonator,  $T_{1,r} = Q_{\text{tot}}/\omega_0$  is the resonator’s energy relaxation time, and  $Y(\omega_0)$  is the admittance of the resonator evaluated its resonance frequency [16]. While this formula may not be screaming to you at the moment, it is extremely helpful when the load resistor  $Z_0$  (see Fig 1.1) is replaced by something more complicated (e.g. a resonant circuit, filter, qubit, etc). In what follows, we will use this formula to derive the ‘Purcell effect’ for the system of coupled oscillators depicted in Fig. 1.4(c). Here, we have a lossless oscillator (denoted with subscript 1) coupled to an oscillator with damping (denoted with subscript 2). We would like to understand how the decay rate of the ‘lossless’ oscillator depends on the coupling strength, detuning, and decay rate of the damped mode. We assume that  $C_1, C_2 \gg C_g$  and  $Z_{\text{LC},2} = \sqrt{L_2/C_2} \gg R_2$ , as these are the limits relevant to a dispersive measurement system.

Starting with the admittance of the undamped resonator to ground, one finds that

$$Y(\omega'_1) = \frac{1}{\frac{1}{j\omega'_1 C_g} + \frac{1}{1/R_2 + 2jC_2\bar{\omega}\Delta/\omega'_1}}, \quad (1.35)$$

where  $\Delta = \omega'_1 - \omega_2$  and  $\bar{\omega} = (\omega'_1 + \omega_2)/2$ . Since we are only interested in the real part

of  $Y(\omega'_1)$ , it pays to rearrange this expression as below:

$$\begin{aligned}
Y(\omega'_1) &= \frac{j\omega'_1 C_g \times (1/R_2 + 2jC_2\bar{\omega}\Delta/\omega'_1)}{1/R_2 + j(\omega'_1 C_g + 2C_2\bar{\omega}\Delta/\omega'_1)} \\
&= \frac{j\omega'_1 C_g \times (1/R_2 + 2jC_2\bar{\omega}\Delta/\omega'_1)}{1/R_2 + j(\omega'_1 C_g + 2C_2\bar{\omega}\Delta/\omega'_1)} \times \frac{1/R_2 - j(\omega'_1 C_g + 2C_2\bar{\omega}\Delta/\omega'_1)}{1/R_2 - j(\omega'_1 C_g + 2C_2\bar{\omega}\Delta/\omega'_1)} \\
&\simeq \frac{\omega_1'^2 C_g^2 / R_2}{4C_2^2 \bar{\omega}^2 \Delta^2 / \omega_1'^2} + \text{imaginary terms.}
\end{aligned} \tag{1.36}$$

Plugging Eq. (1.36) into Eq. (1.34) yields the result

$$T_{1,r} \simeq \left(\frac{\Delta^2}{g^2}\right) \left(\frac{1}{\kappa_2}\right) \times \left(\frac{\omega_2 \bar{\omega}^2}{\omega_1'^3}\right), \tag{1.37}$$

where

$$g = \sqrt{\omega_1' \omega_2} \frac{C_g}{2\sqrt{C_\Sigma C_2}}$$

and

$$\kappa_2 = 1/R_2 C_2.$$

Eq. (1.37) closely resembles the celebrated Purcell formula for qubits:  $T_{1,q} \leq (\Delta/g)^2/\kappa$  [17]. In Fig. 1.6, we analyze the accuracy of this approximation for the parameters listed in Table 1.2. Interestingly, we find that Purcell decay is significantly worse at positive detunings using a single mode approximation for the resonator<sup>5</sup>. This is primarily due to the frequency dependent impedance of the coupling capacitor  $C_g$ , which regulates the flow of current from the lossless mode into the damped mode's

---

<sup>5</sup>Typically, our resonators are constructed using coplanar waveguides which support higher harmonics, leading to additional Purcell decay as discussed by Houck *et al.* [17].

resistor.

Table 1.2: Purcell Decay Parameters

Variable	Value
$\omega'_1/2\pi$	$\in (3.5, 6.5) \times \text{GHz}$
$\omega'_2/2\pi$	5.0 GHz
$C_g$	10 fF
$C_1 + C_g$	100 fF
$C_2 + C_g$	1 pF
$R_2$	100 k $\Omega$

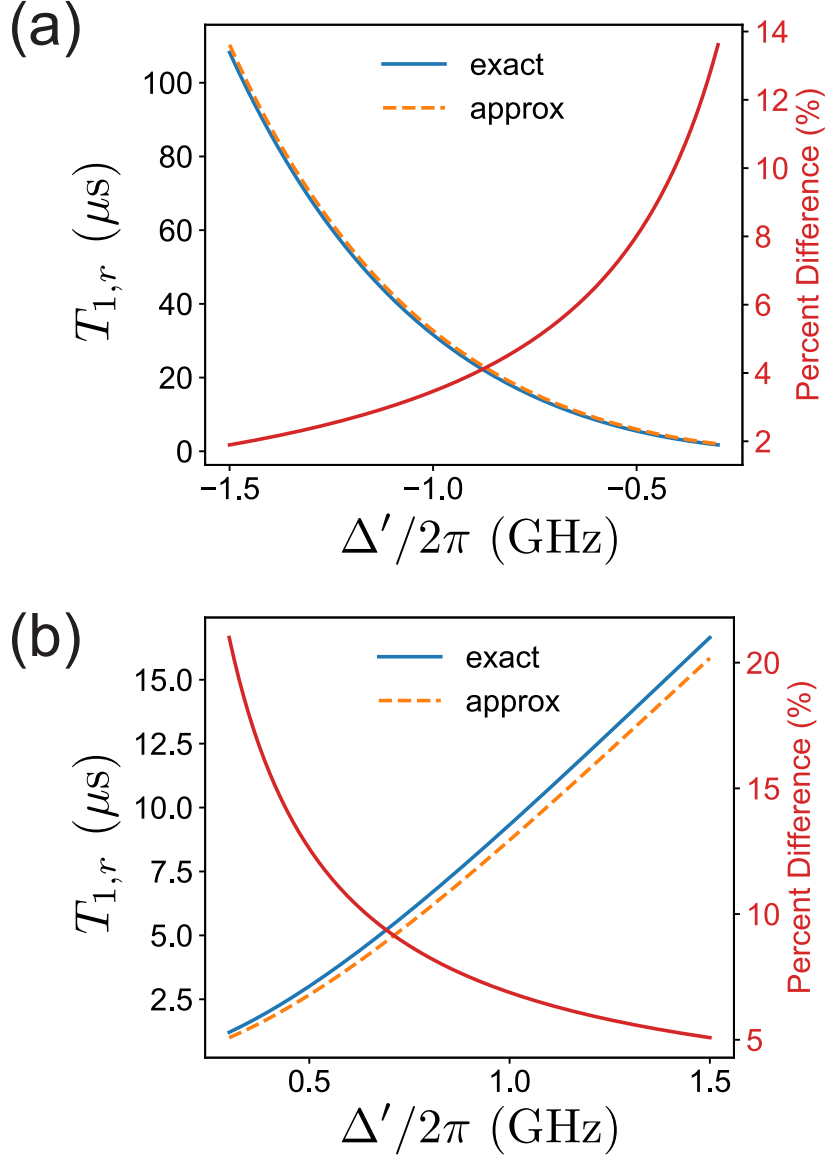


Figure 1.6: Classical Purcell decay. (a) A comparison of the exact [Eq. (1.34)] and approximate [Eq. (1.37)] expressions for the Purcell relaxation time plotted versus the detuning  $\Delta' = \omega'_1 - \omega'_2$ . The parameters used in these plots are listed in Table 1.2, and are representative of a typical dispersive measurement system. We find that the accuracy of our approximation is within 10% of the exact expression for detunings  $|\Delta| > 0.5$  GHz.

## Chapter 2

# Superconducting Quantum Circuits

This chapter is a review of the basic device physics needed to understand superconducting transmon qubits, Josephson Photomultipliers (JPM), and dispersive measurement systems. It begins with a study of the simple  $LC$  oscillator to demonstrate methods for quantizing superconducting electrical circuits in a familiar system. We then introduce Josephson junctions into our circuits to derive Hamiltonians for the transmon and JPM. Finally, we analyze coupled transmon-resonator systems to derive the Jaynes-Cummings Hamiltonian in the dispersive approximation.

## 2.1 LC Circuit

Using the definition of branch flux introduced in Appendix A.1, the current conservation equation for the circuit depicted in Fig. 2.1(a) can be written as

$$0 = \underbrace{C_r \ddot{\Phi}}_{\text{current into } C_r} + \underbrace{\dot{\Phi}/L_r}_{\text{current into } L_r}, \quad (2.1)$$

where  $\Phi = \int_{-\infty}^t V(t') dt'$ . Identifying  $\Phi$  with ‘position’ and  $\dot{\Phi}$  with ‘velocity’, the Lagrangian that reproduces Eq. (2.1) is

$$\mathcal{L}(\Phi, \dot{\Phi}) = \underbrace{\frac{C_r \dot{\Phi}^2}{2}}_{\text{kinetic}} - \underbrace{\frac{\Phi^2}{2L_r}}_{\text{potential}}, \quad (2.2)$$

by assuming the Euler-Lagrange equation

$$\frac{d}{dt} \frac{\partial \mathcal{L}}{\partial \dot{\Phi}} = \frac{\partial \mathcal{L}}{\partial \Phi}. \quad (2.3)$$

The ‘momentum’ conjugate to  $\Phi$  is defined as

$$\frac{\partial \mathcal{L}}{\partial \dot{\Phi}} = C_r \dot{\Phi} = C_r V.$$

Notice that  $C_r V$  is simply the charge  $Q$  stored on the capacitor plate, and therefore that  $\Phi$  and  $Q$  are the conjugate variables for this system, with  $Q$  serving as the ‘momentum’.

From the definition of the Hamiltonian, one finds that

$$H(\Phi, Q) = Q \dot{\Phi} - \mathcal{L} = \frac{Q^2}{2C_r} + \frac{\Phi^2}{2L_r}, \quad (2.4)$$

which is the sum of the capacitive and inductive energies (i.e. the total energy of the system).

To quantize this circuit, we promote  $\Phi$  and  $Q$  to operators and impose the canonical

commutation relation

$$[\hat{\Phi}, \hat{Q}] = i\hbar. \quad (2.5)$$

Under these substitutions, the Hamiltonian becomes an operator of the form

$$\hat{H} = \frac{\hat{Q}^2}{2C_r} + \frac{\hat{\Phi}^2}{2L_r}, \quad (2.6)$$

which can be written in terms of raising and lowering operators as

$$\hat{H} = \hbar\omega_0(\hat{a}^\dagger\hat{a} + 1/2), \quad (2.7)$$

where  $\omega_0 = 1/\sqrt{L_r C_r}$  is the resonance frequency with  $\hat{a}$  and  $\hat{a}^\dagger$  defined implicitly

below<sup>1</sup>:

$$\hat{\Phi} = \Phi_{\text{zpf}}(\hat{a} + \hat{a}^\dagger) \quad (2.8)$$

$$\hat{Q} = iQ_{\text{zpf}}(\hat{a}^\dagger - \hat{a}) \quad (2.9)$$

$$\Phi_{\text{zpf}} = \sqrt{\frac{\hbar\omega_0 L_r}{2}} = \sqrt{\frac{\hbar Z_{\text{LC}}}{2}} \quad (2.10)$$

$$Q_{\text{zpf}} = \sqrt{\frac{\hbar\omega_0 C_r}{2}} = \sqrt{\frac{\hbar}{2Z_{\text{LC}}}}. \quad (2.11)$$

Here,  $\Phi_{\text{zpf}}$  and  $Q_{\text{zpf}}$  are the zero point fluctuations of flux and charge, respectively <sup>2</sup>.

---

<sup>1</sup>To derive these expressions for yourself, assume that  $\hat{a} = c_1\hat{\Phi} + ic_2\hat{Q}$  and  $\hat{a}^\dagger = c_1\hat{\Phi} - ic_2\hat{Q}$  where  $c_1, c_2$  are real. By imposing Eq. (2.5), one arrives at Eqs. (2.8)-(2.11). One can easily verify that  $[\hat{a}, \hat{a}^\dagger] = 1$ .

<sup>2</sup>To remember the expression for  $\Phi_{\text{zpf}}$ , simply equate the inductive energy term  $\Phi^2/2L_r$  with one-half of the zero-point energy of the oscillator (i.e.,  $\hbar\omega_0/4$ ) and solve for  $\Phi$ . The analogous procedure holds for deriving  $Q_{\text{zpf}}$ .

The energy level structure for this system is

$$\langle n | \hat{H} | n \rangle = E_n = \hbar\omega_0(n + 1/2), \quad (2.12)$$

where  $|n\rangle$  is the Fock state corresponding to  $n$  excitations<sup>3</sup> in the resonator. A flux basis representation of the wavefunctions for this system is shown Fig. 2.1(c) using the parameters from rows 1-2 of Table 2.1.

Table 2.1: Comparing  $LC$  circuits with transmons

Variable	Value
$C_r$	64.5 fF
$L_r$	8.2 nH
$C_{xy}$	0
$E_C/h$	300 MHz
$E_J/h$	20 GHz
$C_q = e^2/(2E_C)$	64.5 fF
$L_q = (\frac{\Phi_0}{2\pi})^2/(E_J)$	8.2 nH

### 2.1.1 Driven LC Circuit

Using similar methods to Section 2.1, the Hamiltonian for the driven  $LC$  circuit depicted in Fig. 2.1(b) can be written as

$$\hat{H} = \frac{\hat{Q}^2}{2C_\Sigma} + \frac{\hat{\Phi}^2}{2L_r} + \frac{C_d}{C_\Sigma} \hat{Q} V_d(t), \quad (2.13)$$

where  $C_\Sigma \equiv C_d + C_r$  (see Appendix A.2 for further detail). This is nearly identical to the Hamiltonian from Eq. (2.6), but with a shifted resonance frequency  $\omega'_0 = 1/\sqrt{L_r C_\Sigma}$

---

<sup>3</sup>We often refer to these excitations as microwave photons since  $\omega_0/2\pi$  lies in the microwave frequency range.

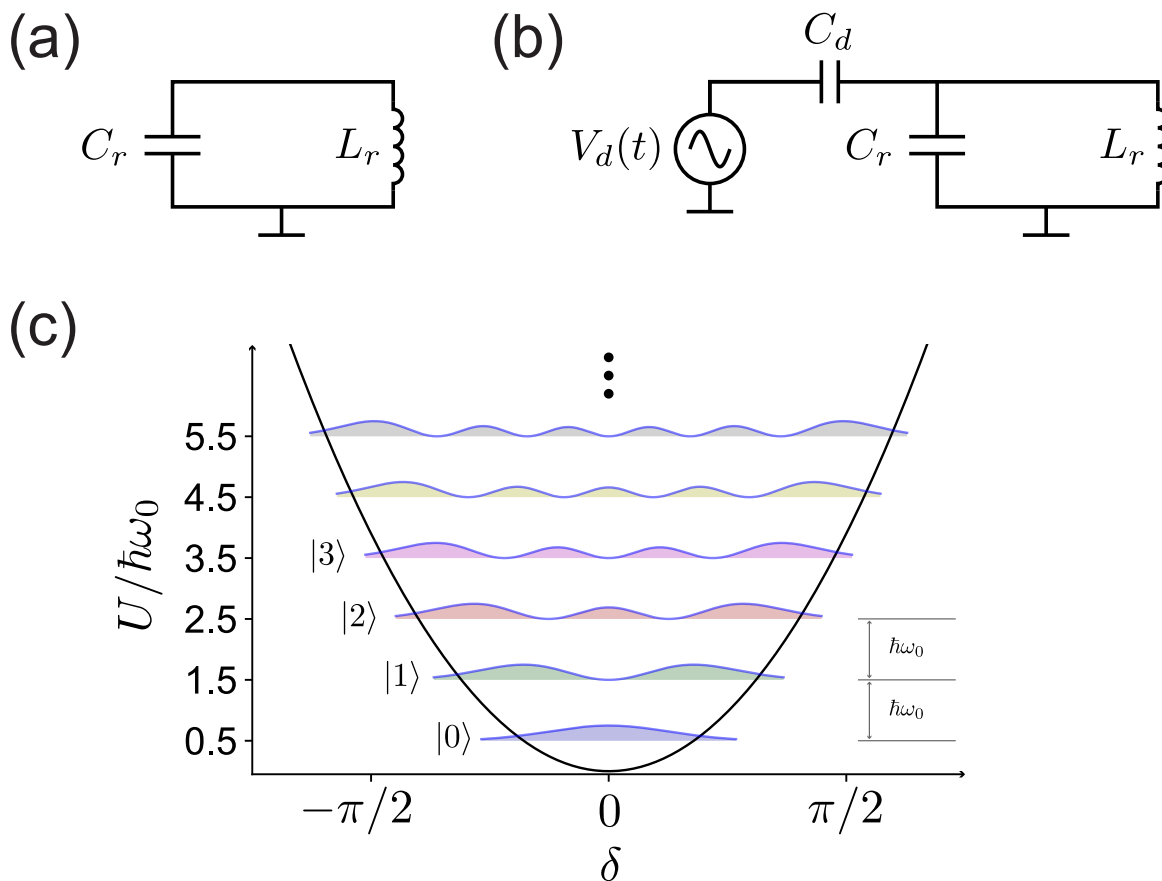


Figure 2.1: The quantum  $LC$  circuit. (a) An isolated  $LC$  circuit with capacitance  $C_r$  and inductance  $L_r$ . (b) As in part (a), but with a drive source  $V_d(t)$  coupled to the oscillator via the capacitance  $C_d$ . (c) A flux basis representation of the wavefunction probabilities for an  $LC$  with the parameters listed in Table 2.1. We plot these wavefunctions versus the ‘dimensionless flux’  $\delta = 2\pi\Phi/\Phi_0$  for a comparison with the transmon’s wavefunctions in Section 2.3.

plus a drive term

$$\hat{H}_d(t) = \frac{C_d}{C_\Sigma} \hat{Q} V_d(t). \quad (2.14)$$

Treating the drive term as a small perturbation, we see from Eq. (2.9) that  $\hat{H}_d(t) \propto \hat{Q}$  couples the states  $|n\rangle$  and  $|n-1\rangle$ , and is therefore capable of creating (and removing) excitations in the resonator, as expected for a drive source. Interestingly, a resonant drive of the form  $V_d(t) = |V_d| \cos(\omega'_0 t)$  produces a coherent state

$$|\alpha_r\rangle = \exp(-|\alpha_r|^2/2) \sum_{n=0}^{\infty} \frac{\alpha_r^n}{\sqrt{n!}} |n\rangle$$

inside the resonator [18, 19], with an average number of photons

$$\bar{n}_r = |\alpha_r|^2.$$

We note that, in practice, it is quite challenging to prepare even small superpositions of Fock states, and we refer the interested reader to the beautiful set of experiments performed by Hofheinz *et al.* [20, 21] for further information about this topic.

## 2.2 Josephson Junctions

The Josephson relations state that the supercurrent  $I$  flowing through a junction and the voltage difference  $V$  across the junction are governed by the equations [22–24]

$$I = I_0 \sin \delta \quad (2.15)$$

$$V = \frac{\Phi_0}{2\pi} \frac{d\delta}{dt}, \quad (2.16)$$

where  $I_0$  is the junction's critical current,  $\delta$  is the superconducting phase difference across the junction,  $\Phi_0 \equiv h/2e$  is the magnetic flux quantum. Taking the time derivative of Eq. (2.15) yields the expression

$$\frac{dI}{dt} = I_0 \cos \delta \times \frac{d\delta}{dt},$$

which, by Eq. (2.16), implies that

$$V = \frac{\Phi_0}{2\pi I_0 \cos \delta} \times \frac{dI}{dt}.$$

This is quite similar to the formula for the voltage drop across an inductor if we define the Josephson inductance as

$$L_J(\delta) = \frac{\Phi_0}{2\pi I_0 \cos \delta}. \quad (2.17)$$

However, notice here that  $L_J(\delta)$  is a function of the current through the junction by Eq. (2.15). This is why Josephson junctions are often referred to as *nonlinear* inductors.

We can evaluate the energy absorbed by this element using the Eq. (A.5), which yields<sup>4</sup>

$$\begin{aligned}
 U(\delta) &= \int_{-\infty}^t I(t')V(t')dt' \\
 &= \frac{\Phi_0}{2\pi} \int_{-\infty}^t I_0 \sin \delta' \times \frac{d\delta'}{dt'} dt' \\
 &= \frac{\Phi_0}{2\pi} \int_0^\delta I_0 \sin \delta' d\delta' \\
 &= -E_J(\cos \delta - 1),
 \end{aligned} \tag{2.18}$$

where

$$E_J = \frac{I_0 \Phi_0}{2\pi} \tag{2.19}$$

is the Josephson energy. Typically, the constant term in Eq. (2.18) is omitted since only differences in potential energy are meaningful. Finally, we note that, by Eq. (2.16), the branch flux [see Eq. (A.1)] across a junction is given by

$$\Phi(t) = \int_{-\infty}^t V(t')dt' = \frac{\Phi_0}{2\pi} \delta(t). \tag{2.20}$$

---

<sup>4</sup>We assume that at  $t = -\infty$ , there are no currents or voltages in the circuit, therefore  $\delta = 0$  [25, 26].

## 2.3 Transmon

From the analysis of Josephson junctions presented in Section 2.2, the Hamiltonian for the transmon circuit shown in Fig. 2.2(a) is given by [27]

$$\hat{H} = \frac{\hat{Q}^2}{2C_\Sigma} - E_J \cos(2\pi\hat{\Phi}/\Phi_0) + \frac{C_{xy}}{C_\Sigma} \hat{Q} V_d(t), \quad (2.21)$$

where  $C_\Sigma = C_q + C_{xy}$  and  $E_J = I_{0q}\Phi_0/2\pi$  (see Appendix A.3 for further detail). Note that when  $\Phi/\Phi_0 \ll 1$ , this Hamiltonian is identical to Eq. (2.13) after the following substitutions are made:  $C_r \rightarrow C_q$ ,  $C_d \rightarrow C_{xy}$ , and  $L_r = \Phi_0/(2\pi I_{0q}) = L_J(\delta = 0)$ . Using this same line of reasoning (with  $V_d(t) = 0$ ), we can estimate the transition frequencies of transmon by treating the quartic term of the cosine potential as a small perturbation

$$\hat{H}' = -\frac{E_J}{12} \left( \frac{2\pi}{\Phi_0} \right)^4 \hat{\Phi}^4 = -\frac{E_C}{12} (\hat{a} + \hat{a}^\dagger)^4$$

added to the harmonic oscillator Hamiltonian. This calculation yields

$$\hbar\omega_{10} = E_1 - E_0 = \hbar\omega_0 - E_C$$

$$\hbar\omega_{21} = E_2 - E_1 = \hbar\omega_0 - 2E_C$$

$$\hbar\omega_{32} = E_3 - E_2 = \hbar\omega_0 - 3E_C$$

⋮

where

$$\omega_0 = \sqrt{8E_J E_C}/\hbar \quad (2.22)$$

is the plasma frequency<sup>5</sup> and

$$E_C = e^2/2C_\Sigma \quad (2.23)$$

is the charging energy (with  $e = +1.602 \times 10^{-19}$  C). The validity of this approximation breaks down for higher excited states where additional terms in the cosine expansion are needed to faithfully represent the potential energy landscape. At any rate, in the transmon limit (i.e.  $E_J/E_C \gg 1$ ) this is an excellent approximation for the first few energy levels, allowing us to estimate the nonlinearity of the system using the closed form expression

$$\boxed{\eta = \omega_{21} - \omega_{10} \simeq -E_C/\hbar}, \quad (2.24)$$

rather than relying on complicated solutions based on the Mathieu functions [27]. In a typical experiment  $\omega_{10}/2\pi \simeq 5$  GHz and  $\eta/2\pi \simeq -250$  MHz leading to a relative nonlinearity  $\simeq 5\%$ . We note that while the weak nonlinearity of the transmon is a disadvantage from the standpoint of gate speed, it is important to maintain a high  $E_J/E_C$  ratio in order to limit the transmon's sensitivity to charge noise which scales as  $\exp(-\sqrt{8E_J/E_C})$  [27, 28]. Though this condition could be satisfied by choosing a higher  $E_J$  to compensate for an increase in  $E_C$ , it would increase the frequency of the transmon and require a larger area (or higher critical current density) Josephson junction, all of which cause problems of their own [29–32]. A phase basis representation of the transmon's wavefunctions are shown in Fig. 2.2(c) using the parameters from rows

---

<sup>5</sup>The frequency obtained by using the second order coefficient in an expansion of the potential about a local minimum.

3-7 of Table 2.1. Note the high degree of similarity between the transmon and harmonic oscillator [see Fig. 2.1(c)], as expected for a system with a relative nonlinearity of  $\sim 5\%$ .

From the methods discussed in Appendix A.4, we can approximate the Hamiltonian in Eq. (2.21) as

$$\hat{H} = -\frac{\hbar\omega_q}{2}\hat{\sigma}_z + \left(\frac{C_{xy}}{C_\Sigma}V_d(t)Q_{\text{zpf}}\right)\hat{\sigma}_y, \quad (2.25)$$

where

$$\omega_q \simeq (\sqrt{8E_J E_C} - E_C)/\hbar \quad (2.26)$$

is the angular qubit frequency and  $\hat{\sigma}_z$ ,  $\hat{\sigma}_y$  are the usual Pauli matrices acting on the lowest two energy levels of the system. For a drive of the form

$$V_d(t) = |V_d| \times \left( Y(t) \cos(\omega_q t) - X(t) \sin(\omega_q t) \right), \quad (2.27)$$

where  $|V_d|$  is the amplitude,  $\omega_q$  is the drive frequency (resonant with the qubit), and  $X(t)$  and  $Y(t)$  are window functions, the Hamiltonian in the interaction picture is (see Appendix A.5 for further detail)

$$\hat{H}_I(t)/\hbar = \Omega_R \times \left( Y(t) \frac{\hat{\sigma}_y}{2} + X(t) \frac{\hat{\sigma}_x}{2} \right), \quad (2.28)$$

where

$$\Omega_R = Q_{\text{zpf}}|V_d| \frac{C_{xy}}{C_\Sigma} / \hbar \quad (2.29)$$

is the angular Rabi frequency. Time evolution in the interaction picture obeys the equation

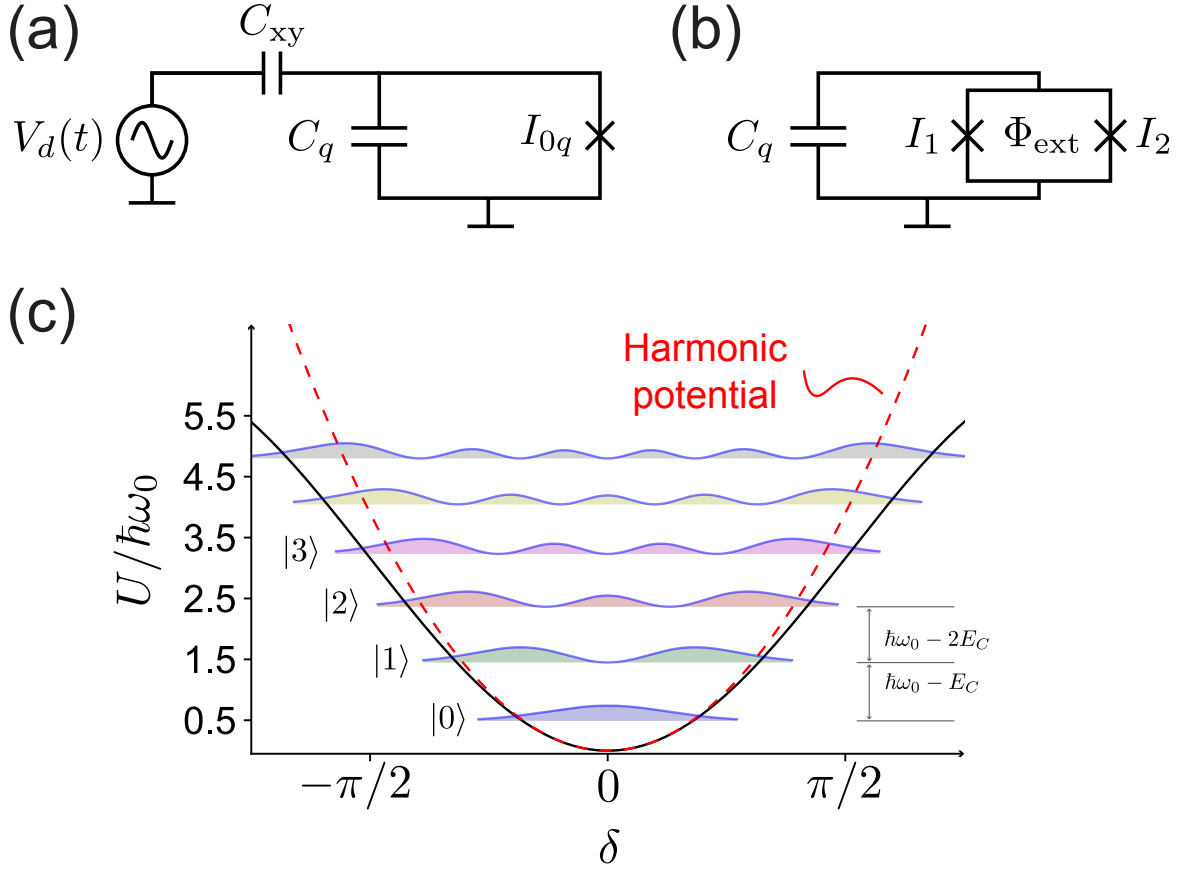


Figure 2.2: The transmon qubit. (a) A fixed frequency transmon with self-capacitance  $C_q$  and junction critical current  $I_{0q}$  coupled to a drive source  $V_d(t)$  via the capacitance  $C_{xy}$ . (b) A frequency tunable transmon with the JJ from part (a) replaced by a dc SQUID with external flux  $\Phi_{\text{ext}}$  threading the loop. (c) Wavefunctions for the fixed frequency transmon using the parameters listed in rows 3-7 of Table 2.1. The overlaid Harmonic potential energy landscape  $U_h = E_J\delta^2/2$  is identical to potential in Fig. 2.1(c), allowing for a comparison between the transmon and harmonic oscillator.

$$|\psi(t)\rangle_I = \hat{U}_I(t)|\psi(0)\rangle_I,$$

where

$$\hat{U}_I(t) = \mathcal{T} \left\{ \exp \left( -\frac{i}{\hbar} \int_0^t \hat{H}_I(t') dt' \right) \right\},$$

is the Dyson series (with time-ordering operator  $\mathcal{T}$ ) and  $|\psi(0)\rangle_I$  is the initial state vector in the interaction frame. If  $H_I(t')$  commutes with itself for all times  $t'$ , we can forgo the details of time-ordering, leading to the familiar propagator equation

$$\hat{U}_I(t) = \exp \left( -\frac{i}{\hbar} \int_0^t \hat{H}_I(t') dt' \right).$$

Assuming  $H_d(t) = \hbar\Omega_R\hat{\sigma}_x/2$ , the propagator is given by

$$\hat{U}_I(t) = \exp \left( -i\frac{\Omega_R t}{2} \hat{\sigma}_x \right).$$

This corresponds to a rotation of the state vector  $|\psi(0)\rangle_I$  about the  $x$ -axis of the Bloch sphere at an angular frequency  $\Omega_R$ . Adding back in the window function  $X(t)$  to drive term, one finds that

$$\boxed{\hat{U}_I(t) = \exp \left( -i\frac{\Omega_R}{2} \hat{\sigma}_x \int_0^t X(t') dt' \right)}. \quad (2.30)$$

This means that we can control the rotation angle of the state vector by simply varying

the integral  $\int_0^t X(t')dt'$ . Similarly, leading to the propagator

$$\boxed{\hat{U}_I(t) = \exp\left(-i\frac{\Omega_R}{2}\hat{\sigma}_y \int_0^t Y(t')dt'\right)}. \quad (2.31)$$

### 2.3.1 Frequency Tunable Transmon

Consider the circuit depicted in Fig. 2.2(c). The potential energy for the dc SQUID loop in Fig. 2.2(c) can be written as [27]

$$U(\hat{\delta}; \Phi_{\text{ext}}) = -E_J(\Phi_{\text{ext}}) \cos(\hat{\delta} - \phi), \quad (2.32)$$

where  $E_J(\Phi_{\text{ext}})$  is the effective Josephson energy,  $\Phi_{\text{ext}}$  is the external flux threading the dc SQUID loop,  $\hat{\delta} = (\hat{\delta}_1 + \hat{\delta}_2)/2$  is the effective phase difference across the junction<sup>6</sup>, and  $\phi$  is an offset phase determined by the equation

$$\tan \phi = d \tan (\pi \Phi_{\text{ext}} / \Phi_0), \quad (2.33)$$

where  $d = (I_2 - I_1)/(I_1 + I_2)$  is the junction asymmetry parameter. The effective Josephson energy

$$E_J(\Phi_{\text{ext}}) = E_\Sigma \cos\left(\frac{\pi \Phi_{\text{ext}}}{\Phi_0}\right) \sqrt{1 + (d \tan(\pi \Phi_{\text{ext}} / \Phi_0))^2}, \quad (2.34)$$

where  $E_\Sigma = \Phi_0(I_1 + I_2)/2\pi$ . In this situation, the effective phase difference  $\delta = 2\pi\Phi/\Phi_0$  in the canonical commutation relation  $[\hat{\Phi}, \hat{Q}] = i\hbar$ . This leads to a frequency tunable

---

<sup>6</sup>As it turns out, a treatment of time

transmon, with a qubit frequency given by

$$\omega_q(\Phi_{\text{ext}}) = (\sqrt{8E_J(\Phi_{\text{ext}})E_C} - E_C)/\hbar, \quad (2.35)$$

which tunes from the maximum frequency  $\omega_{q,\text{max}} \simeq (\sqrt{8E_{J,\Sigma}E_C} - E_C)/\hbar$  down to  $\omega_{q,\text{min}} \simeq \omega_{q,\text{max}} \times \sqrt{d}$ . This frequency tunability is an important feature for implementing fast, high-fidelity controlled-phase (CZ) gates with transmons [33–35] and for avoiding unwanted interactions with TLS defects in the qubit’s energy spectrum [29, 32, 36]. However, this also opens up channels for enhanced dephasing and relaxation.

## 2.4 Josephson Photomultiplier

Consider the JPM circuit depicted in depicted in Fig. 2.3(a). By current conservation, we have that

$$C_j \ddot{\Phi} + I_{0j} \sin(2\pi\Phi/\Phi_0) + (\Phi - \Phi_{\text{ext}})/L_j = 0,$$

where  $C_j$  is the shunt capacitance,  $I_{0j}$  is the junction critical current, and  $L_j$  is the geometric inductance of the rf SQUID loop. The corresponding circuit Lagrangian

$$\mathcal{L} = \frac{1}{2}C_j \dot{\Phi}^2 + E_J(\cos(2\pi\Phi/\Phi_0) - 1) - \frac{(\Phi - \Phi_{\text{ext}})^2}{2L_j},$$

where  $E_J = I_{0j}\Phi_0/2\pi$  is the Josephson energy. Identifying the canonical momentum  $Q = C_j \dot{\Phi}$ , the Hamiltonian can be written as

$$\hat{H} = \frac{\hat{Q}^2}{2C_j} - E_J \cos(2\pi\hat{\Phi}/\Phi_0) + \frac{(\hat{\Phi} - \Phi_{\text{ext}})^2}{2L_j}. \quad (2.36)$$

Identifying the potential energy term

$$U(\delta) = -E_J \cos(\delta) + \left(\frac{\Phi_0}{2\pi}\right)^2 \frac{(\delta - 2\pi\Phi_{\text{ext}}/\Phi_0)^2}{2L_j},$$

with  $\delta = 2\pi\Phi/\Phi_0$ , we can solve for the extrema<sup>7</sup> of this potential by setting  $dU/d\delta = 0$ .

This yields the condition

$$\sin \delta = \frac{1}{\beta_L} (2\pi\Phi_{\text{ext}}/\Phi_0 - \delta) \quad (2.37)$$

where

$$\beta_L = \frac{2\pi I_{0j} L_j}{\Phi_0} \quad (2.38)$$

is the hysteresis parameter [22]. Physically, Eq. (2.37) is a straightforward statement of current conservation in the SQUID loop; solutions can be depicted graphically as shown in Fig. 2.3(b). Notice that  $-1/\beta_L$  determines the slope of the line intersecting the sinusoid from Eq. (2.37), and that the  $y$ -intercept of the line is  $\propto \Phi_{\text{ext}}$ .

The curvature at the local minima of the potential determines the plasma frequency:

$$\omega_p = \frac{2\pi}{\Phi_0} \left[ \frac{1}{C_j} \frac{\partial^2 U}{\partial \delta^2} \right]^{1/2}.$$

This formula recovers the familiar harmonic oscillator expression  $1/\sqrt{LC_j}$ , where  $L$  is the parallel combination of the Josephson inductance (evaluated at the minimum of interest) and  $L_j$  (the geometric inductance). We can estimate the number of levels in a well by  $n \simeq \Delta U/\hbar\omega_p$ , where  $\Delta U$  is the potential energy barrier height. Under normal operation, the JPM (phase qubit) potential is well-approximated by a quadratic

---

<sup>7</sup>From elementary calculus,  $d^2U/d\delta^2 > 0$  indicates a potential minimum,  $d^2U/d\delta^2 < 0$  indicates a potential maximum.

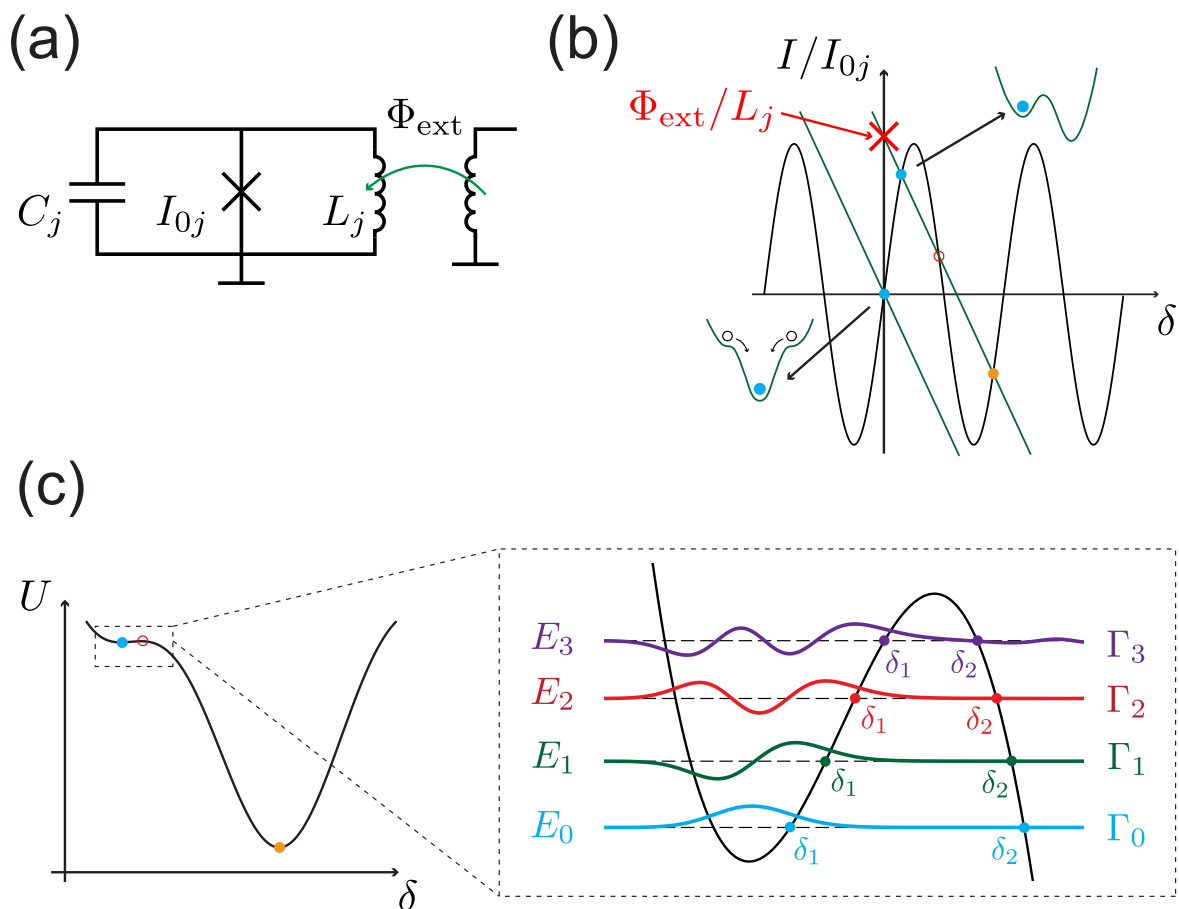


Figure 2.3: The flux-biased phase qubit. **(a)** A flux-biased phase qubit with shunt capacitance  $C_j$ , critical current  $I_{0j}$ , and geometric inductance  $L_j$ . The circuit is flux-biased using external circuitry which is mutually coupled to  $L_j$ , and generates an external flux  $\Phi_{\text{ext}}$  through the loop. **(b)** Graphical solution of Eq. (2.37). The slope of the line,  $-1/\beta_L$ , determines the number of extrema (shown as circles) for a fixed  $\Phi_{\text{ext}}$ . The potential minima (maxima) are indicated with solid (hollow) circles for a comparison with part (c). External flux  $\Phi_{\text{ext}}$  controls the y-intercept, allowing us to move between a single- and double-well regime as needed for JPM reset and photodetection. **(c)** Potential energy landscape of the JPM at a strongly nonlinear operating point. The zoom-in shows the bound states of the left well, with tunneling rates  $\Gamma_0 \ll \Gamma_1 \ll \Gamma_2 \ll \Gamma_3$ .

term plus a cubic perturbation that introduces nonlinearity into the system [see Fig. 2.3(c)]. Clearly, as  $\Delta U$  decreases, the nonlinearity of the well increases, and at a certain point, the well can no longer admit even a single bound state. Right before this happens, these circuits exhibit some interesting quantum mechanical behavior whereby the excited states tunnel out of the shallow minimum where they were localized into the deeper neighboring minima (see Appendices B.1 and B.7 for further detail).

## 2.5 Dispersive Measurement Systems

Consider the capacitively coupled transmon-resonator system depicted in Fig. 2.4. Treating the transmon from this circuit as an ideal two-level system, the Hamiltonian (in the rotating wave approximation) can be written as

$$H = \omega_r \hat{a}^\dagger \hat{a} - \frac{\omega_q}{2} \hat{\sigma}_z + g(\hat{a}^\dagger \hat{\sigma}_- + \hat{a} \hat{\sigma}_+), \quad (2.39)$$

where  $\omega_r \simeq 1/\sqrt{L_r(C_r + C_g)}$  is the resonator frequency,  $\omega_q \simeq (\sqrt{8E_J E_C} - E_C)/\hbar$  is the qubit frequency,  $E_J \simeq I_{0q}\Phi_0/2\pi$  is the qubit's Josephson energy,  $E_C \simeq e^2/2(C_q + C_g)$  is the qubit's charging energy, and

$$g \simeq \frac{\sqrt{\omega_r \omega_q}}{2} \frac{C_g}{\sqrt{(C_r + C_g)(C_q + C_g)}} \quad (2.40)$$

is the transmon-resonator coupling strength (see Appendix A.6 for further detail).

This Hamiltonian can be transformed using the Schrieffer–Wolff transformation into

the effective Hamiltonian (see Appendix A.6.2)

$$\begin{aligned}
\tilde{H}/\hbar &= \omega_r \hat{a}^\dagger \hat{a} - \frac{\omega_q}{2} \hat{\sigma}_z - \frac{\hat{\sigma}_z}{2} (2\chi \hat{n} + \chi) \\
&= \omega_r \hat{a}^\dagger \hat{a} - \underbrace{\frac{\hat{\sigma}_z}{2} \left( \omega_q + 2\chi \left( \hat{n} + \frac{1}{2} \right) \right)}_{\text{ac Stark shift + Lamb Shift}} \\
&= \underbrace{(\omega_r - \chi \hat{\sigma}_z) \hat{a}^\dagger \hat{a}}_{\text{dispersive resonator shift}} - \underbrace{\frac{\hat{\sigma}_z}{2} (\omega_q + \chi)}_{\text{qubit + Lamb shift}},
\end{aligned} \tag{2.41}$$

where

$$\chi = \frac{g^2}{\Delta} \tag{2.42}$$

with  $\Delta = \omega_q - \omega_r$ . Eq. (2.41) is the Jaynes-Cummings Hamiltonian in the dispersive approximation (i.e.,  $g \ll \Delta$ ). We find that the coupling term from Eq. (A.57) gives rise to small energy level shifts that depend on the resonator and qubit states. Interpreting the  $-\chi \hat{\sigma}_z \hat{a}^\dagger \hat{a}$  term as a qubit state-dependent frequency shift of the resonator, one arrives at a basic understanding of how dispersive measurement systems work. Alternatively, this term can be viewed as a resonator state-dependent frequency shift of the qubit (i.e., the ac Stark shift).

In reality, the transmon is not an ideal two-level system and the presence of the  $|2\rangle$  leads to a significant reduction in the effective dispersive shift  $\chi$ , which can be accounted for using the following substitution:

$$2\chi \rightarrow \frac{2g^2}{\Delta} \times \frac{\eta}{\Delta + \eta}, \tag{2.43}$$

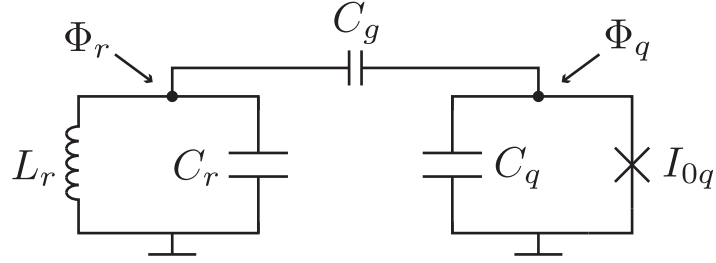


Figure 2.4: A capacitively coupled transmon-resonator system.

where  $\eta = \omega_{10} - \omega_{21}$ ,  $\Delta = \omega_q - \omega_r$ , and  $\omega_{r,|0\rangle} - \omega_{r,|1\rangle} = 2\chi$ . Noting that  $|\eta| \ll |\Delta|$ , the effective dispersive shift  $\chi \rightarrow (g^2/\Delta) \cdot \eta/\Delta$ , and therefore our original estimate of the dispersive shift is reduced by  $\eta/\Delta \sim 0.1$ . For details on how to calculate these corrections, see Refs. [27, 37, 38]. Notably, Ref. [38] showed that there is an additional correction to Eq. (2.43) given by  $\omega_r/\omega_q$ .

## Chapter 3

# JPM Experiment I

Fast, high-fidelity measurement is a key ingredient for quantum error correction<sup>1</sup>. Conventional approaches to the measurement of superconducting qubits, involving linear amplification of a microwave probe tone followed by heterodyne detection at room temperature, do not scale well to large system sizes. We introduce an approach to measurement based on a microwave photon counter demonstrating raw single-shot measurement fidelity of 92%. Moreover, the intrinsic damping of the photon counter is used to extract the energy released by the measurement process, allowing repeated high-fidelity quantum non-demolition measurements. Our scheme provides access to the classical outcome of projective quantum measurement at the millikelvin stage and could form the basis for a scalable quantum-to-classical interface.

---

<sup>1</sup>This chapter is a reformatted version of Ref. [39]

## 3.1 Introduction

In order to harness the tremendous potential of quantum computers, it is necessary to implement robust error correction to combat decoherence of the fragile quantum states. Error correction relies on high-fidelity, repeated measurements of an appreciable fraction of the quantum array throughout the run time of the algorithm [40]. In the context of superconducting qubits, measurement is performed by heterodyne detection of a weak microwave probe tone transmitted across or reflected from a linear cavity that is dispersively coupled to the qubit [41–47]. This approach relies on bulky, magnetic nonreciprocal circuit components to isolate the qubit from noisy amplification stages [44, 48–50]; moreover, the measurement result is only accessible following room temperature heterodyne detection and thresholding, complicating efforts to implement low-latency feedback conditioned on the measurement result [51, 52]. The physical footprint, wiring heat load, and latency associated with conventional amplifier-based qubit measurement stand as major impediments to scaling superconducting qubit technology.

An alternative approach involves entanglement of the qubit with the linear resonator to create cavity pointer states characterized by large differential photon occupation, followed by subsequent photodetection [53]. In our experiments Fig. 3.1(a), microwave drive at one of the two dressed cavity frequencies maps the qubit state onto “bright” and “dark” cavity pointer states. Discrimination of the states is performed directly

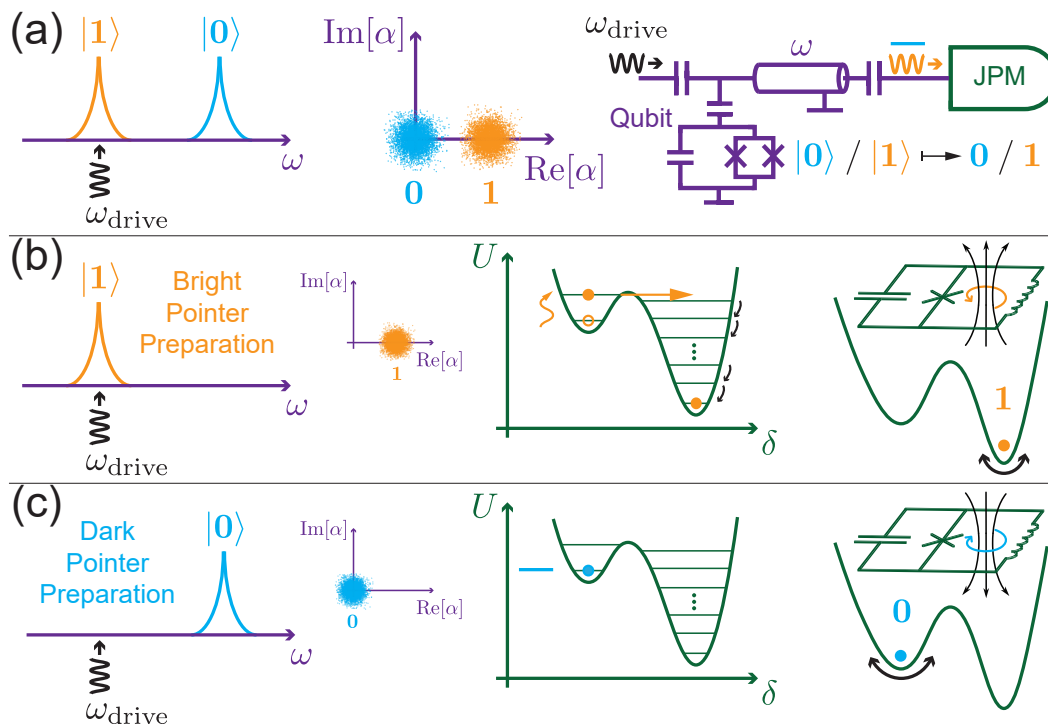


Figure 3.1: Qubit state measurement using the JPM. **(a)** Measurement overview. Microwave drive at the dressed cavity resonance corresponding to the qubit  $|1\rangle$  state creates bright and dark cavity pointer states with large differential photon occupation. These pointer states are detected using the JPM, which stores the measurement result as a classical bit at the millikelvin stage. **(b)** Bright pointer detection. Microwaves resonant with the JPM promote the circuit from the ground state of a metastable local minimum (here, left potential well) to an excited state. The detector subsequently undergoes a rapid tunneling transition that allows relaxation to the global minimum of the potential (here, right potential well). **(c)** Dark pointer detection. Energy contained in the dark pointer state is insufficient to induce a tunneling event. The presence (b) or absence (c) of an interwell tunneling transition results in classically distinguishable flux (oscillation) states in the detector.

at the millikelvin stage by the Josephson photomultiplier (JPM), a microwave photon counter; we use no nonreciprocal components between the qubit and JPM. The JPM is based on a single Josephson junction in an rf superconducting quantum interference device (SQUID) loop that is biased close to the critical flux where a phase slip occurs.

The circuit parameters are chosen to yield a potential energy landscape with one or two local minima, depending on flux bias; the distinct local minima correspond to classically distinguishable flux states in the device (see Appendix B.1). Once the JPM is properly biased, the presence of resonant microwaves induces a rapid tunneling event between the two classically distinguishable states of the detector [Fig. 3.1(b)]. In the absence of microwave input, transitions occur at an exponentially suppressed dark rate [Fig. 3.1(c)]. Thus, the absorption of resonant microwaves creates a readily measured “click” [54].

## 3.2 Experimental Setup

The qubit and the JPM are fabricated on different silicon substrates and housed in separate aluminum enclosures connected via a coaxial transmission line with characteristic impedance  $Z_0 = 50 \Omega$  and length  $L_0 = 14$  cm (see Appendices B.2-B.3). The qubit chip [purple circuit in Fig. 3.2(a)] incorporates an asymmetric transmon [Fig. 3.2(b)] that is capacitively coupled to a half-wave coplanar waveguide (CPW) resonator, the qubit cavity, with frequency  $\omega_1/2\pi = 5.020$  GHz and qubit-cavity coupling strength  $g_1/2\pi = 110$  MHz [27, 29, 55]. The qubit is operated at a fixed frequency  $\omega_q/2\pi = 4.433$  GHz and has an anharmonicity  $\alpha/2\pi = -250$  MHz.

The JPM [green circuit in Fig. 3.2(a)] is based on the capacitively-shunted flux-biased phase qubit [56]. The JPM is capacitively coupled to a local auxiliary CPW

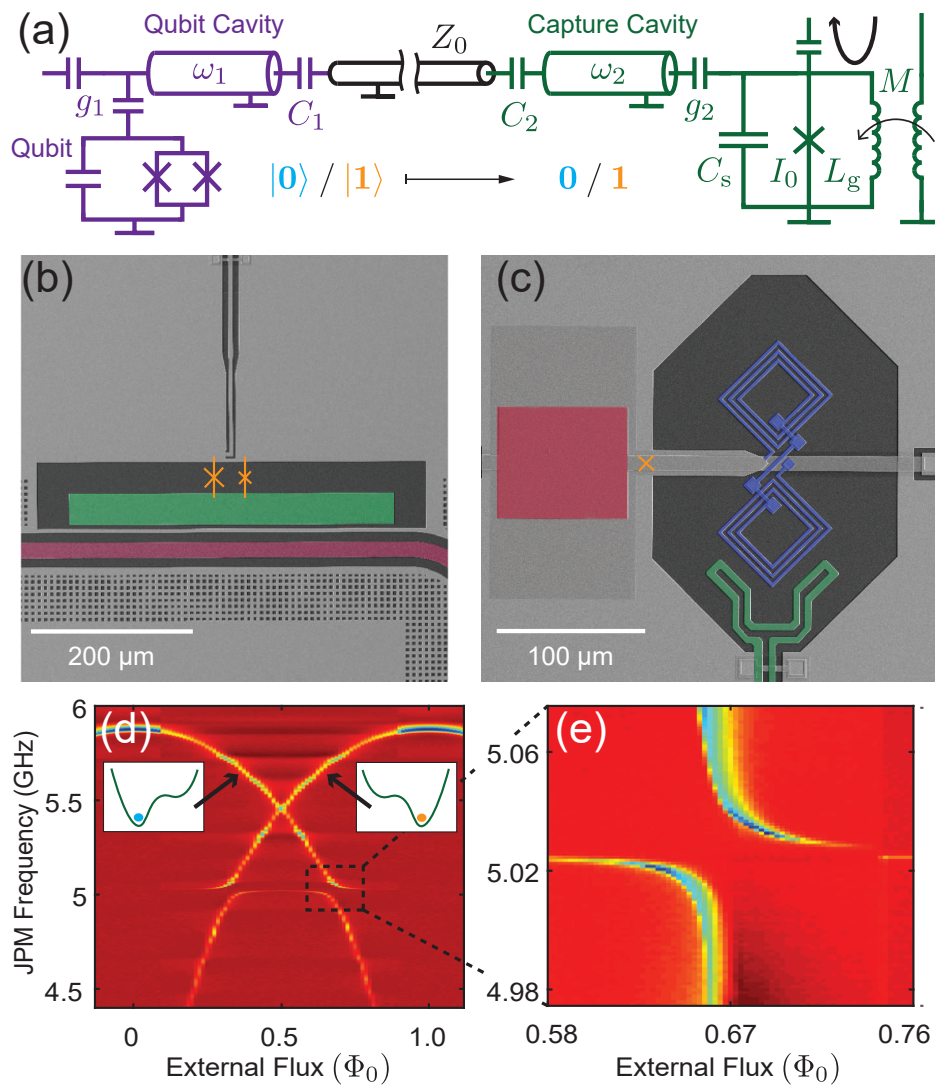


Figure 3.2: Experimental setup. **(a)** Circuit schematic. The qubit circuit (purple) is connected to the JPM circuit (green) via a coaxial transmission line (black) (see Tables B.1-B.3). **(b)** Micrograph of the transmon circuit with superconducting island (green), qubit cavity (red), and Josephson junctions (orange). **(c)** Micrograph of the JPM circuit (capture cavity not shown) with its 3+3 turn gradiometric loop inductance  $L_g$  (blue), single Josephson junction with critical current  $I_0$  (orange), parallel-plate capacitor  $C_s$  (red), and on-chip flux bias line with mutual inductance  $M$  (green). **(d)** JPM spectroscopy versus external flux. Insets show cartoons of a phase particle bound to the left and right wells. **(e)** Zoom in of the avoided level crossing between the JPM and capture cavity.

resonator, the capture cavity, with bare frequency  $\omega_1/2\pi = 5.028$  GHz and coupling strength  $g_1/2\pi = 40$  MHz. A micrograph of the JPM is shown in Fig. 3.2(c). The circuit involves a single Al-AlOx-Al Josephson junction with critical current  $I_0 = 1 \mu\text{A}$  embedded in a 3+3 turn gradiometric loop with inductance  $L_g = 1.1$  nH. The junction is shunted by an external parallel-plate capacitor  $C_s = 2$  pF. The plasma frequency of the JPM is tunable with external flux from 5.9 GHz to 4.4 GHz [Fig. 3.2(d, e)], allowing for both resonant and dispersive interactions between the JPM and capture cavity.

The qubit and capture cavities are capacitively coupled to the mediating transmission line (see Appendix B.4 and Tables B.1-B.3). Following pointer state preparation, microwave energy leaks out of the qubit cavity and a fraction of that energy is transferred to the capture cavity [57]. Without an intervening isolator or circulator to damp unwanted reflections, the finite length  $L_0$  of the transmission line admits a standing wave structure with an approximate mode spacing of  $v_p/2L_0$ , where  $v_p$  is the phase velocity of propagation in the cable. With these complications in mind,  $L_0$  was chosen to avoid destructive interference in the vicinity of  $\omega_1$  and  $\omega_2$  which can significantly degrade photon transfer efficiency (see Appendix B.5).

### 3.3 JPM Measurement Sequence

In the timing diagram of the measurement [Fig. 3.3(a)], the cartoon insets depict the dynamics of the JPM phase particle at critical points throughout the measurement sequence. We begin with a deterministic reset of the JPM, which is accomplished by biasing the JPM potential into a single-well configuration (see Appendix B.1). A depletion interaction between the JPM and capture cavity mode immediately follows in order to dissipate spurious microwave excitations generated during reset. Additional details of this depletion process are described later in the manuscript and in Fig. 3.4(a, b). Next, we use mode repulsion between the JPM and capture cavity to tune  $\omega_2$  in order to maximize photon transfer efficiency. The response of the capture cavity to an applied drive tone at four distinct JPM-capture cavity detunings, and thus four different values of  $\omega_2$ , is shown in Fig. 3.3(b); the detuning is chosen such that  $\omega_1 = \omega_2$ . At the beginning of the tune and capture stage, a qubit  $X$ -gate ( $I$ -gate) is performed and a subsequent qubit cavity drive tone is applied to prepare the bright (dark) pointer state (see Appendix B.6). The cavities are held on resonance for 750 ns to allow the pointer states to leak from the qubit cavity to the capture cavity; this time was determined by maximizing measurement fidelity with respect to the drive pulse duration. The bright pointer state corresponds to a mean qubit cavity photon occupation  $\bar{n}_1 \sim 10$ , calibrated using the ac Stark effect [Fig. 3.3(e)] (see Appendix B.8) [58, 59]. After pointer state transfer, the JPM is biased into resonance with the capture cavity and occupation of

that mode induces intrawell excitations of the phase particle on a timescale  $\pi/(2g_2 \sim 6 \text{ ns}$  [Fig. 3.3(c)] [20]. Finally, a short ( $\sim 10 \text{ ns}$ ) bias pulse is applied to the JPM to induce interwell tunneling of excited states [60]; the amplitude of the bias pulse is adjusted to maximize tunneling contrast between qubit excited and ground states [Fig. 3.3(d)]. At this point the measurement is complete: the measurement result is stored in the classical flux state of the JPM. To retrieve the result of qubit measurement for subsequent analysis at room temperature, we use a weak microwave probe tone to interrogate the plasma resonance of the JPM following measurement. The JPM bias is adjusted so that the plasma frequencies associated with the two local minima in the potential are slightly different; reflection from the JPM can distinguish the flux state of the detector with  $> 99.9\%$  fidelity in under 500 ns (see Appendix B.4).

Each measurement cycle yields a binary result -“0” or “1” - the classical result of projective quantum measurement. To access qubit state occupation probabilities, the measurement is repeated 10,000 times. The JPM switching probabilities represent raw measurement outcomes, uncorrected for state preparation, relaxation, or gate errors. In Fig. 3.3(f) and 3.3(g) we display the raw measurement outcomes for qubit Ramsey and Rabi experiments, respectively. The JPM measurements achieve a raw fidelity of 92%. The bulk of our fidelity loss is due to qubit energy relaxation during pointer state preparation and dark counts, which contribute infidelity of 5% and 2%, respectively. In our setup, dark counts stem from both excess  $|1\rangle$  population of the qubit and spurious

microwave energy contained in our dark pointer state. We attribute the remaining infidelity to imperfect gating and photon loss during pointer state transfer. The qubit  $T_1$  of  $6.6 \mu\text{s}$  measured in these experiments is consistent with separate measurements of the same device using conventional heterodyne readout techniques; we see no evidence of JPM-induced degradation of qubit  $T_1$ .

### 3.4 Measurement Backaction and QNDness

As noted earlier, JPM switching events release a large energy of order 100 photons as the JPM relaxes from a metastable minimum to the global minimum of its potential [61]. It is critical to understand the backaction of JPM switching events on the qubit state. The JPM tunneling transient has a broad spectral content, and Fourier components of this transient that are resonant with the capture and qubit cavities will induce a spurious population in these modes that will lead to photon shot noise dephasing of the qubit [62, 63]. In Fig. 3.4(a) we show the results of qubit Ramsey scans performed with (orange) and without (blue) a forced JPM tunneling event prior to the experiment. In the absence of any mitigation of the classical backaction, qubit Ramsey fringes show strongly suppressed coherence and a frequency shift indicating spurious photon occupation in the qubit cavity [64]. However, we can use the intrinsic damping of the JPM mode itself to controllably dissipate the energy in the linear cavities and fully suppress photon shot noise dephasing. Immediately following JPM reset, the JPM

is biased to a point where the levels in the shallow minimum are resonant with the linear cavity modes. Energy from the capture cavity leaks back to the JPM, inducing intrawell transitions; at the selected bias point, the interwell transition probability is negligible. The JPM mode is strongly damped, with quality factor  $Q \sim 300$ , set by the loss tangent of the  $\text{SiO}_2$  dielectric used in the JPM shunt capacitor [1]. As a result, the energy coupled to the JPM is rapidly dissipated. With this deterministic reset of the cavities, fully coherent qubit Ramsey fringes are recovered for depletion times  $\geq 40$  ns as shown in Fig. 3.4(b). We reiterate that no nonreciprocal components are used in these experiments to isolate the qubit chip from the classical backaction of the JPM.

In Fig. 3.4(c) we explore the quantum non-demolition (QND) character of our measurement protocol [65]. We prepare the qubit in the superposition state  $(|0\rangle - i|1\rangle)/\sqrt{2}$  aligned along the  $-y$ -axis of the Bloch sphere. We verify the state by performing an overdetermined tomography [56]. Here the direction  $\theta$  and length  $t$  of a tomographic pulse are swept continuously over the equatorial plane of the Bloch sphere prior to measurement. For control pulses applied along the  $x$ -axis, the qubit undergoes the usual Rabi oscillations; for control applied along  $y$ , the qubit state vector is unaffected. Following an initial JPM-based measurement (including an additional  $1.4 \mu\text{s}$  of delay for qubit cavity ringdown), we perform a tomographic reconstruction of the qubit state by applying a pre-rotation and a final JPM-based measurement. In the right-hand panel of Fig. 3.4(c), we display tomograms corresponding to the classical

measurement results “0” (top) and “1” (bottom). When the measurement result “0” is returned, we find a tomogram that overlaps with the ideal  $|0\rangle$  state with fidelity 91% (see Appendix B.9). When the result “1” is returned, the measured tomogram corresponds to overlap fidelity of 69% with the  $|1\rangle$  state. The loss in fidelity for the qubit  $|1\rangle$  state is consistent with the measured qubit  $T_1$  time of  $6.6 \mu\text{s}$  and the  $2.8 \mu\text{s}$  between successive measurement drive tones. We conclude that our JPM-based measurement is highly QND.

### 3.5 Conclusion

Our high-fidelity, fast photon counter-based qubit measurement approach provides access to the binary result of projective quantum measurement at the millikelvin stage without the need for nonreciprocal components between the qubit and counter. In a future system, JPM-based readout could form the basis of the measurement side of a robust, scalable interface between a quantum array and a proximal classical controller, for example, by encoding the flux state of the JPM onto classical single flux quantum (SFQ) voltage pulses [66, 67] for subsequent post-processing via SFQ-based digital logic [68].

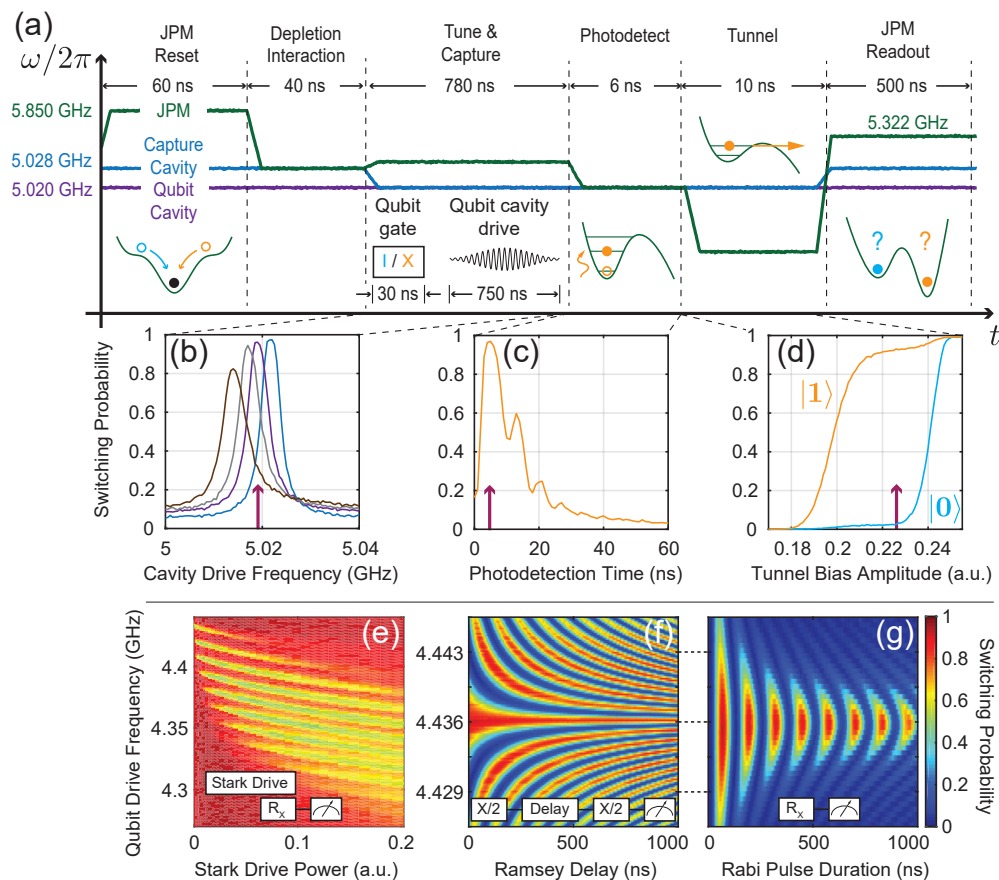


Figure 3.3: JPM-based qubit measurement. **(a)** We begin by resetting the JPM into a well-defined flux state. A subsequent depletion interaction removes spurious microwave excitations generated during reset [see Fig. 3.4(a, b) for more detail]. **(b)** Next, we tune the capture cavity frequency to maximize transfer efficiency from the qubit cavity. The response of the capture cavity to an applied drive at four distinct JPM-capture cavity detunings is shown; the detuning is chosen such that  $\omega_2 = \omega_1$ . During the tune and capture interval, a qubit  $X$ -gate ( $I$ -gate) is applied and microwave drive at the dressed  $|1\rangle$  cavity resonance is used to prepare the bright (dark) pointer state. As we drive the qubit cavity, a fraction of the microwave energy is transferred to the capture cavity during this capture step. **(c)** The JPM is then tuned into resonance with the capture cavity for photodetection. Photons present in the capture cavity induce intrawell transitions of the JPM to higher excited states. **(d)** Finally, a brief bias pulse is applied to induce tunneling of excited JPM states. The arrows on the bottom axes in (c)-(d) indicate optimal bias parameters. At this point the measurement is complete and the result is encoded in the classical flux state of the JPM. Microwave reflectometry is subsequently used to interrogate the JPM. **(e)** Stark spectroscopy used to calibrate qubit cavity photon occupation. JPM-detected Ramsey fringes and Rabi oscillations versus qubit drive detuning are shown in **(f)** and **(g)**, respectively.

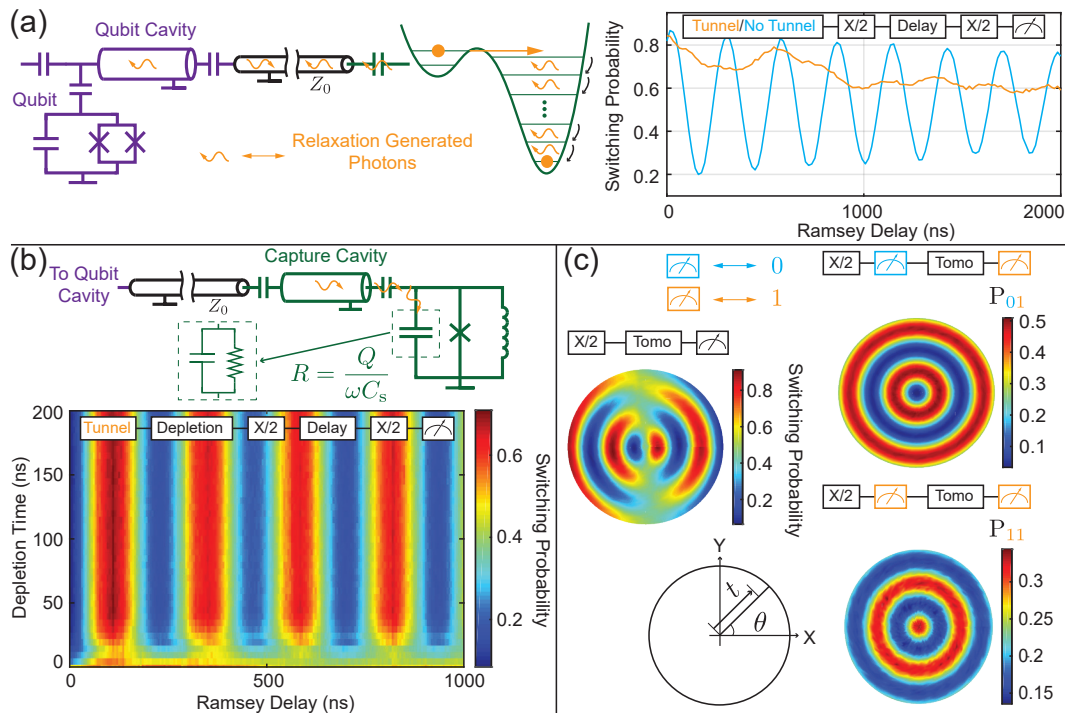


Figure 3.4: Mitigating backaction and preserving QND properties. (a) The JPM switching event releases energy of order 100 photons, inducing spurious population of the capture and qubit cavities. The right-hand panel shows baseline qubit Ramsey fringes (blue) and Ramsey fringes measured after a forced tunneling event by the JPM (orange). (b) Following the fast flux pulse that induces JPM tunneling, we adjust JPM bias so that energy deposited in the cavities is dissipated in the JPM, yielding a deterministic reset of the cavities. The color plot shows qubit Ramsey fringes versus duration of the depletion interaction between the JPM and the capture cavity. (c) Qubit tomography following JPM-based measurement. We prepare the superposition state  $(|0\rangle - i|1\rangle)/\sqrt{2}$  and verify the state with overdetermined qubit tomography (left panel). To characterize the qubit state after JPM-based measurement, we prepare the same superposition state, measure with the JPM, and then perform qubit tomography on the resulting state. Qubit tomography conditioned on the JPM measurement shows high overlap with target states  $|0\rangle$  (top right) and  $|1\rangle$  (bottom right).



## Chapter 4

# JPM Experiment II

We describe an approach to the high-fidelity measurement of a superconducting qubit using an on-chip microwave photon counter<sup>1</sup>. The protocol relies on the transient response of a dispersively coupled measurement resonator to map the state of the qubit to “bright” and “dark” cavity pointer states that are characterized by a large differential photon occupation. Following this mapping, we photodetect the resonator using the Josephson Photomultiplier (JPM), which transitions between classically distinguishable flux states when cavity photon occupation exceeds a certain threshold. Our technique provides access to the binary outcome of projective quantum measurement at the millikelvin stage without the need for quantum-limited preamplification and thresholding at room temperature. We achieve raw single-shot measurement fidelity in excess of 98% across multiple samples using this approach in total measurement times under

---

<sup>1</sup>This chapter is a reformatted version of Ref. [69]

500 ns. In addition, we show that the backaction and crosstalk associated with our measurement protocol can be mitigated by exploiting the intrinsic damping of the JPM itself.

## 4.1 Introduction

Fast, accurate state measurement is critical to the implementation of quantum error correction [40], and global optimization of a large-scale quantum processor demands minimization of physical resources required for qubit measurement [68]. Prior work on the measurement of superconducting qubits has focused on suppression of errors through combined improvements in measurement speed [44, 50, 70] and near-quantum-limited preamplification of the measurement signal [49, 71]; however, the physical footprint of the superconducting amplifiers, nonreciprocal circuit elements, and heterodyne detectors required to implement high-fidelity amplifier-based qubit measurement represents a significant obstacle to scaling. There have been efforts to minimize the hardware overhead associated with qubit measurement using Josephson circulators and directional amplifiers [72–76], but the instantaneous bandwidths of these elements are at present too small to support multiplexed qubit measurement, the primary advantage of amplifier-based approaches [44, 70]. In related work, state-of-the-art measurement efficiencies were achieved by directly embedding a qubit within a Josephson parametric amplifier [77]; however, this approach is not amenable to integration with large-scale

multiqubit arrays. While continued research in these directions is certainly essential, it is clear that there are major obstacles to be overcome.

In this work, we pursue an alternative approach to the measurement of superconducting qubits based on integrated microwave photon counters. The measurement protocol relies on the transient response of a dispersively coupled linear resonator to map the state of the qubit onto “bright” and “dark” cavity pointer states characterized by a large differential photon occupation [41, 53] [Fig. 4.1(a)]. Following this mapping, we photodetect the resonator using the Josephson Photomultiplier (JPM) [39, 54], which operates as a threshold detector of microwave photon occupation [Fig. 4.1(b)]. The JPM is based on a capacitively shunted rf Superconducting QUantum Interference Device (SQUID) with circuit parameters chosen to yield a double-well potential energy landscape [22]. JPM photodetection involves resonant transfer of energy from the bright pointer state of the readout cavity to the JPM mode, followed by a tunneling transition that changes the flux state of the JPM [Fig. 4.1(c)]; when the readout cavity is prepared in the dark state, no tunneling transition occurs. The flux state of the JPM represents a classical bit – the outcome of projective quantum measurement – that in principle can be accessed at the millikelvin stage, without the need for heterodyne detection and thresholding at room temperature. Without any fine tuning of qubit or JPM parameters, we achieve raw single shot measurement fidelities (uncorrected for qubit relaxation and initialization errors) in excess of 98% for total measurement times

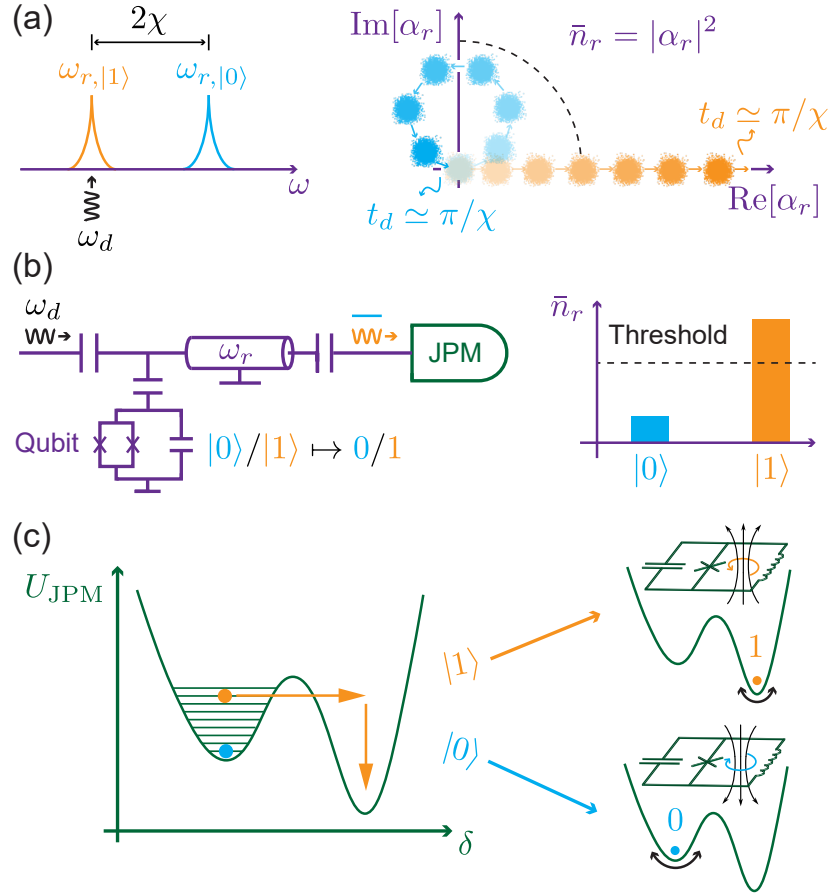


Figure 4.1: Qubit measurement with a photon counter. **(a)** Dispersive coupling of the qubit and the readout resonator yields distinct dressed frequencies of the cavity  $\omega_{r,|0\rangle}$  and  $\omega_{r,|1\rangle}$  corresponding to qubit states  $|0\rangle$  and  $|1\rangle$ , respectively. The application of a microwave drive at frequency  $\omega_d \simeq \omega_{r,|1\rangle}$  displaces the photon field inside the resonator in a qubit state-dependent manner. For resonant drive (orange), the field displaces along a single quadrature axis (drawn as  $\text{Re}[\alpha_r]$ , where  $|\alpha_r\rangle$  is the coherent state of the resonator). For off-resonant drive (blue), the readout cavity acquires a transient occupation; however, the cavity state coherently oscillates back toward vacuum at a time  $\pi/\chi$ , where  $2\chi = \omega_{r,|0\rangle} - \omega_{r,|1\rangle}$ . Therefore, drive for duration  $t_d = \pi/\chi$  maps the qubit state to “bright” and “dark” cavity pointer states with large differential photon occupation. **(b)** Following pointer state preparation, we photodetect the resonator using the JPM, which acts as a threshold discriminator of microwave photon occupation  $\bar{n}_r$ . **(c)** Resonant interaction of the JPM with the cavity leads to conditional excitation of the JPM followed by a tunneling transition between classically distinguishable flux states of the device.

around 500 ns. While the current experiments involve chips comprising two qubits, each with its own dedicated JPM, the approach can be scaled to arbitrary system size, as the physical footprint of the JPM is well matched to the footprint of the qubit. JPM-based measurement requires at most one additional flux bias line per qubit channel, while greatly relaxing the physical resources needed downstream of the millikelvin stage.

This manuscript is organized as follows. In Section 4.2, we discuss the design and characterization of our qubit-JPM circuit and provide a detailed description of the qubit measurement sequence. In Section 4.3, we describe optimization of photon number contrast of the cavity pointer states with respect to resonator drive parameters. In Section 4.4, we analyze the performance of the JPM-based measurement protocol and present a detailed fidelity budget. In addition, we discuss the long-term stability of the measurement and demonstrate the robustness of our protocol with respect to device-to-device variation. In Section 4.5, we discuss backaction and measurement crosstalk, and we demonstrate that intrinsic damping of the JPM itself is a resource that can be exploited to suppress initialization and crosstalk errors. In addition, we explore the degradation of measurement fidelity as the measurement cycle time is pushed below 10  $\mu$ s. Finally, in Section 4.6, we conclude and discuss prospects for the construction of a scalable quantum-to-classical interface at millikelvin temperatures.

## 4.2 Circuit Design and Bring-up

Our circuit consists of two coupled qubit-JPM systems integrated onto a single silicon chip as shown in the micrograph of Fig. 4.2(a). The circuit schematic is shown in Fig. 4.2(b), which introduces notation that will be used throughout the text. In this section, we report the parameters of qubit-JPM pair q1-j1 on chip #1; parameters for the other qubit-JPM pairs can be found in Table C.1. For information about sample fabrication and control wiring, see Appendices C.1 and C.2, respectively.

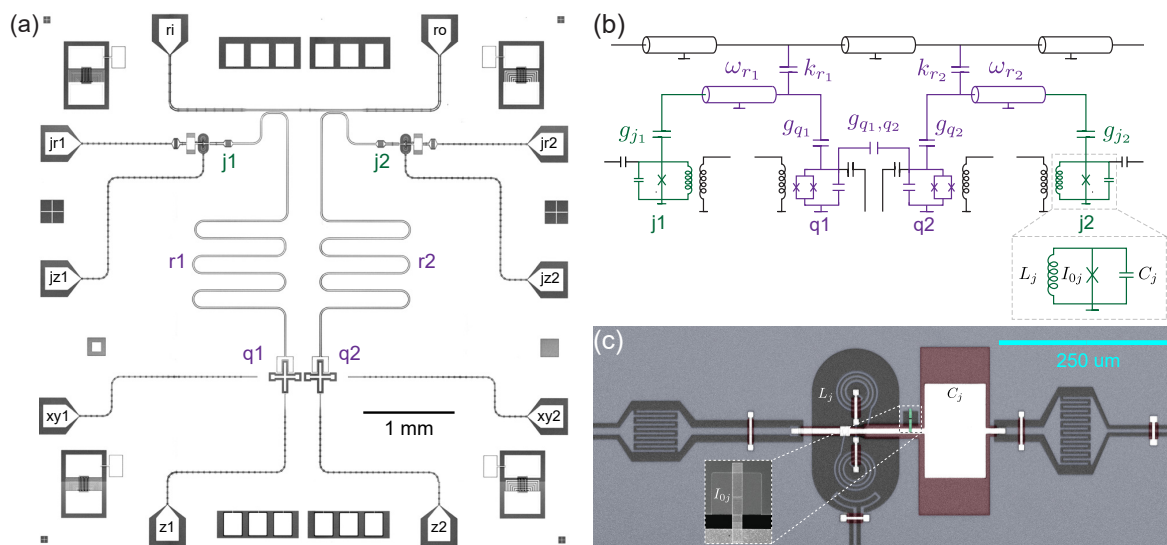


Figure 4.2: Device layout. **(a)** Optical micrograph of the circuit with overlaid text to indicate port functionality and the locations of critical circuit components. Each qubit-JPM system incorporates a transmon qubit q1(2), with excitation line xy1(2) and flux bias line z1(2), and a JPM j1(2), with dedicated readout line jr1(2) and flux bias line jz1(2). Each qubit-JPM pair is coupled to a half-wave CPW resonator r1(2). **(b)** Schematic diagram of the circuit. **(c)** False-color micrograph of the JPM element.

The qubit-JPM system incorporates a frequency-tunable transmon that is dispersively coupled to a half-wave coplanar waveguide (CPW) measurement resonator

[27, 29, 78] with bare frequency  $\omega_r/2\pi = 5.693$  GHz and qubit-resonator coupling strength  $g_{q,r}/2\pi = 90$  MHz. The total energy decay rate of the measurement resonator  $\kappa_r = 1/(1.53 \mu\text{s})$ , which is approximately two orders of magnitude smaller than that for a typical Purcell-filtered design [44, 50, 70]. The transmon has a maximum transition frequency  $\omega_q/2\pi = 5.95$  GHz and an anharmonicity  $\eta/2\pi = -225$  MHz. To avoid Purcell suppression of the qubit energy relaxation time [17], we operate at qubit frequencies below 5.1 GHz, which corresponds to a Purcell limit to qubit  $T_1$  of 66  $\mu\text{s}$ . We remark on a distinct advantage of our approach to qubit measurement compared to amplifier-based implementations: by reading out the measurement resonator with the JPM, we avoid the usual tradeoff between measurement speed and Purcell limit to  $T_1$ , as coupling of the measurement resonator to its readout environment can be tuned over a broad range on nanosecond timescales by appropriate variation of the JPM bias point. In principle, the value of  $\kappa_r$  can be made arbitrarily small without affecting the measurement speed; as a practical matter, however, a balance must be struck to ensure that the power delivered to the measurement resonator is sufficient for creation of the bright pointer state.

At the opposite voltage antinode, the measurement resonator is capacitively coupled to the JPM with coupling strength  $g_{j,r}/2\pi = 62$  MHz. This coupling strength is optimal, as it corresponds to a half-swap period  $\pi/(2g_{j,r}) = 4$  ns and is thus compatible with GS/s waveform generation and comparable to the energy relaxation time

of the JPM  $T_{1,j} = 5$  ns. The JPM circuit is formed by the parallel combination of a 3+3-turn gradiometric loop with inductance  $L_j = 1.3$  nH, a parallel-plate capacitance  $C_j = 2.2$  pF, and a single Al-AlO<sub>x</sub>-Al Josephson junction with critical current  $I_{0j} = 1.4$   $\mu$ A [see Fig. 4.2(b, c)]. The plasma frequency of the JPM is tunable with external flux from 4 to 7.3 GHz, allowing for both resonant and far-detuned interactions with the measurement resonator. To retrieve qubit measurement results from the JPM, the circuit is read out in reflection using the capacitively coupled readout port labeled jr1(2) in Fig. 4.2(a). The two metastable flux states of the JPM correspond to distinct plasma frequencies; therefore, microwave reflectometry in the vicinity of these resonances encodes the JPM flux onto the amplitude and phase of the reflected signal.

Device bring-up begins with JPM spectroscopy versus external flux, which yields the locations of the reset bias points that initialize the JPM in the left and right wells of its double-well potential along with the JPM-resonator avoided level crossing [see Fig. 4.3(a)]. Next, we maximize contrast of JPM reflectometry for states prepared in the left and right wells over the space of JPM readout flux, measurement frequency, and JPM drive power [Fig. 4.3(b)]. Using optimized parameters, the fidelity with which we read out the flux state of the JPM is better than 99.99%. In the following, we always initialize the JPM in the left well of its potential and refer to the probability of a transition to the right well as the *tunneling probability*.

A timing diagram of the qubit measurement sequence is shown in Fig. 4.4(a); the

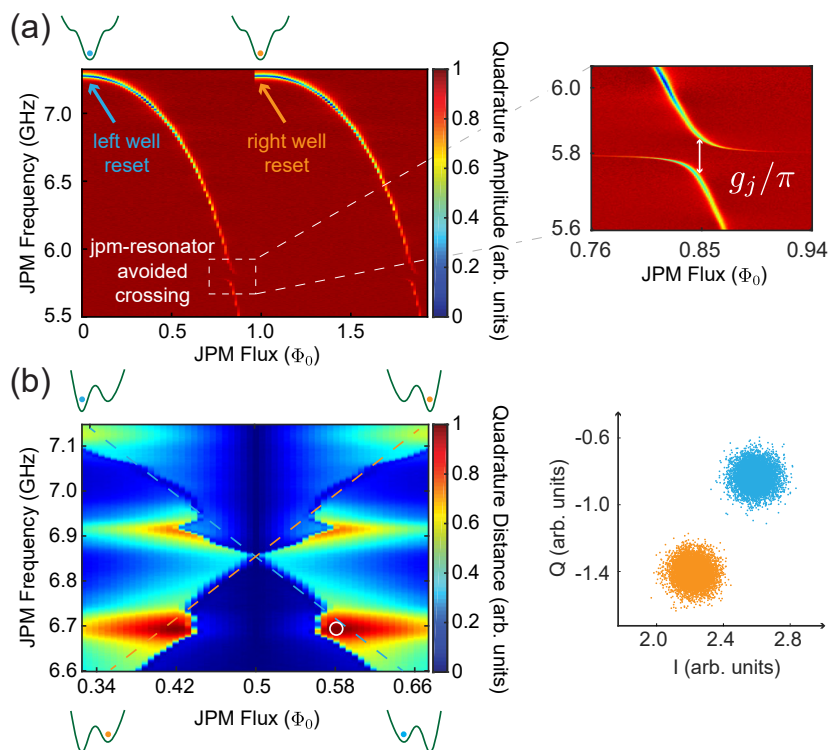


Figure 4.3: JPM bring-up. **(a)** JPM spectroscopy versus external flux. The spectroscopy signal is acquired from a reflection measurement at JPM readout ports jr1(2). Heterodyne detection of this signal yields in-phase (I) and quadrature (Q) components that depend on the applied frequency, the external flux bias of the JPM, and the flux state of the device. Arrows indicate left- and right-well reset bias points, where the potential energy landscape of the JPM supports only a single minimum. The enlargement to the right shows the JPM-resonator avoided level crossing. Following pointer state preparation, the JPM is biased to this point to induce resonant excitation of the JPM by the bright pointer. **(b)** Contrast in IQ signal for reflection from the JPM prepared in the left and right wells of the double-well potential. The white circle indicates the optimal parameters for JPM readout. IQ clouds for JPM readout at this point are shown on the right; here, the separation fidelity is better than 99.99%.

cartoon insets depict the evolution of the JPM phase particle during critical steps of the measurement sequence. The duration of each step is indicated at the top of each panel; for clarity, the time axis is not drawn to scale. During qubit operations prior

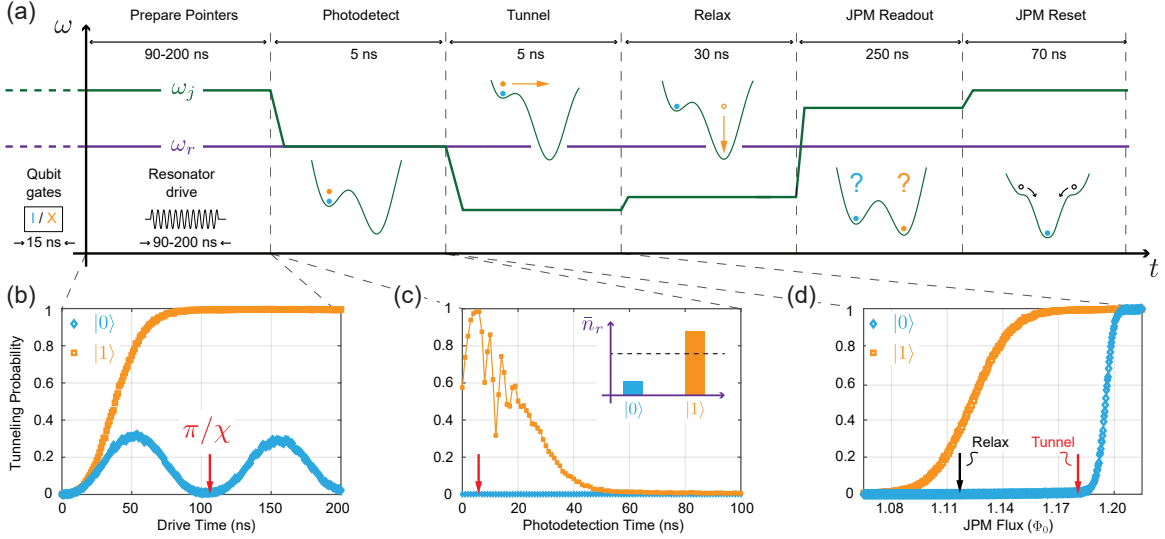


Figure 4.4: JPM-based qubit measurement sequence. **(a)** Measurement timing diagram; see text for detailed discussion. **(b)** Time evolution of high-contrast microwave cavity pointer states as detected by the JPM for qubits initialized in states  $|0\rangle$  (blue) and  $|1\rangle$  (orange). The optimal time for pointer state drive is indicated by the red arrow. **(c)** JPM tunneling probability versus photodetection time for qubits prepared in states  $|0\rangle$  and  $|1\rangle$ . The optimal time for JPM-cavity interaction is indicated by the red arrow. **(d)** JPM tunneling probability versus tunnel bias amplitude for qubits prepared in states  $|0\rangle$  and  $|1\rangle$ . The S-curves are well separated, corresponding to a raw measurement fidelity of 98.4% (see Section 4.4). The optimal tunnel bias point is indicated by the red arrow. Following the tunneling step, the JPM bias point is adjusted to the location indicated by the black arrow to allow the tunneled phase particle to relax. Following the tunneling event, the flux state of the JPM is read out in reflection using the methods discussed in Fig. 4.3(b). Finally, the JPM is reset into the left-well state.

to measurement, the JPM is biased at its flux-insensitive upper sweet spot to minimize JPM-induced damping of the measurement resonator. We prepare the target qubit state by applying the  $X$ -gate ( $I$ -gate); to achieve high-fidelity single-qubit gates, we implement fast (15 ns-long) cosine-shaped derivative reduction by adiabatic gate (DRAG) pulses with a static detuning correction [79–81]. At the start of the mea-

surement sequence, microwave drive at frequency  $\omega_{r,|1\rangle}$  is used to prepare the bright (dark) pointer state. In Fig. 4.4(b), we show the time evolution of optimized pointer states as detected by the JPM (see Section 4.3 for methods); the resonator drive time  $t_d = 105$  ns for the datasets shown in Fig. 4.4(c, d). Next, the JPM is biased into resonance with the measurement resonator to induce intrawell excitations of the phase particle conditioned on the qubit state [20]. The energy transferred into the JPM is maximal for a photodetection time of 5 ns  $\approx \pi/2g_{j,r}$  [Fig. 4.4(c)]. This timescale is independent of the photon occupation in the resonator, as one expects for coupled harmonic systems: at the JPM-resonator avoided level crossing, the left well of the JPM supports approximately 50 bound states. Immediately following photodetection, the JPM is biased towards the critical flux at which the shallow minimum in the potential energy landscape vanishes in order to induce interwell tunneling of excited states [Fig. 4.4(d)] [60]. The duration and amplitude of this bias pulse are chosen to maximize tunneling contrast between qubit excited and ground states; the optimal tunnel bias point is indicated by the red arrow in Fig. 4.4(d). We then adjust the JPM bias to the location indicated by the black arrow in Fig. 4.4(d) to allow the tunneled phase particle to relax for 30 ns. Without this step, a small fraction ( $\sim 5\%$ ) of the tunneled population migrates back into the left well, resulting in a degradation of measurement fidelity. To retrieve the qubit measurement results, we read out the JPM state using the methods discussed in Fig. 4.3(b). Finally, the JPM is reset into the left-well state

for use in subsequent experiments.

### 4.3 Pointer State Preparation

The success of our measurement protocol hinges on our ability to create high-contrast microwave cavity pointer states conditioned on the state of the qubit [see Fig. 4.1]. To achieve this experimentally, we need to determine the optimal resonator drive frequency, time, and amplitude. To optimize pointer state preparation, we begin with two-dimensional scans of the resonator with sweeps of both drive frequency and time, as shown in Fig. 4.5(a, b). Both datasets are taken over identical ranges and differ only in the prepared qubit state. The cartoons above each plot indicate that we are scanning over a range of frequencies containing both dressed resonances of the cavity, with the dressed resonance corresponding to the prepared qubit state drawn using a solid line. Optimal measurement contrast is achieved at drive parameters that maximize the difference in tunneling probability for the prepared qubit states  $|0\rangle$  and  $|1\rangle$  [Fig. 4.5(c)]; the optimal parameters correspond roughly to cavity drive at frequency  $\omega_d = \omega_{r,|1\rangle}$  (overlaid squares) and  $\omega_d = \omega_{r,|0\rangle}$  (overlaid circles) for a duration  $t_d \simeq \pi/\chi$ . Slight deviation of the optimal drive frequency from the two dressed cavity resonance frequencies and of the optimal drive time from  $\pi/\chi$  can be understood as the result of nonlinearity of the measurement resonator inherited from the qubit; this nonlinearity similarly limits the size of the bright pointer state that can be created with

a naive cavity ringup pulse applied at fixed frequency. As the dressed cavity resonance corresponding to qubit  $|1\rangle$  disperses less strongly with power than the resonance corresponding to qubit  $|0\rangle$ , we achieve best measurement fidelity with cavity drive  $\omega_d \simeq \omega_{r,|1\rangle}$ , meaning that the qubit  $|1\rangle$  ( $|0\rangle$ ) state is mapped onto the bright (dark) cavity pointer state.

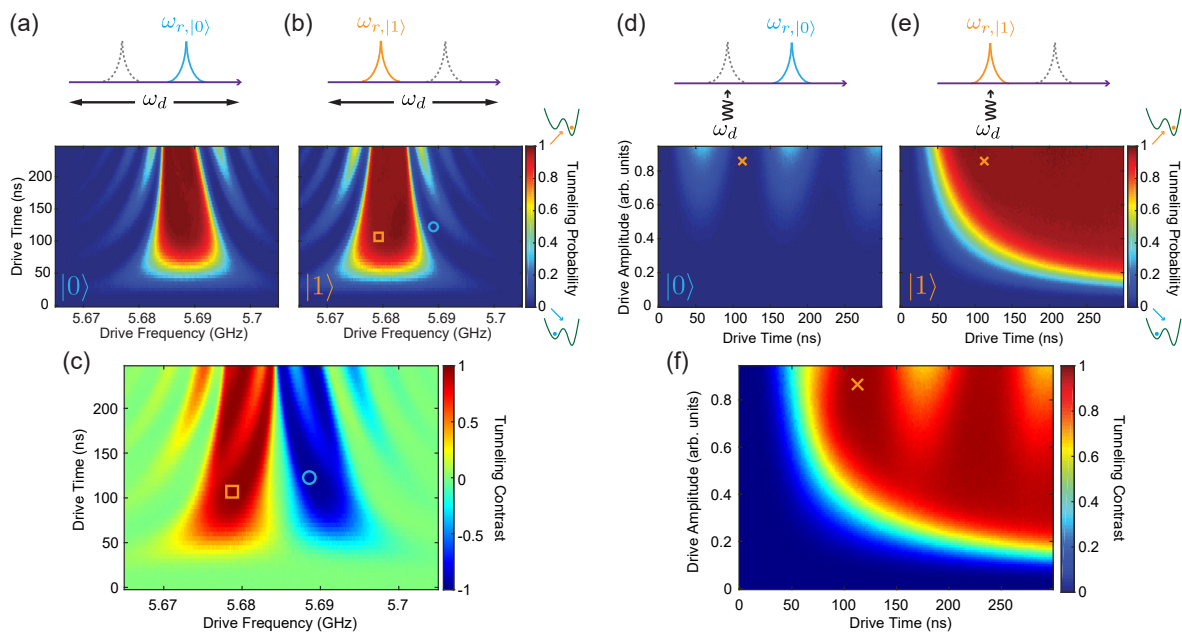


Figure 4.5: Pointer state preparation. **(a)** JPM tunneling probability versus resonator drive time and frequency with the qubit prepared in  $|0\rangle$ . **(b)** As in (a), but with the qubit prepared in  $|1\rangle$ . **(c)** The difference in these scans allows determination of the optimal drive frequency and time that maximize single-shot measurement fidelity. We find two local maxima in measurement fidelity for drive frequencies near  $\omega_{r,|0\rangle}$  (overlaid circles) and  $\omega_{r,|1\rangle}$  (overlaid squares) for a duration  $t_d \simeq \pi/\chi$ . For comparison with parts (d)-(e), these datasets were taken at a resonator drive amplitude of 0.8 arb. units. **(d)** JPM tunneling probability versus resonator drive amplitude and time with the qubit prepared in the  $|0\rangle$  state. This scan uses the drive frequency  $\omega_d \simeq \omega_{r,|1\rangle}$  found in parts (a) and (b). **(e)** As in (d), but with the qubit prepared in  $|1\rangle$ . **(f)** The difference in these scans yields the optimal drive amplitude and time for pointer state preparation as indicated by the overlaid X symbols.

Next, we perform two-dimensional scans of the resonator with sweeps of both drive amplitude and time, as shown in Fig. 4.5(d, e). The cartoons above each plot indicate the frequency of the cavity drive with respect to the dressed cavity resonances. Taking the difference between these scans yields the optimal drive amplitude and time as shown in Fig. 4.5(f). Scans of type Fig. 4.5(a, b) and Fig. 4.5(d, e) are repeated iteratively to optimize single-shot measurement fidelity over the space of resonator drive time, frequency, and amplitude, with the final results displayed in Fig. 4.4(b). This method converges on a drive frequency that is  $-2.1$  MHz detuned from  $\omega_{r,|1\rangle}/2\pi$ , leading to a 22% decrease in the resonator drive time as compared to  $\pi/\chi$ . The bright pointer state corresponds to a mean resonator occupation  $\bar{n}_r \approx 27$  photons, determined via the ac Stark effect (see Appendix C.3 for further detail). Ultimately, photon number contrast is limited by imperfect preparation of the dark pointer state: as occupation of the dark pointer becomes comparable to the critical photon number  $n_{\text{crit}} = (\Delta_{q,r}/g_{q,r})^2/4$  [41], the nonlinearity of the resonator prevents coherent oscillation back to the vacuum state [82, 83], contributing an infidelity around 0.6% (see discussion in the next section). We expect that it will be straightforward to suppress this source of infidelity by a slightly more complicated ringup sequence involving either composite pulses or a chirped frequency drive.

## 4.4 Measurement Fidelity

We analyze the performance of JPM-based measurement in terms of the fidelity

$$F = 1 - P(1|0) - P(0|1), \quad (4.1)$$

where  $P(i|j)$  is the probability of measuring the qubit in state  $|i\rangle$  given that it was nominally prepared in state  $|j\rangle$  [84]; here, detection of a tunneling transition from the left well to the right well of the JPM constitutes measurement of the qubit  $|1\rangle$  state, while the absence of a tunneling transition constitutes measurement of qubit  $|0\rangle$ . Using the measurement sequence described in Fig. 4.4, we perform a standard Rabi experiment to identify values for  $P(1|1)$  and  $P(1|0)$  as shown in Fig. 4.6(a); assuming that leakage errors are negligible, we have  $F = P(1|1) - P(1|0)$ . In order to faithfully estimate the conditional probabilities  $P(i|j)$ , the measurement sequence is repeated 5,000 times. Prior to each measurement, an active qubit reset step is performed to extract unwanted excess  $|1\rangle$  population from the qubit (see Appendix C.5 for further detail); without this step, the excess  $|1\rangle$  state population of our qubits is approximately 4%.

To characterize the long-term stability of JPM-based measurement, we perform 20,000 independent determinations of  $F$  evenly spaced over the span of twelve hours; the results are shown in the histogram of Fig. 4.6(b). We achieve an average raw measurement fidelity  $\bar{F} = 98.4 \pm 0.2\%$ , uncorrected for state preparation, relaxation, or gate errors. A detailed budget of measurement infidelity is shown in Table 4.1.

The nonvanishing  $P(1|0)$  contains contributions both from qubit initialization errors and from imperfect dark pointer state preparation. Using the methods described in Appendix C.4, we infer an excess  $|1\rangle$  population of 0.3% following active qubit reset. This initialization infidelity degrades both  $P(0|0)$  and  $P(1|1)$ , contributing an overall infidelity of 0.6% to our measurement. We attribute the remaining portion of  $P(1|0)$  to imperfect dark pointer state preparation, for which we obtain 0.6%. Nonvanishing  $P(0|1)$  contains additional contributions from qubit relaxation and  $X$ -gate error. Qubit relaxation with timescale  $T_1 = 16.9 \mu\text{s}$  contributes an infidelity  $t_d/2T_1 = 0.3\%$ , where  $t_d = 105 \text{ ns}$  is the drive time for pointer state preparation. Finally, we use interleaved randomized benchmarking (IRB) [85] to characterize the infidelity of our  $X$ -gate, for which we find 0.1%.

We have characterized measurement fidelity for system q1-j1 on chip #1 over a range of qubit operating points, corresponding to a range of optimal resonator drive times from 90-200 ns; results are shown in rows 1-4 of Table 4.2. For all experiments, we maintain the same readout parameters calibrated at the initial qubit bringup point  $\omega_q/2\pi = 5.037 \text{ GHz}$ , apart from the resonator drive time, which must be matched to  $\pi/\chi$ . We maintain similar performance across all four qubit frequencies. This demonstrates that fine-tuning of JPM bias parameters is not needed to address qubits that resonate over a broad range of frequencies.

While the above results were obtained for the single qubit-JPM pair q1-j1 on chip

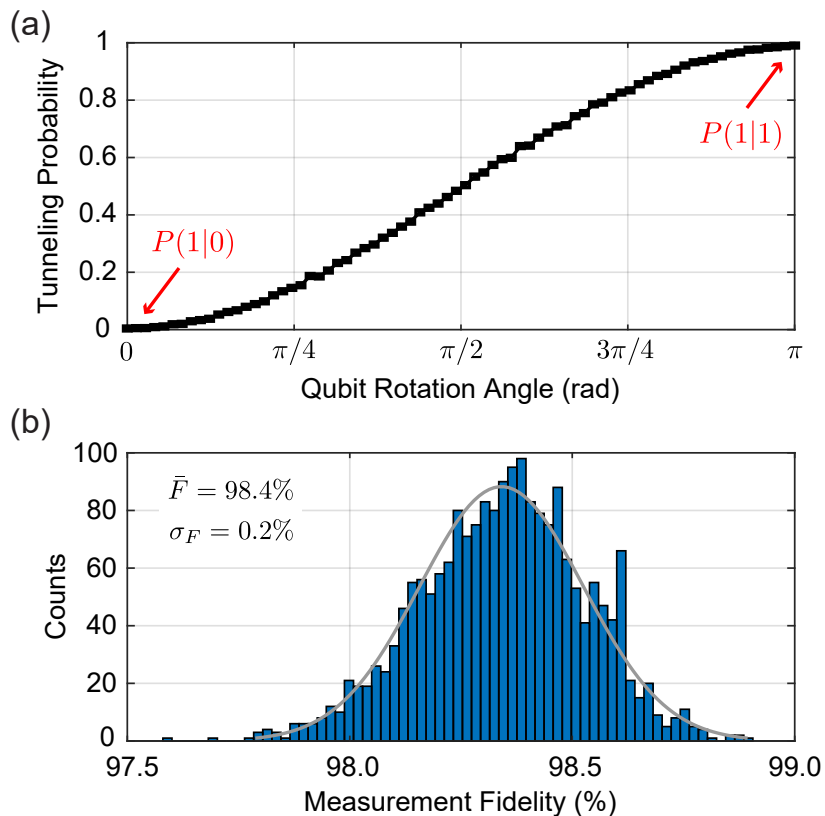


Figure 4.6: Measurement fidelity and long-term stability. **(a)** JPM tunneling probability versus qubit rotation angle to identify values for  $P(1|0)$  (0 rotation) and  $P(1|1)$  ( $\pi$  rotation). For this dataset,  $P(1|0) = 0.4\%$  and  $P(1|1) = 99.0\%$ . **(b)** Histogram of measurement fidelity  $F$  logged over the span of twelve hours (20,000 independent measurements of  $F$ ), demonstrating the robustness of JPM-based measurement with respect to long-term drift. A Gaussian fit to the histogram yields an average fidelity  $\bar{F} = 98.4\%$  with standard deviation  $\sigma_F = 0.2\%$ .

#1, we observe similar performance for the three other qubit-JPM pairs that we have examined; measurement fidelities for these devices are reported in rows 5-7 of Table 4.2.

The durations of the flux bias parameters determined from our bring-up of pair q1-j1 on chip #1 were used for all remaining qubit-JPM pairs, without full optimization of each separate qubit-JPM system. The raw single-shot measurement fidelity averaged

Source of Infidelity	Infidelity (%)	Calculation Method
Excess $ 1\rangle$ population	0.6	low power drive
Imperfect dark pointer	0.6	high power drive
Qubit relaxation	0.3	$t_d/2T_1$
X-gate	0.1	IRB [85]

Table 4.1: Infidelity budget for the data displayed in Fig. 4.6(b).

Chip #	Qubit-JPM Pair	$\omega_q/2\pi$ (GHz)	Resonator Drive Time (ns)	Measurement Fidelity (%)
1	q1-j1	5.037	105	98.4
1	q1-j1	5.098	90	98.3
1	q1-j1	4.980	150	97.1
1	q1-j1	4.833	200	98.1
1	q2-j2	5.069	147	98.0
2	q1-j1	5.068	128	97.6
2	q2-j2	5.062	163	98.3

Table 4.2: Measurement fidelity within and across devices. The first entry corresponds to the data shown in Fig. 4.6(b), and therefore represents the average fidelity  $\bar{F}$ . The remaining entries (rows 2-7) correspond to single measurements of  $F$ .

over the four qubit-JPM pairs is 98%.

## 4.5 Backaction and Crosstalk

JPM tunneling events deposit an energy of order 100 photons on chip as the phase particle relaxes to the global minimum of the potential [39, 61] [see Fig. 4.7(a)]. The associated transient contains spectral components at the frequencies of the readout resonator and the qubit, and as a result can transfer energy to these modes [Fig. 4.7(b)]. It is therefore critical to characterize the backaction and crosstalk associated with JPM tunneling events.

We begin with a study of JPM-induced backaction using the Rabi experiment described in Fig. 4.7(c). Prior to the qubit drive pulse, we force a tunneling event in the JPM and perform a deterministic reset of the JPM in the left well. In the absence of mitigation, the Rabi scan yields a nearly constant tunneling probability of 80% as a function of the qubit rotation angle, indicating severe corruption of the qubit and the readout resonator by the JPM tunneling event. Next, we perform JPM-assisted resonator reset prior to the Rabi experiment as a potential mitigation strategy. Namely, we bias the JPM into resonance with the readout cavity for 100 ns as a means to deplete the cavity of photons released by the JPM tunneling event [39]. With resonator reset, we recover Rabi oscillations with low visibility  $\sim 30\%$ . In a further refinement, we adjust the bias point of the qubit during the JPM tunneling event from 5.1 GHz down to 4.4 GHz in order to minimize the spectral content of the tunneling transient at the qubit frequency; we refer to this as a *hide bias* step. By concatenating the hide bias step with resonator reset, we obtain a Rabi visibility  $\sim 75\%$ . Finally, we append a JPM-assisted qubit reset step to the end of the mitigation sequence. With full mitigation, we recover all but 0.2% of the measurement fidelity compared to the situation with no forced JPM tunneling event. The resonator and qubit reset steps take a combined time of 200 ns (see Appendix C.5).

We characterize JPM-induced crosstalk to the unmeasured qubit by performing a spin-echo experiment on one qubit following a forced JPM tunneling event on the neigh-

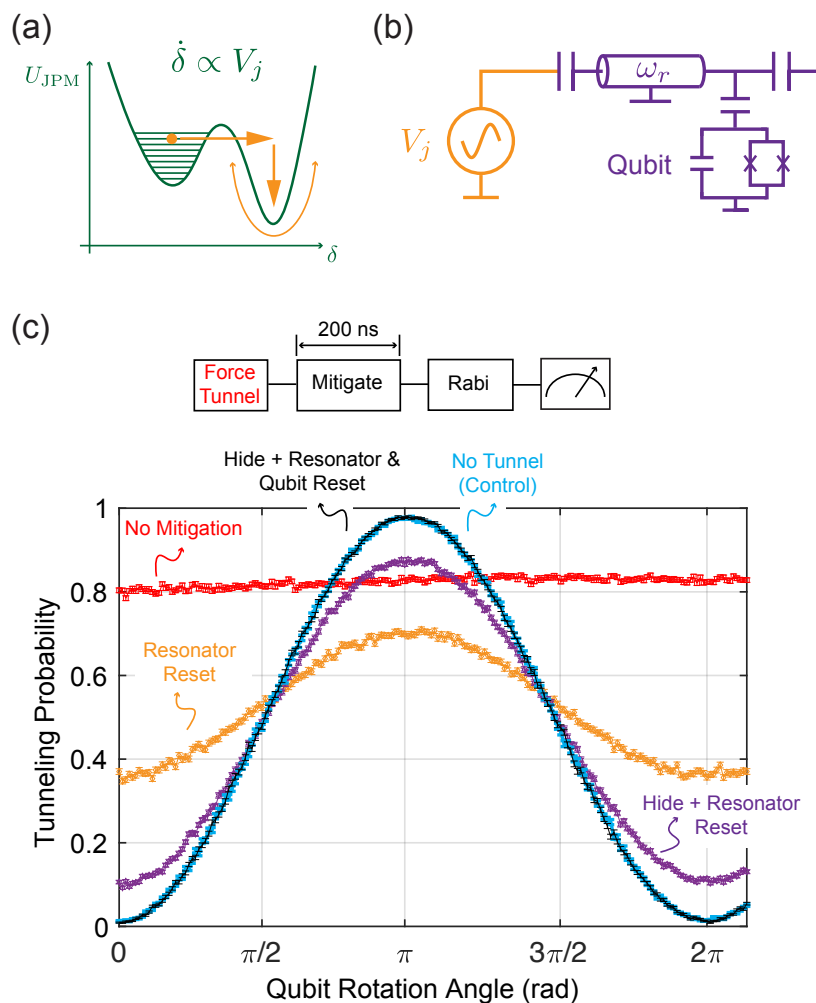


Figure 4.7: Characterizing and mitigating backaction induced by the JPM tunneling event. **(a)** Relaxation processes following a JPM tunneling event deposit an energy of order 100 photons on chip. **(b)** By the ac Josephson relation, the JPM is modeled as an effective voltage source  $V_j$  that can excite both the resonator and qubit modes. **(c)** Rabi experiments preceded by a forced JPM tunneling event followed by various mitigation steps. The hide step is accomplished by biasing the qubit to a frequency where backaction from the forced tunneling event is minimal. With full mitigation (i.e. qubit hide bias plus resonator and qubit reset), we recover all but 0.2% of the measurement fidelity compared to the experiment with no forced JPM tunneling event.

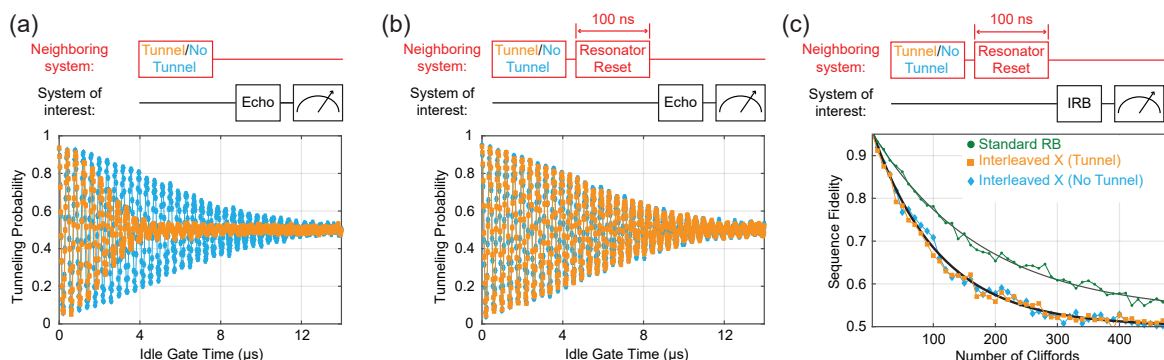


Figure 4.8: Characterizing and mitigating crosstalk induced by the JPM tunneling event. **(a)** Spin echo data taken on the q1-j1 system on chip #1 with and without a prior forced tunneling event on the q2-j2 system. The spin-echo gate sequence is  $X/2 - \text{Idle}/2 - Y - \text{Idle}/2 - X/2$ . We observe a factor of 2.6 reduction in the Gaussian decay envelope of the spin-echo fringes with respect to the control experiment with no forced tunneling event. **(b)** As in part (a), but with resonator reset on system q2-j2 following the forced tunneling event. We recover identical spin-echo fringes with respect to the control. **(c)** Interleaved randomized benchmarking (IRB) experiment to quantify the performance of our crosstalk mitigation strategy. We measure identical IRB gate fidelities for the tunnel and no tunnel cases following resonator reset on q2-j2 (see Table 4.3 for further detail).

boring qubit-JPM pair [see Fig. 4.8(a)]. We use spin-echo to probe qubit coherence as opposed to a conventional Ramsey experiment in order to suppress the contribution to dephasing from low-frequency  $1/f$  magnetic flux noise [55, 86, 87]. We measure a factor of 2.6 reduction in the Gaussian decay time of the spin-echo fringes with respect to our control experiment <sup>2</sup>, indicating the presence of unwanted crosstalk between systems. We speculate that the enhanced dephasing is due to spurious photon occupation in the measurement resonator of the tunneled JPM, leading to photon shot noise dephasing of the neighboring qubit via parasitic coupling [62, 63, 88]. To test this hy-

<sup>2</sup>The spin-echo decay envelope obtained from modeling photon shot noise dephasing using our circuit parameters is well described by a Gaussian function of the idle gate time

Interleaved Gate	Gate Fidelity (Tunnel)	Gate Fidelity (No Tunnel)
$X$	$99.8 \pm 0.3\%$	$99.8 \pm 0.2\%$
$X/2$	$99.9 \pm 0.3\%$	$99.9 \pm 0.2\%$
$I$	$99.9 \pm 0.1\%$	$99.9 \pm 0.1\%$

Table 4.3: Interleaved randomized benchmarking results for the crosstalk experiments described in Section 4.5. Each of the interleaved gates reported here has a total duration of 15 ns.

pothesis, we add a resonator reset step following the forced tunneling event as shown in Fig. 4.8(b). With resonator reset, we recover identical spin-echo fringes with respect to the control experiment. To confirm that resonator reset fully mitigates crosstalk of the JPM-based measurement, we use IRB to quantify single-qubit gate error with and without a prior forced JPM tunneling event in the neighboring qubit-JPM system [Fig. 4.8(c)] [85]. With resonator reset following the JPM tunneling event, we measure identical interleaved gate fidelities for the tunnel and no tunnel cases, as summarized in Table 4.3.

To implement a practical error-corrected superconducting quantum computer based on the two-dimensional surface code, measurement repetition rates of order 1 MHz will be required [89, 90]. For this reason, we analyze the dependence of JPM-based measurement fidelity on the time between experiments using the measurement sequence depicted in Fig. 4.9(a). We find that as the time between experiments decreases, the fidelity  $P(1|1)$  with which we detect the bright pointer state degrades, with a characteristic time for recovery of fidelity of  $13 \mu\text{s}$  [see Fig. 4.9(b)]. We speculate that the degradation in fidelity is due to enhanced loss in both the qubit and the JPM at

high measurement repetition rates. To separately examine the contributions of the JPM and the qubit to the loss of fidelity, we switch the roles of the bright and dark pointer states as shown in Fig. 4.9(c). With the qubit  $|1\rangle$  state mapped to the dark cavity pointer, the measurement fidelity is insensitive to enhanced loss in the JPM, since an elevated JPM relaxation rate would preserve the correct outcome for measurement of the dark pointer state (namely, no tunneling event). However, in this case we do see enhanced  $P(0|1)$  for measurement duty cycles below  $5 \mu\text{s}$ , indicating a contribution to infidelity either from enhanced qubit relaxation or from qubit initialization errors. Similarly, when we map the qubit  $|0\rangle$  state to the bright cavity pointer, the tunneling probability  $P(0|0)$  is insensitive to qubit loss and dominated by enhanced loss in the JPM element that prevents mapping of the bright pointer state to a tunneling event. We conclude that the enhanced measurement infidelity observed at high repetition rate is dominated by loss in the JPM, with a small contribution from increased qubit errors at the highest repetition rates  $> 200 \text{ kHz}$ . While the physics that drives this degradation in fidelity is not presently understood, we speculate that the enhanced loss in both the qubit and the JPM is mediated by the transfer of energy released in the tunneling event to nonequilibrium quasiparticles [91, 92] or to dielectric two-level states (TLS) in the lossy bulk oxides of the JPM or in the surface oxides of the qubit. Possible mitigation strategies to preserve measurement fidelity at repetition rates approaching 1 MHz include incorporation of quasiparticle traps into the circuit

[93, 94] or a modification of the JPM energy landscape to reduce the energy released by the tunneling event.

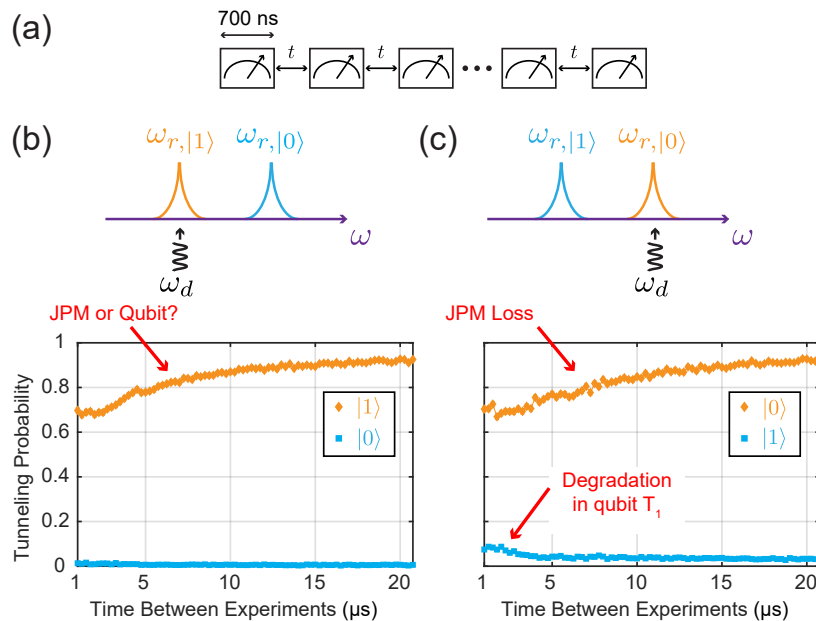


Figure 4.9: Dependence of JPM-based measurement fidelity on repetition rate. **(a)** Timing sequence of the experiment to probe sensitivity to measurement repetition rate. Each measurement takes 700 ns from start to finish, including resonator and qubit reset. **(b)** JPM-detection of the qubit  $|0\rangle$  and  $|1\rangle$  states versus interval between measurements. **(c)** As in (b), but with the qubit  $|0\rangle$  state mapped to the bright pointer (i.e.  $\omega_d = \omega_{r,|0\rangle}$ ). Parts (b) and (c) indicate a degradation in both JPM detection efficiency and qubit  $T_1$  as the repetition rate is increased, with the former playing the dominant role.

## 4.6 Conclusion

We have developed and characterized a fast, accurate state measurement technique for superconducting qubits using on-chip microwave photon counters. Our technique pro-

vides access to the binary result of projective quantum measurement at the millikelvin stage of a dilution refrigerator; furthermore, it eliminates the need for nonreciprocal circuit components between the qubit and the measurement apparatus [39]. While our achieved raw single-shot measurement fidelity  $> 98\%$  already compares favorably with the current state of the art [95], straightforward improvements in pointer state preparation and suppression of qubit relaxation and initialization errors should push raw single-shot measurement fidelity beyond 99%. Our study of achievable measurement repetition rate revealed an anomalous source of loss associated with JPM tunneling events; this topic merits further investigation. We anticipate that straightforward modifications to our circuit design will provide a path to higher measurement repetition rates.

The physical footprint of the JPM is well matched to the dimensions of the qubit, so that it would be straightforward to integrate a single JPM element with every qubit in a large-scale multiqubit processor; in such an architecture, each cell in the array would require one additional flux bias line for JPM control. Microwave-based readout of the classical flux state of the JPM is amenable to multiplexing for the efficient measurement of large multiqubit arrays with low hardware overhead; alternatively, it is possible to encode the flux state of the JPM in a propagating fluxon [66, 67, 96] that could then be passed to a proximal classical Josephson digital circuit for error monitoring of the qubit array, postprocessing of the measurement results, and low-latency feedback. Combined

with digital approaches to coherent control [97, 98], this approach to measurement could form the basis for a scalable quantum–classical interface for next-generation superconducting qubit arrays [68].

# Appendix A

## Mathematical Derivations

### A.1 Introducing Branch Variables

In this section, we introduce the concepts needed to quantize simple electrical circuits.

Following Vool and Devoret [25, 26], we begin with definitions of the *branch flux*

$$\Phi_b(t) = \int_{-\infty}^t V_b(t') dt' \quad (\text{A.1})$$

and *branch charge*

$$Q_b(t) = \int_{-\infty}^t I_b(t') dt', \quad (\text{A.2})$$

where

$$V_b(t) = \int_{\text{start of b}}^{\text{end of b}} \vec{E}(\vec{r}, t) \cdot d\vec{l} \quad (\text{A.3})$$

is the voltage drop across a branch element and

$$I_b(t) = \frac{1}{\mu_0} \oint \vec{B}(\vec{r}, t) \cdot d\vec{l} \quad (\text{A.4})$$

is the current flowing through it as shown in Fig. A.1. We note that the line integral in Eq. (A.4) is taken along a close curve in ‘vacuum’ encircling the element. Here, by a *branch* we mean a two-port electrical component (e.g., a capacitor, inductor, or Josephson junction). The total energy absorbed by the element is given by

$$\mathcal{E}_b(t) = \int_{-\infty}^t I_b(t') V_b(t') dt', \quad (\text{A.5})$$

where  $I_b(t)V_b(t)$  is the instantaneous electrical power absorbed by the component. We assume that at  $t = -\infty$ , the circuit was at rest (i.e., all currents and voltages in the system were zero). Throughout this text, we will identify  $\Phi_b$  with the ‘position’ coordinate and  $\dot{\Phi}_b$  with the ‘velocity’ coordinate. Then, to construct a circuit Lagrangian (typically denoted by  $\mathcal{L}$ ), we simply subtract the kinetic (capacitive) and potential (inductive) energy terms such that the Euler-Lagrange equation(s) for the system

$$\frac{d}{dt} \frac{\partial \mathcal{L}}{\partial \dot{\Phi}_b} = \frac{\partial \mathcal{L}}{\partial \Phi_b}$$

recover the equation(s) of motion that one would arrive at using classical circuit theory.

In Table A.1, we list the energies stored in the three most basic circuit components in terms of the branch flux  $\Phi_b$  and its first time derivative  $\dot{\Phi}_b$ . Notice that we have added in offset terms to the capacitive and inductive energies, which are typically assumed to have both intrinsic and extrinsic contributions. We refer the interested reader to Refs.

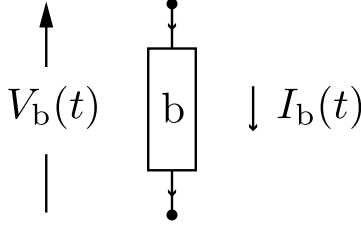


Figure A.1: Sign convention for the voltage  $V_b(t)$  and current  $I_b(t)$  associated with an arbitrary branch element  $b$  of an electrical circuit. Reproduced (with modifications) from Ref. [26].

[25, 26, 99] for further detail.

Table A.1: Energy stored in non-dissipative circuit elements.

Element	Energy	Type
linear capacitance $C$	$C(\dot{\Phi}_b - V_{\text{offset}})^2/2$	‘kinetic’
linear inductance $L$	$(\Phi_b - \Phi_{\text{offset}})^2/2L$	‘potential’
Josephson junction $E_J = I_0\Phi_0/2\pi$	$E_J(1 - \cos(2\pi\Phi_b/\Phi_0))$	‘potential’

## A.2 Hamiltonian for a Driven LC Circuit

Consider the circuit depicted in Fig. 2.1(b). By current conservation, we have that

$$\underbrace{C_d(\dot{V}_d(t) - \ddot{\Phi})}_{\text{current through } C_d} = \underbrace{C_r\ddot{\Phi}}_{\text{current through } C_r} + \underbrace{\Phi/L_r}_{\text{current through } L_r} \quad (\text{A.6})$$

when written in terms of the flux<sup>1</sup>  $\Phi$  [see Eq. (A.1)]. By inspection, the Lagrangian that reproduces this equation of motion is

$$\mathcal{L} = \frac{1}{2}C_r\dot{\Phi}^2 + \frac{1}{2}C_d(\dot{\Phi} - V_d(t))^2 - \frac{\Phi^2}{2L_r}. \quad (\text{A.7})$$

One can verify this using the Euler-Lagrange equation [Eq. (2.3)]. To derive the Hamiltonian for this system, we first express  $\dot{\Phi}$  in terms of the canonical momentum<sup>2</sup>

$$Q \equiv \frac{\partial \mathcal{L}}{\partial \dot{\Phi}} = (C_d + C_r)\dot{\Phi} - C_d V_d(t). \quad (\text{A.8})$$

From here, we find that

$$\dot{\Phi} = \frac{Q + C_d V_d(t)}{C_\Sigma}, \quad (\text{A.9})$$

where  $C_\Sigma \equiv C_d + C_r$ . Then, from the definition of the Hamiltonian, one finds that

$$\begin{aligned} H &= \dot{\Phi}Q - \mathcal{L} \\ &= \frac{Q^2}{C_\Sigma} + \frac{C_d}{C_\Sigma}QV_d(t) - \left( \frac{1}{2C_\Sigma} \left[ Q^2 + 2C_dQV_d(t) + \cancel{C_d^2V_d(t)^2} \right] \right. \\ &\quad \left. - \frac{C_d}{C_\Sigma}QV_d(t) - \cancel{\frac{C_d^2}{2}V_d(t)^2} + \frac{C_d}{2}V_d(t)^2 - \frac{\Phi^2}{2L_r} \right) \\ &= \frac{Q^2}{2C_\Sigma} + \frac{\Phi^2}{2L_r} + \frac{C_d}{C_\Sigma}QV_d(t). \end{aligned} \quad (\text{A.10})$$

Note that all terms independent of both  $Q$  and  $\Phi$  have been omitted in the final expression for  $H$ . At this point,  $Q$  and  $\Phi$  are promoted to operators satisfying the canonical commutation relationship  $[\hat{\Phi}, \hat{Q}] = i\hbar$ , and the circuit is said to have been *quantized*.

---

<sup>1</sup>We assume that both branches of this circuit are connected by an ideal wire (i.e., with no capacitance or inductance), and furthermore that there are no external fields (magnetic or electric) near these two components. Under these conditions, the branch flux across the capacitor and inductor are equal, which we refer to simply as the flux.

<sup>2</sup>Often referred to as the node charge or simply as the charge.

### A.3 Hamiltonian for a Transmon

Consider the circuit depicted in Fig. 2.2(a). By current conservation, we have that

$$\underbrace{C_{xy}(\dot{V}_d(t) - \ddot{\Phi})}_{\text{current through } C_{xy}} = \underbrace{C_q \ddot{\Phi}}_{\text{current through } C_q} + \underbrace{I_{0q} \sin(2\pi\Phi/\Phi_0)}_{\text{current through JJ}}. \quad (\text{A.11})$$

This looks like a driven harmonic oscillator in the  $2\pi\Phi/\Phi_0 \ll 1$  limit [see Eq. (A.6)].

By inspection, the Lagrangian that reproduces this equation of motion is

$$\mathcal{L} = \frac{1}{2}C_q \dot{\Phi}^2 + \frac{1}{2}C_{xy}(\dot{\Phi} - V_d(t))^2 + E_J(\cos(2\pi\Phi/\Phi_0) - 1), \quad (\text{A.12})$$

where  $E_J = I_{0q}\Phi_0/(2\pi)$  [see Eq. (2.19)]. From the canonical momentum

$$Q = \frac{\partial \mathcal{L}}{\partial \dot{\Phi}} = (C_{xy} + C_q)\dot{\Phi} - C_{xy}V_d(t), \quad (\text{A.13})$$

we find that

$$\dot{\Phi} = \frac{Q + C_{xy}V_d(t)}{C_\Sigma}, \quad (\text{A.14})$$

where  $C_\Sigma \equiv C_{xy} + C_q$ . Therefore, the Hamiltonian for this circuit can be written as

$$\begin{aligned} H &= \dot{\Phi}Q - \mathcal{L} \\ &= \frac{Q^2}{C_\Sigma} + \frac{C_{xy}}{C_\Sigma}QV_d(t) - \left( \frac{1}{2C_\Sigma} \left[ Q^2 + 2C_{xy}QV_d(t) + \cancel{C_{xy}^2 V_d(t)^2} \right] \right. \\ &\quad \left. - \frac{C_{xy}}{C_\Sigma}QV_d(t) - \cancel{\frac{C_{xy}^2}{C_\Sigma} V_d(t)^2} + \cancel{\frac{C_{xy}}{2} V_d(t)^2} + E_J(\cos(2\pi\Phi/\Phi_0) - 1) \right) \\ &= \frac{Q^2}{2C_\Sigma} - E_J(\cos(2\pi\Phi/\Phi_0) - 1) + \frac{C_{xy}}{C_\Sigma}QV_d(t). \end{aligned} \quad (\text{A.15})$$

We can express this equation in a more familiar form [27] by introducing the phase operator [see Eq. (2.20)]

$$\hat{\delta} = 2\pi\hat{\Phi}/\Phi_0,$$

Cooper pair number operator

$$\hat{n} = -\hat{Q}/2e,$$

and offset charge

$$n_g = +C_{xy}V_d/2e.$$

Using these definitions, Eq. (A.15) can be written as<sup>3</sup>

$$H = 4E_C(\hat{n} - n_g)^2 - E_J \cos(\hat{\delta}) + \cancel{E_J} - \cancel{4E_C n_g^2}. \quad (\text{A.16})$$

Typically, the offset charge is assumed to have contributions from both the drive source and the environment. In a well-designed system, the charge noise due to the drive source can largely be ignored. However, the environmental contribution can lead to enhanced dephasing (depending on the  $E_J/E_C$  ratio), relaxation, and excitation.

## A.4 From $\hat{Q}$ and $\hat{\Phi}$ to Pauli Matrices

As discussed in Section 2.3, the transmon is a weakly anharmonic oscillator with eigenstates that closely resemble those of the harmonic oscillator. This leads to a major simplification when analyzing the transmon, as we can approximate this system as a harmonic oscillator during calculations, while still gaining valuable intuition about the circuit's behavior. We explore this concept below to demonstrate how the 'harmonic transmon' can be mapped onto a nearly equivalent Pauli matrix representation.

---

<sup>3</sup>From the definitions of  $\hat{n}$  and  $\hat{\delta}$ , the canonical commutation relation can be written in dimensionless form as  $[\hat{n}, \hat{\delta}] = +i$ .

Throughout this discussion, we will highlight situations where these approximations lead to problems.

By approximating the transmon as a harmonic oscillator<sup>4</sup> and truncating the eigenbasis to the first two energy levels, one can show that the following mappings can be made:

- $\hat{a} \rightarrow \hat{\sigma}_-$
- $\hat{a}^\dagger \rightarrow \hat{\sigma}_+$
- $\hat{a} + \hat{a}^\dagger \rightarrow \hat{\sigma}_x$
- $i(\hat{a}^\dagger - \hat{a}) \rightarrow \hat{\sigma}_y$
- $1 - 2\hat{a}^\dagger\hat{a} \rightarrow \hat{\sigma}_z$

Here,  $\hat{\sigma}_x$ ,  $\hat{\sigma}_y$ , and  $\hat{\sigma}_z$  denote the usual Pauli matrices<sup>5</sup>,  $\hat{\sigma}_+ \equiv |1_p\rangle\langle 0_p|$  and  $\hat{\sigma}_- \equiv |0_p\rangle\langle 1_p|$  are the Pauli raising and lower operators, and  $\hat{a}^\dagger$  and  $\hat{a}$  are the creation and annihilation operators of harmonic oscillator excitations. To show this, we denote the basis states of the harmonic oscillator (Pauli- $z$  matrix) using the subscript h (p) in the calculation below:

- $\hat{a}|0_h\rangle = 0 \quad \leftrightarrow \quad \hat{\sigma}_-|0_p\rangle = |0_p\rangle\langle 1_p|0_p\rangle \stackrel{0}{=} 0$
- $\hat{a}|1_h\rangle = \sqrt{1}|0_h\rangle \quad \leftrightarrow \quad \hat{\sigma}_-|1_p\rangle = |0_p\rangle$

---

<sup>4</sup>The harmonic approximation means that  $\hat{H}_0 \approx \hbar\omega_0(\hat{a}^\dagger\hat{a} + 1/2)$  and  $\hat{Q} \approx Q_{\text{zpf}} \times j(\hat{a}^\dagger - \hat{a})$ , where  $\omega_0 = \sqrt{8E_J E_C}/\hbar$  and  $Q_{\text{zpf}} = \sqrt{\hbar\omega_0 C_q/2}$  [see Eq. (2.11)].

<sup>5</sup>With eigenstate convention  $\hat{\sigma}_z|0_p\rangle = +|0_p\rangle$  and  $\hat{\sigma}_z|1_p\rangle = -|1_p\rangle$ .

- $\hat{a}^\dagger|0_h\rangle = \sqrt{1}|1_h\rangle \leftrightarrow \hat{\sigma}_+|0_p\rangle = |1_p\rangle$
- $\hat{a}^\dagger|1_h\rangle = \sqrt{2}|2_h\rangle \stackrel{0}{=} 0 \leftrightarrow \hat{\sigma}_+|1_p\rangle = |1_p\rangle \langle 0_p|1_p\rangle \stackrel{0}{=} 0$
- $(\hat{a} + \hat{a}^\dagger)(|0_h\rangle + |1_h\rangle) = +(|0_h\rangle + |1_h\rangle) + \sqrt{2}|2_h\rangle \stackrel{0}{=} \leftrightarrow \hat{\sigma}_x|x_+\rangle = +|x_+\rangle$
- $(\hat{a} + \hat{a}^\dagger)(|0_h\rangle - |1_h\rangle) = -(|0_h\rangle - |1_h\rangle) - \sqrt{2}|2_h\rangle \stackrel{0}{=} \leftrightarrow \hat{\sigma}_x|x_-\rangle = -|x_-\rangle$
- $i(\hat{a}^\dagger - \hat{a})(|0_h\rangle + i|1_h\rangle) = +(|0_h\rangle + i|1_h\rangle) - \sqrt{2}|2_h\rangle \stackrel{0}{=} \leftrightarrow \hat{\sigma}_y|y_+\rangle = +|y_+\rangle$
- $i(\hat{a}^\dagger - \hat{a})(|0_h\rangle - i|1_h\rangle) = -(|0_h\rangle - i|1_h\rangle) + \sqrt{2}|2_h\rangle \stackrel{0}{=} \leftrightarrow \hat{\sigma}_y|y_-\rangle = -|y_-\rangle$
- $(1 - 2\hat{a}^\dagger\hat{a})|0_h\rangle = +|0_h\rangle \leftrightarrow \hat{\sigma}_z|0_p\rangle = +|0_p\rangle$
- $(1 - 2\hat{a}^\dagger\hat{a})|1_h\rangle = -|1_h\rangle \leftrightarrow \hat{\sigma}_z|1_p\rangle = -|1_p\rangle.$

Here,  $|x_\pm\rangle = (|0_p\rangle \pm |1_p\rangle)/\sqrt{2}$  and  $|y_\pm\rangle = (|0_p\rangle \pm i|1_p\rangle)/\sqrt{2}$ . Notice that we have artificially set all terms  $\propto |2_h\rangle = 0$ . Clearly, this cannot hold if Fourier components of the drive signal are resonant with the  $|1\rangle \rightarrow |2\rangle$  transition; however, this is often a good approximation provided that the Rabi frequency induced by the drive signal is much smaller than the transmon's nonlinearity. As these quantities become comparable, additional pulse shaping techniques are required to avoid leakage and phase errors caused by the weakly off-resonant  $|2\rangle$  state [79, 81]. We refer the interested reader to Zijun Chen's PhD thesis for further detail [37].

From the mappings above and Eq. (A.15), we have that

$$\hat{H} \simeq \left( -\frac{\hbar\omega_0}{2} \right) \hat{\sigma}_z + \left( \frac{C_{xy}}{C_\Sigma} V_d(t) Q_{z\text{pf}} \right) \hat{\sigma}_y + \hbar\omega_q \tilde{\mathbb{1}}.$$

We note that the frequency term  $\omega_0$  in front of the  $\hat{\sigma}_z$  operator from this Hamiltonian should be replaced by  $\omega_q = (\omega_0 - E_C/\hbar)$  to obtain a more accurate approximation of the qubit frequency (see Section 2.3), in other words

$$\hat{H} = \underbrace{\left(-\frac{\hbar\omega_0 - E_C}{2}\right)}_{=\hat{H}_0} \hat{\sigma}_z + \underbrace{\left(\frac{C_{xy}}{C_\Sigma} V_d(t) Q_{z\text{zpf}}\right)}_{=\hat{H}_d(t)} \hat{\sigma}_y. \quad (\text{A.17})$$

In addition, we note that the prefactor in front of the  $\hat{\sigma}_x$  operator was estimated using the harmonic oscillator wavefunctions, and therefore differs slightly from the expression obtained using the transmon's wavefunctions [see Fig. 2.2(c)]. At any rate, this expression captures the correct leading order dependencies, and provides us with a compact set of design rules for building driven transmon systems.

## A.5 Resonant Drives and the RWA

In this section, we study the action of the drive term  $\hat{H}_d(t)$  from Eq. (A.17) by assuming that

$$V_d(t) = |V_d| \cdot X(t) \times \sin(\omega_d t + \phi_d), \quad (\text{A.18})$$

where  $|V_d|$  is the drive amplitude,  $\omega_d$  is the drive frequency,  $\phi_d$  is the drive phase, and  $X(t)$  is a time-dependent window function. Let us begin by introducing the time evolution operator

$$\hat{U} = \exp(-i\hat{H}_0 t/\hbar) = \exp(+i\frac{\omega_q}{2} t \hat{\sigma}_z). \quad (\text{A.19})$$

Then, in the interaction picture, the drive term is altered by the unitary transformation

$$\hat{H}_I(t) = \hat{U}^\dagger \hat{H}_d(t) \hat{U} = \hbar \Omega_R X(t) \hat{U}^\dagger \hat{\sigma}_y \hat{U}, \quad (\text{A.20})$$

where

$$\Omega_R = Q_{\text{zpf}} |V_d| \frac{C_{xy}}{C_\Sigma} / \hbar \quad (\text{A.21})$$

is the angular ‘Rabi frequency’. There are multiple ways to calculate the  $\hat{U}^\dagger \hat{\sigma}_y \hat{U}$  term.

The laborious method relies on the Baker-Campbell-Hausdorff relations. The first few terms in the expansion are given below for completeness:

$$\begin{aligned} \hat{U}^\dagger \hat{\sigma}_y \hat{U} &= \hat{\sigma}_y + \frac{(-i\omega_q t/2)}{1!} \underbrace{[\hat{\sigma}_z, \hat{\sigma}_y]}_{=-2i\hat{\sigma}_x} + \frac{(-i\omega_q t/2)^2}{2!} \underbrace{[\hat{\sigma}_z, [\hat{\sigma}_z, \hat{\sigma}_y]]}_{=4\hat{\sigma}_y} + \dots \\ &= \hat{\sigma}_y \cos(\omega_q t) - \hat{\sigma}_x \sin(\omega_q t). \end{aligned} \quad (\text{A.22})$$

Note that each commutator generates a factor of two in a manner that cancels out the powers of  $1/2$  generated by the  $(-i\omega_q t/2)^n$  terms, thus reproducing the expansions of  $\cos(\omega_q t)$  and  $-\sin(\omega_q t)$ . Alternatively, we can think about the physics of the transformation we are making – in other words, what do the Pauli operators in the lab frame look like from the standpoint of an observer that rotates about the  $z$ -axis at an angular frequency  $-\omega_q$ ? We know that after a quarter period in the rotating frame, the  $\hat{\sigma}_y$  operator of the lab frame will align with  $-\hat{\sigma}_x$  of the rotating frame<sup>6</sup>. Similar arguments can be made at  $1/2$  and  $3/4$  of a period until the trend is obvious (see Fig.

---

<sup>6</sup>Recall that our qubit Hamiltonian is  $\propto -\hat{\sigma}_z$  and not  $+\hat{\sigma}_z$ , hence the rotation about the minus  $z$ -axis.

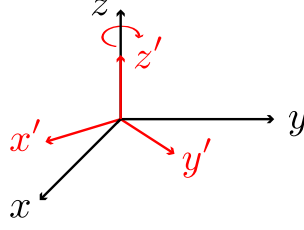


Figure A.2: Visual representation of the frame transformation from Eq. (A.22). Here, the coordinates  $x$ ,  $y$ , and  $z$  denote the lab frame and the coordinates  $x'$ ,  $y'$ , and  $z'$  denote the frame rotating about the  $z = z'$  axis at the angular frequency  $-\omega_q$ .

A.2).

Substituting Eq. (A.22) into Eq. (A.20), one finds that

$$\begin{aligned}
\hat{H}_I(t) &= \hbar\Omega_R X(t) \sin(\omega_d t + \phi_d) \times \left[ \hat{\sigma}_y \cos(\omega_q t) - \hat{\sigma}_x \sin(\omega_q t) \right] \\
&= \frac{\hbar\Omega_R X(t)}{2} \left[ \frac{\hat{\sigma}_y}{2i} \times \left[ \exp\left(i(\delta\omega_d + \phi_d)\right) - \exp\left(-i(\delta\omega_d + \phi_d)\right) \right. \right. \\
&\quad \left. \left. + \exp\left(i(\delta\omega_\Sigma + \phi_d)\right) - \exp\left(-i(\delta\omega_\Sigma + \phi_d)\right) \right] \right. \\
&\quad \left. - \frac{\hat{\sigma}_x}{2} \times \left[ \exp\left(i(\delta\omega_d + \phi_d)\right) + \exp\left(-i(\delta\omega_d + \phi_d)\right) \right. \right. \\
&\quad \left. \left. - \exp\left(i(\delta\omega_\Sigma + \phi_d)\right) - \exp\left(-i(\delta\omega_\Sigma + \phi_d)\right) \right] \right] \\
&= \hbar\Omega_R X(t) \times \left[ \frac{\hat{\sigma}_y}{2} \left( \sin(\delta\omega_d t + \phi_d) + \cancel{\sin(\omega_\Sigma t + \phi_d)} \right) \right. \\
&\quad \left. - \frac{\hat{\sigma}_x}{2} \left( \cos(\delta\omega_d t + \phi_d) - \cancel{\cos(\omega_\Sigma t + \phi_d)} \right) \right],
\end{aligned} \tag{A.23}$$

where  $\delta\omega_d \equiv \omega_d - \omega_q$ , and  $\omega_\Sigma \equiv \omega_d + \omega_q$ . Note that one-half of the signal is thrown away as counter-rotating terms; however, their participation in the dynamical description of

the system is negligible<sup>7</sup>. Taking  $\delta\omega_d = 0$  yields the drive term

$$\boxed{\hat{H}_I(t)/\hbar \simeq \Omega_R X(t) \times \left( \frac{\hat{\sigma}_y}{2} \sin(\phi_d) - \frac{\hat{\sigma}_x}{2} \cos(\phi_d) \right)}. \quad (\text{A.24})$$

From Eq. (A.24), it is clear how  $X$ - and  $Y$ -gates are achieved experimentally using microwave signals: for an  $X$ -gate ( $Y$ -gate) set  $\phi_d = \pi$  ( $\phi_d = \pi/2$ ) until the accumulated rotation angle equals  $\pi$ . We refer the interested reader to Daniel Sank's PhD thesis for further detail [100].

Now consider an alternative drive signal of the form

$$V'_d(t) = |V_d| \times \left( Y(t) \cos(\omega_q t) - X(t) \sin(\omega_q t) \right). \quad (\text{A.25})$$

The  $-X(t) \sin(\omega_q t)$  term follows from Eq. (A.24) by setting  $\phi_d = \pi$ . Similarly, the  $Y(t) \cos(\omega_q t)$  term also follows from Eq. (A.24) by setting  $\phi_d = \pi/2$  and letting  $X(t) \rightarrow Y(t)$ . Combining these results, one finds that

$$\hat{H}_I(t)/\hbar \simeq \Omega_R \times \left( Y(t) \frac{\hat{\sigma}_y}{2} + X(t) \frac{\hat{\sigma}_x}{2} \right). \quad (\text{A.26})$$

This is the control Hamiltonian needed for implementing Derivative Removal by Adiabatic Gate (DRAG) [79, 80]. Using DRAG, the window functions  $X(t)$  and  $Y(t)$  are related by

$$Y(t) = -\alpha \frac{\dot{X}(t)}{\eta} \quad (\text{A.27})$$

where  $\alpha \in (0, 1.5)$  is a dimensionless prefactor and  $\eta$  is the anharmonicity [Eq. (2.24)].

---

<sup>7</sup>This is the so-called rotating wave approximation (RWA).

## A.6 Dispersive Measurement Systems

Consider the coupled transmon-resonator system depicted in Fig. 2.4. By current conservation, we have that

$$\underbrace{C_g(\ddot{\Phi}_q - \ddot{\Phi}_r)}_{\text{current through } C_g} = \underbrace{C_r \ddot{\Phi}_r}_{\text{current through } C_r} + \underbrace{\Phi_r/L_r}_{\text{current through } L_r}$$

for the currents in the resonator, and

$$\underbrace{C_g(\ddot{\Phi}_r - \ddot{\Phi}_q)}_{\text{current through } C_g} = \underbrace{C_q \ddot{\Phi}_q}_{\text{current through } C_q} + \underbrace{I_{0q} \sin(2\pi\Phi_q/\Phi_0)}_{\text{current through JJ}}$$

for the currents in the transmon. The Lagrangian that reproduces these equations of motion is

$$\begin{aligned} \mathcal{L} = & \frac{1}{2}C_r\dot{\Phi}_r^2 + \frac{1}{2}C_q\dot{\Phi}_q^2 + \frac{1}{2}C_g(\dot{\Phi}_r - \dot{\Phi}_q)^2 \\ & - \frac{\Phi_r^2}{2L_r} + E_J(\cos(2\pi\Phi_q/\Phi_0) - 1), \end{aligned} \quad (\text{A.28})$$

where  $E_J = I_{0q}\Phi_0/2\pi$ . Rewriting the kinetic portion of this Lagrangian as

$$T = \frac{1}{2}(C_r + C_g)\dot{\Phi}_r^2 + \frac{1}{2}(C_q + C_g)\dot{\Phi}_q^2 - C_g\dot{\Phi}_r\dot{\Phi}_q,$$

one finds that

$$\begin{aligned} T &= \frac{1}{2} \begin{bmatrix} \dot{\Phi}_r & \dot{\Phi}_q \end{bmatrix} \underbrace{\begin{bmatrix} (C_r + C_g) & -C_g \\ -C_g & (C_q + C_g) \end{bmatrix}}_C \begin{bmatrix} \dot{\Phi}_r \\ \dot{\Phi}_q \end{bmatrix} \\ &= \frac{1}{2} \dot{\Phi}^T C \dot{\Phi} \end{aligned} \quad (\text{A.29})$$

when written in matrix form. From the definition of conjugate momentum, we find that

$$\begin{aligned}
Q &= \begin{bmatrix} \partial\mathcal{L}/\partial\dot{\Phi}_r \\ \partial\mathcal{L}/\partial\dot{\Phi}_q \end{bmatrix} \\
&= \begin{bmatrix} (C_r + C_g)\dot{\Phi}_r - C_g\dot{\Phi}_q \\ -C_g\dot{\Phi}_r + (C_q + C_g)\dot{\Phi}_q \end{bmatrix} \\
&= \underbrace{\begin{bmatrix} (C_r + C_g) & -C_g \\ -C_g & (C_q + C_g) \end{bmatrix}}_{=C} \begin{bmatrix} \dot{\Phi}_r \\ \dot{\Phi}_q \end{bmatrix} \\
&= C\dot{\Phi}. \tag{A.30}
\end{aligned}$$

Interestingly, the expression for  $T$  and  $Q$  are related by the same capacitance matrix  $C$ . Since  $C$  is invertible, Eq. (A.30) implies that  $\dot{\Phi} = C^{-1}Q$ , allowing us to express Eq. (A.29) as

$$T = \frac{1}{2}\dot{\Phi}^T Q \tag{A.31}$$

$$\begin{aligned}
&= \frac{1}{2}(C^{-1}Q)^T C(C^{-1}Q) \\
&= \frac{1}{2}Q^T C^{-1}Q. \tag{A.32}
\end{aligned}$$

In the last line of this expression, we have used the fact that  $(C^{-1})^T = C^{-1}$ , as  $C$  is symmetric. Then, from Eqs. (A.31) and (A.32), the Hamiltonian for this system is given by [19]

$$\begin{aligned}
H &= \dot{\Phi}^T Q - \mathcal{L} \\
&= \dot{\Phi}^T Q - \left( \frac{1}{2} \dot{\Phi}^T Q - \frac{\Phi_r^2}{2L_r} + E_J(\cos(2\pi\Phi_q/\Phi_0) - 1) \right) \\
&= \frac{1}{2} \dot{\Phi}^T Q + \frac{\Phi_r^2}{2L_r} - E_J(\cos(2\pi\Phi_q/\Phi_0) - 1) \\
&= \underbrace{\frac{1}{2} Q^T C^{-1} Q}_{=T} + \frac{\Phi_r^2}{2L_r} - E_J(\cos(2\pi\Phi_q/\Phi_0) - 1). \tag{A.33}
\end{aligned}$$

To make use of Eq. (A.33), we compute the expression for  $C^{-1}$  below

$$C^{-1} = \frac{1}{\det(C)} \begin{bmatrix} (C_q + C_g) & C_g \\ C_g & (C_r + C_g) \end{bmatrix}, \tag{A.34}$$

where  $\det(C) = (C_r + C_g)(C_q + C_g) - C_g^2$ . Plugging Eq. (A.34) into Eq. (A.32) yields the expression

$$\begin{aligned}
T &= \frac{1}{2} \begin{bmatrix} Q_r & Q_q \end{bmatrix} \frac{1}{\det(C)} \begin{bmatrix} (C_q + C_g) & C_g \\ C_g & (C_r + C_g) \end{bmatrix} \begin{bmatrix} Q_r \\ Q_q \end{bmatrix} \\
&= \frac{Q_r^2}{2C'_r} + \frac{Q_q^2}{2C'_q} + \frac{Q_r Q_q}{C'_g}, \tag{A.35}
\end{aligned}$$

where

$$C'_r = C_r + \frac{C_q C_g}{C_q + C_g} \quad (\text{A.36})$$

$$C'_q = C_q + \frac{C_r C_g}{C_r + C_g} \quad (\text{A.37})$$

$$C'_g = \frac{(C_r + C_g)(C_q + C_g) - C_g^2}{C_g}. \quad (\text{A.38})$$

The equation for  $C'_r$  ( $C'_q$ ) is simply the capacitance of  $C_r$  ( $C_q$ ) in parallel with the series combination of  $C_g$  and  $C_q$  ( $C_r$ ). Finally, by Eq. (A.35), the Hamiltonian is given by

$$H = \underbrace{\frac{Q_r^2}{2C'_r} + \frac{\Phi_r^2}{2L_r}}_{=H_r} + \underbrace{\frac{Q_q^2}{2C'_q} - E_J(\cos(2\pi\Phi_q/\Phi_0) - 1)}_{=H_q} + \underbrace{\frac{Q_r Q_q}{C'_g}}_{=H_g}. \quad (\text{A.39})$$

This looks like the Hamiltonian for a resonator ( $H_r$ ), plus the Hamiltonian for a transmon ( $H_q$ ), along with a ‘small’ coupling term ( $H_g$ ). As usual, we promote  $\Phi_j$  and  $Q_j$  to operators satisfying the canonical commutation relation  $[\hat{\Phi}_j, \hat{Q}_j] = i\hbar$  for  $j \in \{r, q\}$ .

The coupling term from Eq. (A.39) can be written as<sup>8</sup>

$$\begin{aligned}\hat{H}_g &= \frac{\hat{Q}_r \hat{Q}_q}{C'_g} \\ &= \frac{Q_{r,\text{zpf}} Q_{q,\text{zpf}}}{C'_g} i(\hat{a}_r^\dagger - \hat{a}_r) i(\hat{a}_q^\dagger - \hat{a}_q)\end{aligned}\quad (\text{A.40})$$

$$= \hbar g (\hat{a}_r^\dagger - \hat{a}_r) (\hat{a}_q - \hat{a}_q^\dagger), \quad (\text{A.41})$$

where  $Q_{j,\text{zpf}} = \sqrt{\hbar \omega_j C'_j / 2}$  and  $\omega_j = 1 / \sqrt{C'_j L_j}$  (see Sections 2.1 and 2.3). Noting that in practical cases  $C'_r \simeq C_r + C_g$ ,  $C'_q \simeq C_q + C_g$ , and  $C'_g \simeq (C_r + C_g)(C_q + C_g) / C_g$ , the expression for  $g$  from Eq. (A.41) is

$$g \simeq \frac{\sqrt{\omega_r \omega_q}}{2} \frac{C_g}{\sqrt{(C_r + C_g)(C_q + C_g)}}. \quad (\text{A.42})$$

This is a fundamental design formula for dispersive measurement systems involving transmons. Letting  $\hat{a}_r^\dagger \rightarrow \hat{a}^\dagger$ ,  $\hat{a}_r \rightarrow \hat{a}$ ,  $\hat{a}_q^\dagger \rightarrow \hat{\sigma}_+$ ,  $\hat{a}_q \rightarrow \hat{\sigma}_-$ , and  $1 - 2\hat{a}_q^\dagger \hat{a}_q \rightarrow \hat{\sigma}_z$  (see Appendix A.4), the coupling term can be written as

$$\hat{H}_g = \hbar g (\hat{a}^\dagger - \hat{a}) (\hat{\sigma}_- - \hat{\sigma}_+), \quad (\text{A.43})$$

and therefore our Hamiltonian is of the form

$$\hat{H} / \hbar = \omega_r (\hat{a}^\dagger \hat{a} + \frac{1}{2}) + \omega_q (-\frac{1}{2} \hat{\sigma}_z + 1) + g (\hat{a}^\dagger - \hat{a}) (\hat{\sigma}_- - \hat{\sigma}_+). \quad (\text{A.44})$$

---

<sup>8</sup>This form of the coupling term assumes that we are treating the transmon as a harmonic oscillator plus a small perturbation. This means that the matrix elements of the coupling term  $\hat{H}_g$  should be evaluated with respect to the perturbed eigenfunctions, rather than those of the harmonic oscillator alone when dealing with the transmon's states; however, to streamline our discussion, we will forgo these corrections and refer the interested reader to the excellent PhD thesis by Mostafa Khezri for further detail [38].

Dropping all constants, we find that

$$\boxed{\hat{H}/\hbar = \omega_r \hat{a}^\dagger \hat{a} - \frac{\omega_q}{2} \hat{\sigma}_z + g(\hat{a}^\dagger \hat{\sigma}_- - \hat{a} \hat{\sigma}_+ - \hat{a} \hat{\sigma}_- + \hat{a} \hat{\sigma}_+)} . \quad (\text{A.45})$$

This is the celebrated Jaynes-Cummings Hamiltonian.

To get Eq. (A.45) into a more useful form, we define the bare Hamiltonian

$$\hat{H}_0/\hbar = \omega_r \hat{a}^\dagger \hat{a} - \frac{\omega_q}{2} \hat{\sigma}_z, \quad (\text{A.46})$$

with the corresponding time evolution operator

$$\hat{U} = \exp(-i\hat{H}_0 t/\hbar). \quad (\text{A.47})$$

Then, in the interaction picture, Eq. (A.43) can be written as

$$\hat{H}_I(t) = \hat{U}^\dagger \hat{H}_g \hat{U}. \quad (\text{A.48})$$

Using the Baker-Cambell-Hausdorff relation

$$e^{\hat{A}} \hat{B} e^{-\hat{A}} = \hat{B} + [\hat{A}, \hat{B}] + \frac{1}{2} [\hat{A}, [\hat{A}, \hat{B}]] + \dots + \frac{1}{n!} \overbrace{[\hat{A}, [\hat{A}, \dots [\hat{A}, \hat{B}] \dots]}^{n \text{ A's}} + \dots, \quad (\text{A.49})$$

one finds that

$$\begin{aligned} \hat{U}^\dagger \hat{a}^\dagger \hat{U} &= \hat{a}^\dagger + i\omega_r t [\hat{a}^\dagger \hat{a}, \hat{a}^\dagger] - \frac{(\omega_r t)^2}{2} [\hat{a}^\dagger \hat{a}, [\hat{a}^\dagger \hat{a}, \hat{a}^\dagger]] + \dots \\ &= \hat{a}^\dagger e^{+i\omega_r t} \end{aligned} \quad (\text{A.50})$$

and

$$\begin{aligned}\hat{U}^\dagger \hat{a} \hat{U} &= \hat{a} + i\omega_r t [\hat{a}^\dagger \hat{a}, \hat{a}] - \frac{(\omega_r t)^2}{2} [\hat{a}^\dagger \hat{a}, [\hat{a}^\dagger \hat{a}, \hat{a}]] + \dots \\ &= \hat{a} e^{-i\omega_r t}.\end{aligned}\tag{A.51}$$

These equations follow from the fact that  $[\hat{a}^\dagger \hat{a}, \hat{a}^\dagger] = \hat{a}^\dagger$  and  $[\hat{a}^\dagger \hat{a}, \hat{a}] = -\hat{a}$ . The term  $\hat{U}^\dagger \hat{\sigma}_y \hat{U}$  was derived in Appendix A.5, with the result given below

$$\hat{U}^\dagger \hat{\sigma}_y \hat{U} = \hat{\sigma}_y \cos(\omega_q t) - \hat{\sigma}_x \sin(\omega_q t).$$

Using similar methods, one can show that

$$\hat{U}^\dagger \hat{\sigma}_x \hat{U} = \hat{\sigma}_x \cos(\omega_q t) + \hat{\sigma}_y \sin(\omega_q t).$$

Since  $\hat{\sigma}_- = (\hat{\sigma}_x + i\hat{\sigma}_y)/2$  and  $\hat{\sigma}_+ = (\hat{\sigma}_x - i\hat{\sigma}_y)/2$  under our convention<sup>9</sup>, we find that

$$\hat{U}^\dagger \hat{\sigma}_- \hat{U} = \hat{\sigma}_- e^{-i\omega_q t}\tag{A.52}$$

and

$$\hat{U}^\dagger \hat{\sigma}_+ \hat{U} = \hat{\sigma}_+ e^{+i\omega_q t}.\tag{A.53}$$

Combining Eqs. (A.50)-(A.53), the transformed coupling term can be written as

$$\hat{H}_I(t) = \hbar g (\hat{a}^\dagger \hat{\sigma}_- e^{-i\Delta t} - \hat{a}^\dagger \hat{\sigma}_+ e^{i\Sigma t} - \hat{a} \hat{\sigma}_- e^{-i\Sigma t} + \hat{a} \hat{\sigma}_+ e^{i\Delta t}),\tag{A.54}$$

where  $\Delta = \omega_q - \omega_r$  and  $\Sigma = \omega_q + \omega_r$ . To first order in  $\hat{H}_g$ , time evolution in the

---

<sup>9</sup>Typically, one uses the convention  $\hat{\sigma}_\pm = (\hat{\sigma}_x \pm i\hat{\sigma}_y)/2$ , where  $|g\rangle = |\uparrow\rangle$  and  $|e\rangle = |\downarrow\rangle$ . In this case, the  $\pm$  refer to how the operator acts on the spin state.

interaction picture is equivalent to the action of

$$\hat{U}_I(t) = 1 - \frac{i}{\hbar} \int_0^t dt' \hat{H}_I(t'). \quad (\text{A.55})$$

Acting  $\hat{U}_I(t)$  on the bare states, one arrives at terms  $\propto 1/\Sigma$  and  $\propto 1/\Delta$ . Since  $|\Delta| \ll \Sigma$ , the terms  $\propto 1/\Sigma$  are much weaker; furthermore, they oscillate rapidly compared to the  $\exp(\pm i\Delta t)$  terms. Dropping the  $\exp(\pm i\Sigma t)$  terms and moving back into the lab frame yields the coupling term

$$\hat{H}_g \simeq \hbar g(\hat{a}^\dagger \hat{\sigma}_- + \hat{a} \hat{\sigma}_+). \quad (\text{A.56})$$

This means that under the RWA, the Jaynes-Cummings Hamiltonian from Eq. (A.45) is given by

$$\boxed{\hat{H}_{\text{RWA}}/\hbar = \omega_r \hat{a}^\dagger \hat{a} - \frac{\omega_q}{2} \sigma_z + g(\hat{a}^\dagger \hat{\sigma}_- + \hat{a} \hat{\sigma}_+)} \quad (\text{A.57})$$

We note that  $\hat{H}_{\text{RWA}}$  preserves the total number of excitations in the system. This means that only the states  $|n, e\rangle$  and  $|n+1, g\rangle$  are coupled, thus greatly reducing the number of nonzero matrix elements<sup>10</sup>. As we will demonstrate in the following section,  $\hat{H}_{\text{RWA}}$  is an exactly solvable Hamiltonian.

---

<sup>10</sup>To avoid confusion between the joint transmon-resonator states, we will denote the resonator states via  $|n\rangle$  where  $n \in \{0, 1, 2, \dots\}$  and the qubit states via  $|g\rangle, |e\rangle, |f\rangle, \dots$ , where  $|g\rangle$  is ground,  $|e\rangle$  is the first excited state,  $|f\rangle$  is the second excited state, and so on.

### A.6.1 Exact Solutions: the Eigenvalue Approach

To solve for the eigenvalues and eigenvectors of Eq. (A.57), we act this matrix on the bare eigenstates of the system<sup>11</sup>, with the first few terms listed below:

$$\begin{aligned}
\frac{\hat{H}_{\text{RWA}}}{\hbar}|0, g\rangle &= -\frac{\omega_q}{2}|0, g\rangle \\
\frac{\hat{H}_{\text{RWA}}}{\hbar}|0, e\rangle &= +\frac{\omega_q}{2}|0, e\rangle \\
\frac{\hat{H}_{\text{RWA}}}{\hbar}|1, g\rangle &= \left(-\frac{\omega_q}{2} + \omega_r\right)|1, g\rangle + g|0, e\rangle \\
\frac{\hat{H}_{\text{RWA}}}{\hbar}|1, e\rangle &= \left(\frac{\omega_q}{2} + \omega_r\right)|1, e\rangle + \sqrt{2}g|2, g\rangle \\
\frac{\hat{H}_{\text{RWA}}}{\hbar}|2, g\rangle &= \left(-\frac{\omega_q}{2} + 2\omega_r\right)|2, g\rangle + \sqrt{2}g|1, e\rangle \\
\frac{\hat{H}_{\text{RWA}}}{\hbar}|2, e\rangle &= \left(\frac{\omega_q}{2} + 2\omega_r\right)|2, e\rangle + \sqrt{3}g|3, g\rangle \\
&\vdots
\end{aligned}$$

To impose that  $\langle 0, g | \hat{H}_{\text{RWA}} | 0, g \rangle = 0$ , we temporarily add  $\hat{1} \times \hbar\omega_q/2$  to our Hamiltonian.

Then, in terms of the bare eigenstates, we find that  $\hat{H}_{\text{RWA}}$  is given by

$$\hat{H}_{\text{RWA}}/\hbar = \begin{matrix} & |0, g\rangle & |0, e\rangle & |1, g\rangle & |1, e\rangle & |2, g\rangle & \cdots \\ \begin{matrix} \langle 0, g| \\ \langle 0, e| \\ \langle 1, g| \\ \langle 1, e| \\ \langle 2, g| \\ \vdots \end{matrix} & \left( \begin{array}{cccccc} 0 & 0 & 0 & 0 & 0 & \cdots \\ 0 & \omega_q & g & 0 & 0 & \cdots \\ 0 & g & \omega_r & 0 & 0 & \cdots \\ 0 & 0 & 0 & \omega_q + \omega_r & \sqrt{2}g & \cdots \\ 0 & 0 & 0 & \sqrt{2}g & 2\omega_r & \cdots \\ \vdots & \vdots & \vdots & \vdots & \vdots & \ddots \end{array} \right) \end{matrix} \quad (\text{A.58})$$

<sup>11</sup>Here, by *bare eigenstates* we mean the joint eigenstates of the Hamiltonian  $H_r + H_q$  from Eq. (A.39), by pretending that the coupling term  $H_g$  is not there. This is subtly different than setting  $C_g = 0$ .

In general, the  $n^{\text{th}}$  block of this matrix is<sup>12</sup>

$$\hat{H}_{\text{RWA},n}/\hbar = \begin{array}{c} |n, e\rangle \\ \langle n, e| \\ \langle n+1, g| \end{array} \begin{array}{cc} & |n+1, g\rangle \\ \left( \begin{array}{cc} \omega_q + n\omega_r & \sqrt{n+1}g \\ \sqrt{n+1}g & (n+1)\omega_r \end{array} \right) & \end{array}. \quad (\text{A.59})$$

To simplify our analysis, we temporarily subtract  $\hat{1} \times (n+1)\hbar\omega_r$  from  $\hat{H}_{\text{RWA},n}$ . Introducing the notation  $\Delta \equiv \omega_q - \omega_r$  and solving for the eigenvalues of the matrix below

$$\begin{array}{c} |n, e\rangle \\ \langle n, e| \\ \langle n+1, g| \end{array} \begin{array}{cc} & |n+1, g\rangle \\ \left( \begin{array}{cc} \Delta & \sqrt{n+1}g \\ \sqrt{n+1}g & 0 \end{array} \right) & \end{array},$$

one finds that

$$\lambda_{\pm} = \frac{\Delta}{2} \pm \frac{\sqrt{\Delta^2 + 4(n+1)g^2}}{2}.$$

Adding  $(n+1)\omega_r$  and subtracting  $\omega_q/2$  from this equation, we find that the eigenvalues of  $\hat{H}_{\text{RWA},n}$  are

$$E_{n,\pm}/\hbar = \omega_r(n + \frac{1}{2}) \pm \frac{|\Delta|}{2} \sqrt{1 + \frac{4(n+1)g^2}{\Delta^2}}. \quad (\text{A.60})$$

The corresponding eigenvectors are

$$|n, +\rangle = \frac{1}{\sqrt{N}} \begin{bmatrix} \lambda_+ \\ g\sqrt{n+1} \end{bmatrix}$$

---

<sup>12</sup>We note that the  $n^{\text{th}}$  block  $\hat{H}_{\text{RWA}}$  corresponds to a total of  $n+1$  excitations in the resonator when the qubit is in state  $|g\rangle$ , or  $n$  excitations in the resonator when the qubit is in state  $|e\rangle$ .

and

$$|n, -\rangle = \frac{1}{\sqrt{N}} \begin{bmatrix} -g\sqrt{n+1} \\ \lambda_+ \end{bmatrix},$$

where the normalization factor

$$N = \lambda_+^2 + g^2(n+1).$$

Alternatively, these eigenvectors can be written in terms of sine and cosine as

$$|n, +\rangle = \cos \theta_n |n, e\rangle + \sin \theta_n |n+1, g\rangle \quad (\text{A.61})$$

and

$$|n, -\rangle = \cos \theta_n |n+1, g\rangle - \sin \theta_n |n, e\rangle, \quad (\text{A.62})$$

with

$$\cos \theta_n = \frac{\lambda_+}{\sqrt{\lambda_+^2 + g^2(n+1)}}$$

and

$$\sin \theta_n = \frac{g\sqrt{n+1}}{\sqrt{\lambda_+^2 + g^2(n+1)}}.$$

Computing the ratio of  $\sin \theta_n$  and  $\cos \theta_n$ , we find that

$$\tan \theta_n = \frac{g\sqrt{n+1}}{\lambda_+},$$

where  $\theta_n$  is often referred to as the ‘mixing angle’. Using the trigonometry from below

$$\begin{aligned} \tan 2\theta_n &= \frac{2 \tan \theta_n}{1 - \tan^2 \theta_n} \\ &= \frac{2\lambda_+g\sqrt{n+1}}{\lambda_+^2 - (n+1)g^2} \\ &= \frac{2\lambda_+g\sqrt{n+1}}{\frac{\Delta^2}{2} + g^2(n+1) - g^2(n+1) + \frac{\Delta}{2}\sqrt{\Delta^2 + g^2(n+1)}} \\ &= \frac{2\lambda_+g\sqrt{n+1}}{\Delta \underbrace{\left( \frac{\Delta}{2} + \frac{1}{2}\sqrt{\Delta^2 + g^2(n+1)} \right)}_{\lambda_+}} \\ &= \frac{2g\sqrt{n+1}}{\Delta}, \end{aligned}$$

one finds that

$$\boxed{\theta_n = \frac{1}{2} \arctan \left( \frac{2\sqrt{n+1}g}{\Delta} \right)}. \quad (\text{A.63})$$

We note that Eqs. (A.60)-(A.63) contain a ton of information about dispersive measurement systems as discussed in the following section.

### Asymptotics of the Exact Solutions in the Dispersive Limit

For  $\Delta > 0$ , we set  $|\Delta| = \omega_q - \omega_r$  and expand our expression for  $E_{n,\pm}$  [see Eq. (A.60)] to first order in  $|g/\Delta| \ll 1$ . The result is that

$$E_{n,\pm}/\hbar = \begin{cases} (\omega_r + |\chi|)n + \omega_q/2 + |\chi| & \text{for } + \\ (\omega_r - |\chi|)(n+1) - \omega_q/2 & \text{for } - \end{cases}, \quad (\text{A.64})$$

where  $|\chi| \equiv g^2/|\Delta|$ . This follows directly from the expansion:  $\sqrt{1+x} \approx 1 + x/2$  for  $x \ll 1$ . We note that this approximation breaks down when

$$\frac{4g^2(n+1)}{|\Delta|^2} \simeq 1,$$

in other words, at the critical photon number [41]

$$n_{\text{crit}} = \frac{1}{4} \frac{|\Delta|^2}{g^2}. \quad (\text{A.65})$$

By expanding the eigenstates given by Eqs. (A.61) and (A.62) in the  $g \ll |\Delta|$  limit, we find that the  $|n, +\rangle$  state has the most weight in  $|n, e\rangle$ , while the  $|n, -\rangle$  state has the most weight in  $|n+1, g\rangle$ . Intuitively,  $\Delta > 0 \implies \omega_q > \omega_r$ , therefore the higher energy eigenstate should have the most weight in  $|n, e\rangle$ . One typically neglects the small amount of state mixing between  $|n, e\rangle$  and  $|n+1, g\rangle$ , and directly associates  $|n, +\rangle$  with  $|n, e\rangle$ , and  $|n, -\rangle$  with  $|n+1, g\rangle$  when  $\omega_q > \omega_r$  and  $|g/\Delta| \ll 1$ .

For  $\Delta < 0$ , we set  $|\Delta| = \omega_r - \omega_q$  and expand our expression for  $E_{n,\pm}$  to first order

in  $|g/\Delta| \ll 1$ . The result is that

$$E_{n,\pm}/\hbar = \begin{cases} (\omega_r + |\chi|)(n+1) - \omega_q/2 & \text{for } + \\ (\omega_r - |\chi|)(n) + \omega_q/2 - |\chi| & \text{for } - \end{cases}, \quad (\text{A.66})$$

where again  $|\chi| \equiv g^2/|\Delta|$ . Similarly, we find that the  $|n, +\rangle$  state has the most weight in  $|n+1, g\rangle$ , while the  $|n, -\rangle$  state has the most weight in  $|n, e\rangle$ . Intuitively,  $\Delta < 0 \implies \omega_q < \omega_r$ , therefore the higher energy eigenstate should have the most weight in  $|n+1, g\rangle$ <sup>13</sup>. Again, one directly associates  $|n, +\rangle$  with  $|n+1, g\rangle$ , and  $|n, -\rangle$  with  $|n, e\rangle$  when  $\omega_r > \omega_q$  and  $|g/\Delta| \ll 1$ .

The results from Eqs. (A.64) and (A.66) are summarized graphically in Fig. A.3. From Fig. A.3(b, d), with  $\chi \equiv g^2/\Delta$  (now a signed quantity), our findings can be viewed as the assignment

$$\omega_r \rightarrow \begin{cases} \omega_r - \chi & \text{for qubit in } |g\rangle \\ \omega_r + \chi & \text{for qubit in } |e\rangle \end{cases}, \quad (\text{A.67})$$

This qubit state dependent frequency shift of the resonator is the basis of dispersive measurement system. Alternatively, these findings can be viewed as the assignment

$$\omega_q \rightarrow \omega_q + \chi(2n+1), \quad (\text{A.68})$$

in which the qubit frequency depends of the number of photons in the resonator. This is the ac Stark effect [58, 59].

---

<sup>13</sup>Be careful when expanding Eq. (A.63) for small arguments with negative denominators. The function returns  $\pi - \arg$  rather than  $\arg$ .

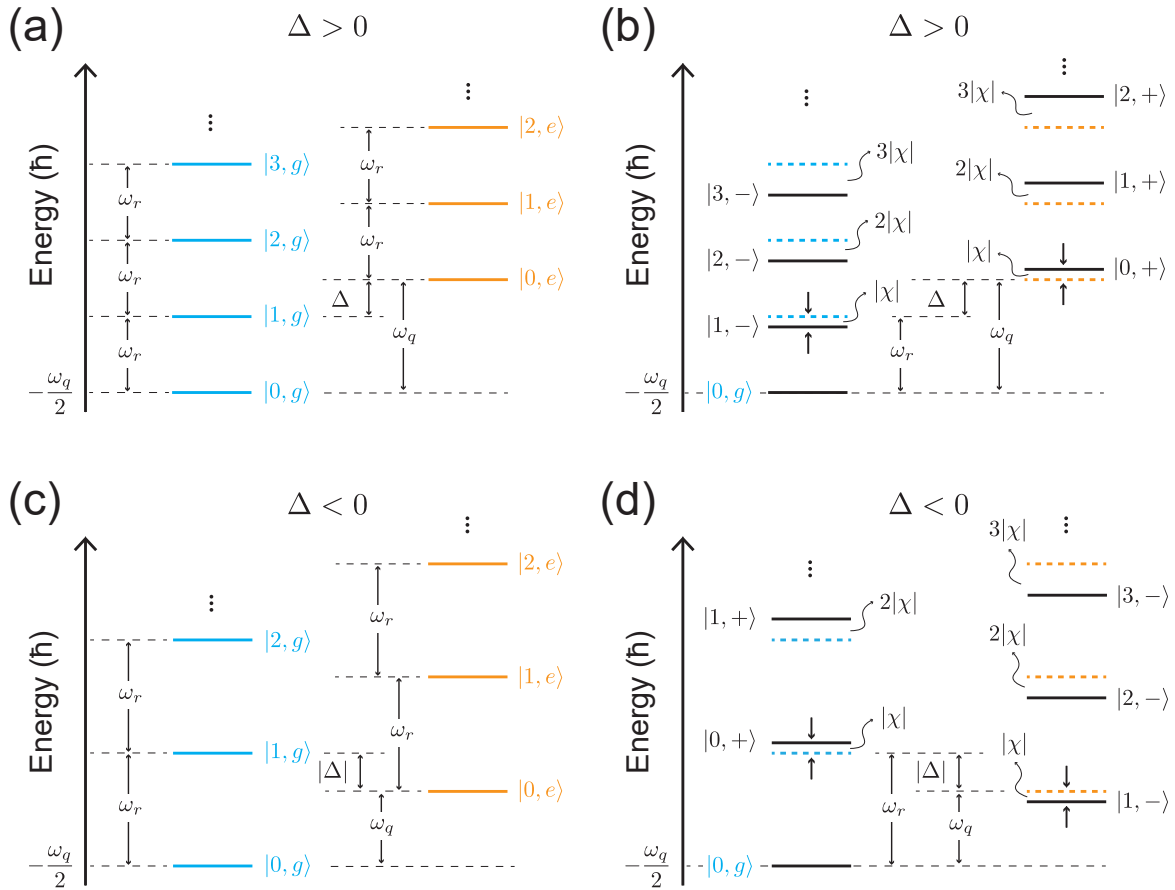


Figure A.3: **(a)** Bare energy level structure for  $\Delta > 0$ . **(b)** Dressed energy level structure for  $\Delta > 0$ . The dashed lines in this diagram correspond to the bare energy levels, while the solid lines correspond to the coupled (dressed) energy levels. **(c)** As in (a), but with  $\Delta < 0$ . **(d)** As in (b), but with  $\Delta < 0$ .

## A.6.2 Approximate Solutions: the Schrieffer–Wolff transformation

Modern treatments of the Jaynes–Cummings Hamiltonian arrive at the eigenvalues from Eqs. (A.64) and (A.66) using the Schrieffer–Wolff transformation [27, 41]. The basic idea behind this transformation is to find a generator of rotation  $\hat{R}$  such that  $[\hat{H}_0, \hat{R}] = \hat{H}_g$  [see Eqs. (A.46) and (A.56)]. Under these conditions, the unitary transformation  $\exp(\hat{R})\hat{H}_{\text{RWA}}\exp(-\hat{R})$  will diagonalize  $\hat{H}_{\text{RWA}}$  to first order in the interaction term  $\hat{H}_g$  [by Eq. (A.49)]. Introducing the operators

$$\hat{T}_+ = \hat{\sigma}_+\hat{a} + \hat{\sigma}_+\hat{a}^\dagger \quad (\text{A.69})$$

and

$$\hat{T}_- = \hat{\sigma}_+\hat{a} - \hat{\sigma}_+\hat{a}^\dagger, \quad (\text{A.70})$$

we find that the commutators

$$\begin{aligned} [\hat{T}_-, \hat{n}] &= [\hat{a}, \hat{a}^\dagger]\hat{\sigma}_+\hat{a} + \hat{\sigma}_-\hat{a}^\dagger[\hat{a}, \hat{a}^\dagger] \\ &= \hat{T}_+ \end{aligned} \quad (\text{A.71})$$

and

$$\begin{aligned}
[\hat{T}_-, \hat{\sigma}_z] &= [\hat{\sigma}_+, \hat{\sigma}_z]\hat{a} + [\hat{\sigma}_z, \hat{\sigma}_-]\hat{a}^\dagger \\
&= 2(\hat{\sigma}_+\hat{a} + \hat{\sigma}_-\hat{a}^\dagger) \\
&= 2\hat{T}_+.
\end{aligned} \tag{A.72}$$

Noting that  $\hat{H}_g \propto \hat{T}_+$ , we have identified the desired generator of rotation up to a prefactor, which happens to be  $g/\Delta$  (i.e.  $\hat{R} = (g/\Delta) \times \hat{T}_+$ ). In addition, the following identity will prove useful in the calculation below

$$\begin{aligned}
[\hat{T}_-, \hat{T}_+] &= 2(\hat{\sigma}_+\hat{\sigma}_-\hat{a}\hat{a}^\dagger - \hat{\sigma}_-\hat{\sigma}_+\hat{a}^\dagger\hat{a}) \\
&= 2(\hat{\sigma}_+\hat{\sigma}_- - \hat{\sigma}_z\hat{n}).
\end{aligned} \tag{A.73}$$

The last line follows from the fact that  $\hat{a}\hat{a}^\dagger = 1 + \hat{a}^\dagger\hat{a}$ .

Then, by Eq. (A.49), to first order in  $g/\Delta$  we find that the unitary transformation

is given by

$$\begin{aligned}
\tilde{H}_{\text{RWA}} &\equiv \exp\left(\frac{g}{\Delta}\hat{T}_-\right)\hat{H}_{\text{RWA}}\exp\left(-\frac{g}{\Delta}\hat{T}_-\right) \\
&\simeq \hat{H}_{\text{RWA}} + \frac{g}{\Delta}[\hat{T}_-, \hat{H}_{\text{RWA}}] + \frac{g^2}{2\Delta^2}[\hat{T}_-, [\hat{T}_-, \hat{H}_{\text{RWA}}]] \\
&= \hat{H}_r + \hat{H}_q + \hbar g \hat{T}_+ + \frac{\hbar g}{\Delta}\left(-\Delta\hat{T}_+ + 2g(\hat{\sigma}_+\hat{\sigma}_- - \hat{\sigma}_z\hat{n})\right) \\
&+ \frac{\hbar g^2}{2\Delta^2}(-\Delta[\hat{T}_-, \hat{T}_+]) + \mathcal{O}\left(\left(\frac{g}{\Delta}\right)^2\right) \\
&= \hat{H}_r + \hat{H}_q + \frac{\hbar g^2}{\Delta}(\hat{\sigma}_+\hat{\sigma}_- - \hat{\sigma}_z\hat{n}). \tag{A.74}
\end{aligned}$$

Subtracting the constant

$$\frac{1}{2}\frac{\hbar g^2}{\Delta}(|e\rangle\langle e| + |g\rangle\langle g|) \tag{A.75}$$

from Eq. (A.74), we have that

$$\begin{aligned}
\tilde{H}_{\text{RWA}}/\hbar &= \omega_r \hat{a}^\dagger \hat{a} - \frac{\omega_q}{2} \hat{\sigma}_z - \frac{\hat{\sigma}_z}{2}(2\chi\hat{n} + \chi) \\
&= \omega_r \hat{a}^\dagger \hat{a} - \underbrace{\frac{\hat{\sigma}_z}{2}\left(\omega_q + 2\chi\left(\hat{n} + \frac{1}{2}\right)\right)}_{\text{ac Stark shift + Lamb Shift}} \\
&= \underbrace{(\omega_r - \chi\hat{\sigma}_z)\hat{a}^\dagger \hat{a}}_{\text{dispersive resonator shift}} - \underbrace{\frac{\hat{\sigma}_z}{2}(\omega_q + \chi)}_{\text{qubit + Lamb shift}}, \tag{A.76}
\end{aligned}$$

where

$$\chi = \frac{g^2}{\Delta}. \tag{A.77}$$

This is the Jaynes-Cummings Hamiltonian in the dispersive approximation. Notice that  $\tilde{H}_{\text{RWA}}$  is diagonal to first order in  $g/\Delta$ , and that the action of the unitary  $\exp(g\hat{T}_-/\Delta)$  on the dressed eigenstates from Eqs. (A.61) and (A.62) removes the state ‘mixing’ caused by the interaction to first order in  $g/\Delta$ .



# Appendix B

## Supplementary Materials for JPM

### Experiment I

#### B.1 JPM Theory

A circuit schematic for the JPM is shown in Fig. B.1(a). The JPM is based on the design of the capacitively-shunted flux-biased phase qubit [56]. Fig. B.1(b) shows a scanning electron microscopy (SEM) micrograph of the circuit with labels indicating components. The circuit Hamiltonian is given by

$$H(\delta, Q) = \frac{Q^2}{2C_s} - E_J \cos \delta + \frac{1}{2L_g} \left( \frac{\Phi_0}{2\pi} \right)^2 \left( \delta - \frac{2\pi\Phi_{\text{ext}}}{\Phi_0} \right)^2, \quad (\text{B.1})$$

where  $Q$  is the capacitor charge,  $C_s$  is the shunt capacitance (red),  $\delta$  is the phase difference across the Josephson junction,  $\Phi_0 \equiv h/2e$  is the magnetic flux quantum,  $I_0$  is

the critical current of the Josephson junction (orange),  $E_J = I_0\Phi_0/2\pi$  is the Josephson energy, and  $L_g$  is the gradiometric loop inductance (blue). The capacitance of the Josephson junction is negligible compared to  $C_s$ . The external flux  $\Phi_{\text{ext}}$  is generated by an on-chip control line (green) which is coupled to the JPM with a mutual inductance  $M$ . The extrema of the potential energy landscape are determined by the equation

$$\sin \delta = \frac{1}{\beta_L} \left( \frac{2\pi\Phi_{\text{ext}}}{\Phi_0} - \delta \right), \quad (\text{B.2})$$

where

$$\beta_L = \frac{2\pi L_g I_0}{\Phi_0}. \quad (\text{B.3})$$

Eq. (B.2) is a straightforward statement of current conservation in the JPM loop; solutions can be depicted graphically as shown in Fig. B.1(c). We seek values  $\beta_L$  which allow the JPM to be tuned between a single- and double-well regime for reset and photodetection, respectively. The curvature at the local minima of the potential determines the plasma frequency:

$$\omega_p = \frac{2\pi}{\Phi_0} \left[ \frac{1}{C_s} \frac{\partial^2 U}{\partial \delta^2} \right]^{1/2}. \quad (\text{B.4})$$

In addition, we can estimate the number of levels in a well by  $n \approx \Delta U/\hbar\omega_p$ , where  $\Delta U$  is the potential energy barrier height.

## B.2 JPM Fabrication

The JPM is fabricated on a high-resistivity Si substrate. Prior to deposition, the wafer is dipped in HF acid to remove native oxide from the surface. Next, we quickly transfer ( $\sim 1$  min) the device into a high vacuum (HV) sputter tool to deposit a 100 nm-thick film of Al. The first patterning step defines all Al features except for the wiring crossovers, Josephson junction, and shunt capacitor [see Fig. B.1(b)]. The pattern is wet-etched using Transene Aluminum Etchant Type A. After this, a 130 nm-thick film of amorphous SiO<sub>2</sub> is deposited using plasma-enhanced chemical vapor deposition (PECVD). Next, we define a 1  $\mu\text{m}^2$  via in the dielectric which determines the location of our Josephson junction. Josephson junctions are formed in the sputter tool using the following steps: i) *in situ* ion mill to remove native oxide, ii) controlled oxidation in pure O<sub>2</sub> at room temperature ( $P_{\text{O}_2} \sim 10$  mTorr), and iii) deposition of the Al counterelectrode ( $\sim 150$  nm thick). The counterelectrode layer is then patterned and etched using the same Al etching procedure as before. Next, we pattern for dielectric removal using a reactive-ion etcher (RIE). Dielectric is cleared throughout except where needed for wiring insulation. A final Al wiring step is completed using liftoff and e-beam evaporation in a separate HV system. Once again an *in situ* ion mill is used to ensure good metal-to-metal contact, a 5 nm layer of Ti is evaporated to promote adhesion, then a 150 nm-thick film of Al is evaporated and the metal is lifted off. This completes the device. Circuit parameters for the JPM chip are listed in Table B.1 with

component labels indicated in Fig. B.2(a).

### B.3 Qubit Fabrication

The transmon qubit and readout cavity are fabricated on a high-resistivity Si substrate. A 90-nm Nb film is deposited using a dc sputter system. A single photolithography step defines all features, except for the Josephson junctions. This pattern is etched using a reactive-ion etcher. The Dolan-bridge qubit junctions are defined in an MMA/PMMA bilayer exposed on an electron-beam writer. The junctions are deposited in the following steps: i) *in situ* Ar ion mill to remove native oxide from underlying Nb, ii) electron-beam evaporation of 35 nm of Al at +11.5 degrees, iii) controlled oxidation, and iv) 65 nm Al deposition at -11.5 degrees. Circuit parameters for the qubit chip are listed in Table B.2 with component labels indicated in Fig. B.2(b).

### B.4 Experimental Setup

The setup for our experiment is shown in Fig. B.3. The qubit control, qubit cavity, and JPM readout waveforms are generated through sideband mixing of shaped intermediate frequency (IF) and local oscillator (LO) tones; 1 GS/s arbitrary waveform generators (AWGs) are used to generate the IF waveforms. These IF waveforms are sent to the in-phase (I) and quadrature (Q) ports of an IQ mixer and are mixed with an LO to

generate pulses at microwave frequencies at the RF port. The qubit flux bias is fixed at a constant dc value throughout the measurement sequence. The JPM flux bias is composed of two signals which are combined at the millikelvin stage using a microwave bias tee that is dc coupled to both of its ports. The output of the qubit cavity is connected to the input of the JPM capture cavity via a coaxial transmission line with no intervening isolators or circulators. The state of the JPM is read out in reflection using a directional coupler, an isolator, and a high mobility electron transistor (HEMT) amplifier at the 3 K stage of the cryostat. The JPM readout signal is sent to the RF port of an IQ mixer where it is down-converted using the shared LO with the JPM readout AWG. Baseband I and Q signals are digitized using a 500 MS/s analog-to-digital converter (ADC). Further signal demodulation and thresholding are performed in software in order to extract the oscillation state of the JPM. In Fig. B.4(a) we show our ability to distinguish between distinct oscillation states in IQ space. The JPM state can be determined with  $> 99.9\%$  accuracy in under 500 ns [see Fig. B.4(b)].

## B.5 Pointer State Transfer

Prior work has shown the efficient absorption of coherent states by a microwave resonator coupled to a mediating transmission line [57]. These experiments relied on a tunable coupling scheme to ensure destructive interference between the incoming and outgoing microwaves, as well as the ability to control the temporal profile of the in-

Table B.1: JPM Circuit Parameters

Label	Description	Value	Method of Determination
$C_2$	Capture cavity input coupling capacitor	12 fF	Finite element simulations
$\omega_2/2\pi$	Fundamental frequency of the half-wave coplanar waveguide resonator (with JPM far detuned at 5.9 GHz)	5.03 GHz	Cavity spectroscopy
$L_2$	Approximate length of the capture cavity	12 mm	Defined lithographically
$C_{lumped}$	Equivalent lumped element capacitance of the capture cavity	1 pF	Analytical expressions
$L_{lumped}$	Equivalent lumped element inductance of the capture cavity	1.1 nH	Analytical expressions
$Q_T$	Total quality factor of the capture cavity at the 5.020 GHz operating point where photon capture occurs. Quality factor is dominated by intrinsic damping of the $\text{SiO}_x$ dielectric used in the JPM	1,300	Cavity spectroscopy
$g_2/2\pi$	JPM-cavity coupling strength	44 MHz	Swap spectroscopy between the JPM and capture cavity
$C_s$	JPM shunt capacitor	3.3 pF	JPM spectroscopy
$I_0$	Critical current	1.2 $\mu\text{A}$	JPM spectroscopy and 4-wire resistance measurements of co-fabricated test junctions
$L_g$	Gradiometric loop inductance	1.2 nH	JPM spectroscopy
$C_r$	JPM readout capacitor, used to perform microwave reflectometry	52 fF	Finite element simulations

coming signal, in order to achieve transfer efficiencies approaching 100%. In our setup, photon transfer between the qubit and capture cavities is more complicated. Without an intervening isolator or circulator to damp unwanted reflections, the finite length  $L_0$  of the transmission line admits a standing wave structure with an approximate mode spacing of  $v_p/2L_0 \approx 0.75$  GHz, where  $v_p$  is the phase velocity of propagation in the cable (see Table B.3 for transmission line parameters). In fact, to avoid these issues our initial experiments included an isolator between the qubit and capture cavities, but reached a maximum single-shot measurement fidelity of only  $\sim 50\%$ . We attributed this subpar performance to inline losses and impedance mismatches between samples. To improve our measurement fidelity, our later experiments (described in this report) eliminated the isolator in favor of a single piece of coax with length  $L_0$  chosen to avoid destructive interference in the vicinity of  $\omega_1$  and  $\omega_2$ . It should be noted that when using this approach to transfer energy between cavities, the achievable photon transfer efficiencies depend strongly on  $L_0$ . Using the quite universal circuit simulator (Qucs), we performed a transient analysis based on a simplified version of our experimental setup using the parameters listed in Tables B.1-B.3. In this model, we represented the qubit and capture cavities by their equivalent lumped element representations (valid only near resonance) [14] and analyzed the response of resonator node voltages to an applied resonant drive via  $50\ \Omega$  source coupled to capacitor  $C_0$  [Fig. B.2(b)] allowing  $L_0$  to vary. In our model we represent the coupling losses at both transitions (onto and

off of the two chips) as effective 0.25 dB attenuators. We find that transfer efficiencies  $\sim 25\%$  are possible for our experimental value of  $L_0$ , however, by varying  $L_0$  one can significantly degrade photon transfer efficiency. In Appendix B.8, we describe an alternate method of estimating the photon transfer efficiency based on the calibrated qubit cavity photon occupation of the bright pointer state and an analysis of the JPM tunneling process following photodetection.

## B.6 Window Functions for Pointer State Preparation

Window functions are typically used for pulse shaping qubit drive waveforms in order to suppress spectral content at the 1-2 transition frequency. Since JPM-based qubit state measurement relies on intensity contrast between bright and dark cavity pointer states, windowing functions on the qubit cavity drive were used to suppress microwave energy at the dark pointer state frequency. The Hamming window function was used for cavity pointer state preparation in our experiment. The duration of our cavity pointer state preparation pulse was 780 ns.

## B.7 Theoretical Detection Efficiency

Here we provide a theoretical estimate for the achievable efficiency of the JPM to detect microwave cavity pointer states. We consider the difference in JPM switching probability for the bright pointer state with respect to an ideal dark pointer (qubit cavity at vacuum). The modeling takes into account tunneling of JPM levels between wells and strong relaxation within the shallow left well. Following pointer state transfer, the JPM is tuned into resonance with the capture cavity to probe for photons. At this bias point, the JPM acts as a weakly anharmonic oscillator with an anharmonicity of  $-10$  MHz [Fig. B.5(a)] and an intrinsic relaxation rate of  $\sim 10^8$  s $^{-1}$ . We therefore assume that following photodetection, the JPM levels are populated by a coherent state with mean photon number  $\bar{n}_J$  [see Fig. B.5(b)]. Next, the JPM is biased close to the critical flux  $\Phi_c$ , defined as the bias at which the shallow left well no longer exists. In the neighborhood of this bias, JPM excited states tunnel with high probability [see Fig. B.5(c)]. Using the WKB approximation, we compute the tunneling rate  $\Gamma_n$  of the  $n^{\text{th}}$  level by

$$\Gamma_n = \frac{\omega_0}{2\pi} f_n \exp(-S_n/\hbar). \quad (\text{B.5})$$

Here

$$S_n = \int_{\delta_1}^{\delta_2} \sqrt{2m|E_n - U(\delta)|} d\delta \quad (\text{B.6})$$

is the effective action evaluated at the classical turning points  $\delta_1$  and  $\delta_2$  at energy  $E_n = (n + 1/2)\hbar\omega_0$ , where  $\omega_0$  is the plasma frequency given by Eq. (B.4) and  $m = C_s(\Phi_0/2\pi)^2$  is the effective mass of the JPM phase particle [Fig. B.1(a)]. The numerical factor  $f_n$  is given by

$$f_n = \frac{\sqrt{2\pi}}{n!} \left( \frac{n + \frac{1}{2}}{e} \right)^{n + \frac{1}{2}} \quad (\text{B.7})$$

and provides a small correction due to the anharmonicity [101, 102]. In Fig. B.5(d) we plot tunneling rates for the first four levels of the JPM as a function of  $\Phi_{\text{ext}}/\Phi_c$ . We numerically simulate the population dynamics of the JPM levels under the influence of an applied flux pulse designed to promote tunneling of excited states from the shallow minimum to the global minimum. From the JPM quality factor  $Q \sim 300$ , we estimate the first excited state lifetime  $T_{1,\text{JPM}}$  to be roughly 20 ns near  $\Phi_c$ . Using Fermi's golden rule and the harmonic approximation, we assume that the energy relaxation time of the  $n^{\text{th}}$  excited state is given by  $T_{1,\text{JPM}}/n$ . We consider pulse waveforms with Gaussian rise times of 2 ns and plateau widths of 8 ns; we find that the results are only weakly dependent on the details of the flux pulse waveform. We discretize the time interval of the pulse in steps  $dt \ll 2$  ns; during each time step, we allow the population of the various levels to tunnel with rates calculated using Eq. (B.5). We then redistribute remaining population among the levels in the shallow well according to the relaxation rates of the JPM (assumed to be independent of bias flux). We can then determine switching probability  $P(\bar{n}_J; \Phi_{\text{ext}})$  for various  $\bar{n}_J$  as a function of the

flux pulse amplitude  $\Phi_{\text{ext}}$ ; results are shown in Fig. B.5(e). Detection efficiency is defined as the maximum difference  $P(\bar{n}_J; \Phi_{\text{ext}}) - P(\bar{n}_J = 0; \Phi_{\text{ext}})$  for all  $\Phi_{\text{ext}}$ ; note that our definition assumes a perfect dark pointer state. Results are shown in Fig. B.5(f). In order to achieve detection efficiency of 99%, one must transfer  $\bar{n}_J \sim 8$  photons to the JPM; for smaller photon occupation, the Poisson probability of occupying low lying states in the shallow left well precludes high fidelity measurement. For fixed  $\bar{n}_J$ , improvements in  $T_{1,\text{JPM}}$  from 10 ns to 100 ns yield improvements in fidelity at the level of a few percent [Fig. B.5(g)], but also increase the timescales of both JPM-reset and the depletion interaction.

## B.8 Estimates of Photon Occupation

JPM-based qubit state measurement relies on the transfer of cavity pointer states between the qubit and capture cavities [see Fig. 3.2(a)]. Following pointer state transfer, the state of the capture cavity is detected by the JPM. The short ( $\sim 20$  ns) JPM relaxation time makes it difficult to directly measure the mean photon occupation in the capture cavity [20]; however, we can use Stark spectroscopy to calibrate photon occupation of the qubit cavity [58, 59]. For these experiments, we create a bright pointer state corresponding to the qubit  $|0\rangle$  state in order to circumvent issues associated with qubit energy relaxation. This is in contrast with the results reported in the main text where we drove on the dressed  $|1\rangle$  cavity state to create a bright pointer. The wave-

forms used for Stark calibration are shown in Fig. B.6(a). Stark data shown in Fig. B.6(b) indicate a maximum of 10 photons in the qubit cavity for the range of powers shown. Next, we map our Stark drive (leaving out the spectroscopy and readout drive pulse) onto JPM switching probability. The switching probability saturates at drive powers that correspond to a qubit cavity photon occupation of  $\bar{n}_1 \approx 8$ . Using the model described in Appendix B.7, we can estimate the transfer efficiency between the qubit cavity and the JPM. From our measured JPM switching curves [Fig. 3.3(d)] and our plot of simulated JPM detection inefficiency versus mean photon number  $\bar{n}_J$  [Fig. B.5(g)], we estimate a mean JPM photon occupation of  $\bar{n}_J \sim 4$  during bright pointer state detection. From this, we estimate a transfer efficiency of  $\sim 50\%$  from the qubit cavity to the JPM in our experiments. This number is in reasonable agreement with the transient analysis simulations discussed in Appendix B.5. These efficiencies should not be interpreted as a precise calibration of photon transfer efficiency, but rather as an order of magnitude estimate for the interested reader.

## B.9 Tomography Fits

To estimate the qubit density matrix from the overdetermined tomography described in Fig. 3.4(c) of the main text, we perform a four-parameter fit to a simplistic model of the gate sequence and measurement. The model assumes perfect gates and measurement; any fidelity loss then appears as a less pure density matrix. The fit function

is determined by considering an arbitrary density matrix,

$$\rho = \begin{pmatrix} 1 - \beta & r e^{i\phi} \\ r e^{-i\phi} & \beta \end{pmatrix}, \quad (\text{B.8})$$

which is rotated about an axis  $\theta$  for a time  $t$ , given by

$$R = \exp \left[ \frac{i\pi}{2} \frac{t}{t_\pi} (\sigma_x \cos \theta + \sigma_y \sin \theta) \right], \quad (\text{B.9})$$

where  $t_\pi$  is the  $\pi$ -pulse duration and  $\sigma_x$  and  $\sigma_y$  are the usual Pauli matrices. After the rotation, the qubit occupation is measured,  $M = |1\rangle\langle 1|$ . The average occupation fit function is thus given by

$$P(t, \theta) = \text{Tr}(R\rho R^\dagger M). \quad (\text{B.10})$$

We then fit the tomographic data to the occupation fit function, with fit parameters  $\beta$ ,  $r$ ,  $\phi$ ,  $t_\pi$ , resulting in an estimate of the qubit density matrix. The extracted density matrices for the conditional tomograms shown in Fig. 3.4(c) of the main text are

$$\rho_0 = \begin{pmatrix} 0.91 & 0.02 \\ 0.02 & 0.09 \end{pmatrix} \quad (\text{B.11})$$

and

$$\rho_1 = \begin{pmatrix} 0.31 & 0.01 \\ 0.01 & 0.69 \end{pmatrix}. \quad (\text{B.12})$$

Here, the subscripts 0, 1 correspond to the classical outcome of the initial qubit measurement. We then use the estimated density matrices to compute the overlap (Jozsa) fidelities  $\langle \psi | \rho | \psi \rangle$ , where  $|\psi\rangle$  is the target state [103].

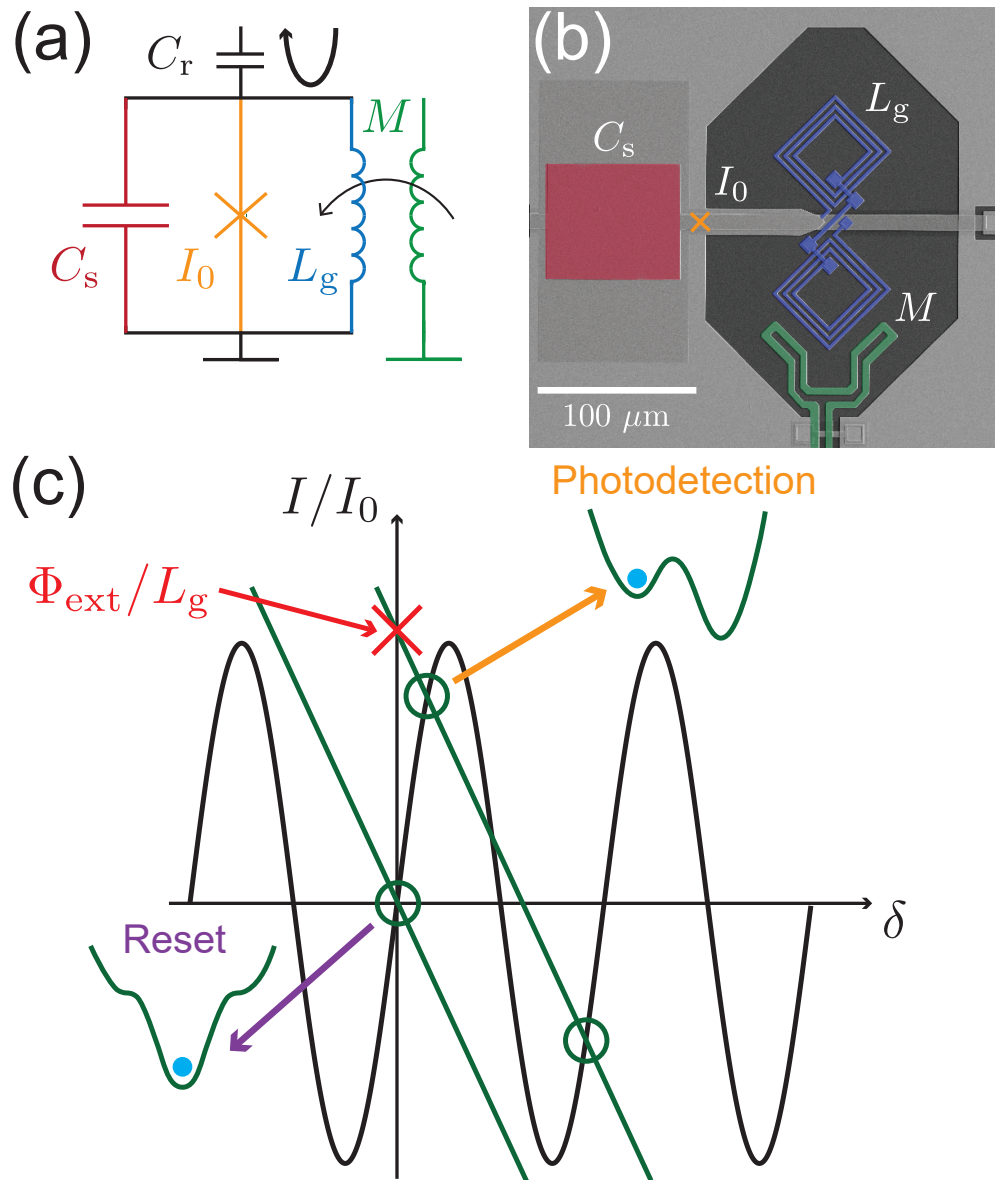


Figure B.1: JPM design. (a) Circuit schematic of the JPM. (b) SEM micrograph of the device. Components are color coded to match the schematic (the JPM reflection capacitor  $C_r$  is not shown). (c) Graphical solution of Eq. (B.2). The slope of the line,  $-1/\beta_L$ , determines the number of local minima (shown as open circles) for a fixed  $\Phi_{\text{ext}}$ . External flux  $\Phi_{\text{ext}}$  controls the  $y$ -intercept, allowing us to move between a single- and double-well regime as needed for JPM reset and photodetection. Black arrows show JPM potentials (with phase particles in blue) for two values of  $\Phi_{\text{ext}}$ .

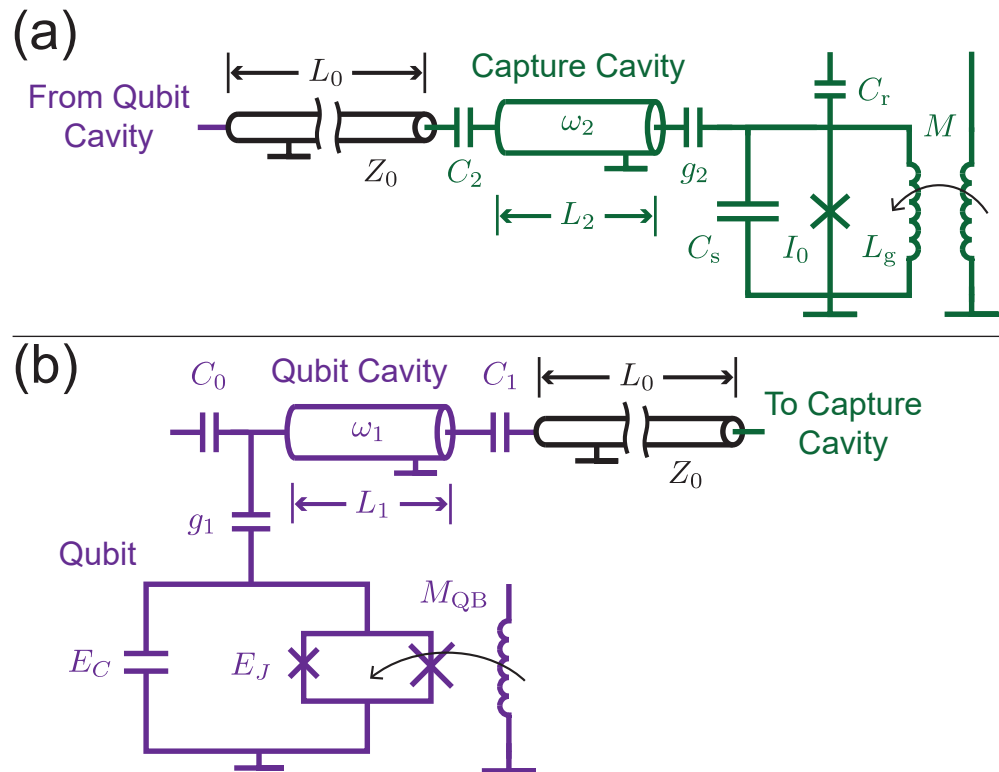


Figure B.2: Circuit schematics. (a) Circuit schematic of the JPM chip with component values listed in Table B.1. (b) Circuit schematic of the qubit chip with component values listed in Table B.2.

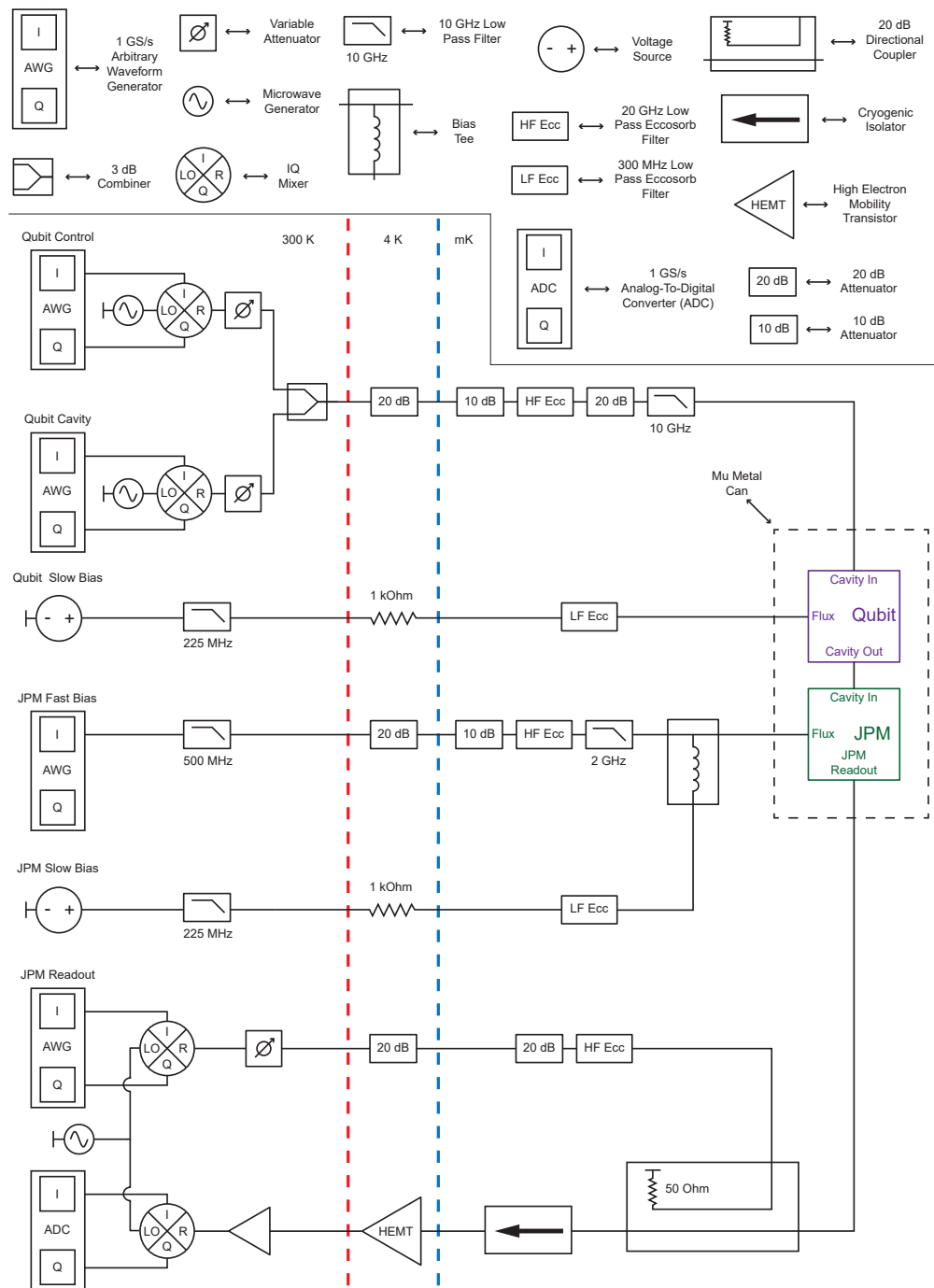


Figure B.3: Experimental setup. Dashed colored lines divide temperature stages. Circuit symbols are defined above. Names above the room temperature AWGs and voltage sources describe their role in the experiment.

Table B.2: Qubit Circuit Parameters

Label	Description	Value	Method of Determination
$C_0$	Qubit cavity input coupling capacitor	1 fF	Finite element simulations
$g_1/2\pi$	Qubit-cavity coupling strength	110 MHz	Qubit and cavity spectroscopy
$E_c/h$	Qubit charging energy	250 MHz	Qubit spectroscopy of the $f_{20}/2$ transition
$E_J/h$	Josephson energy at the upper flux-insensitive sweetspot	9.8 GHz	Qubit spectroscopy of the $f_{10}$ transition
$M_{QB}$	Flux bias mutual inductance	2.2 pH	Cavity spectroscopy versus applied flux
$\omega_1/2\pi$	Fundamental frequency of the half-wave coplanar waveguide resonator	5.020 GHz	Cavity spectroscopy at the upper flux-insensitive sweetspot
$L_1$	Approximate length of the qubit cavity	12 mm	Defined lithographically
$C_{lumped}$	Equivalent lumped element capacitance of the qubit cavity	1 pF	Analytical expressions
$L_{lumped}$	Equivalent lumped element inductance of the qubit cavity	1.1 nH	Analytical expressions
$Q_T$	Total quality factor of the qubit cavity	8,200	Low power cavity spectroscopy measured into a 50 $\Omega$ load
$C_1$	Qubit cavity output coupling capacitor	4.6 fF	High power cavity spectroscopy measurements into a 50 $\Omega$ load on a separate cooldown. Consistent with finite element simulations

Table B.3: Transmission Line Parameters

Label	Description	Value	Method of Determination
$L_0$	Approximate length of the coaxial cable	14 cm	Direct measurement
$Z_0$	Characteristic impedance of the coaxial cable	$50 \Omega$	Manufacturer specification
$v_p$	Propagation velocity of the coaxial cable	$0.7 c$	Manufacturer specification
$\alpha$	Attenuation constant at 5 GHz	55 dB/(100 ft)	Manufacturer specification

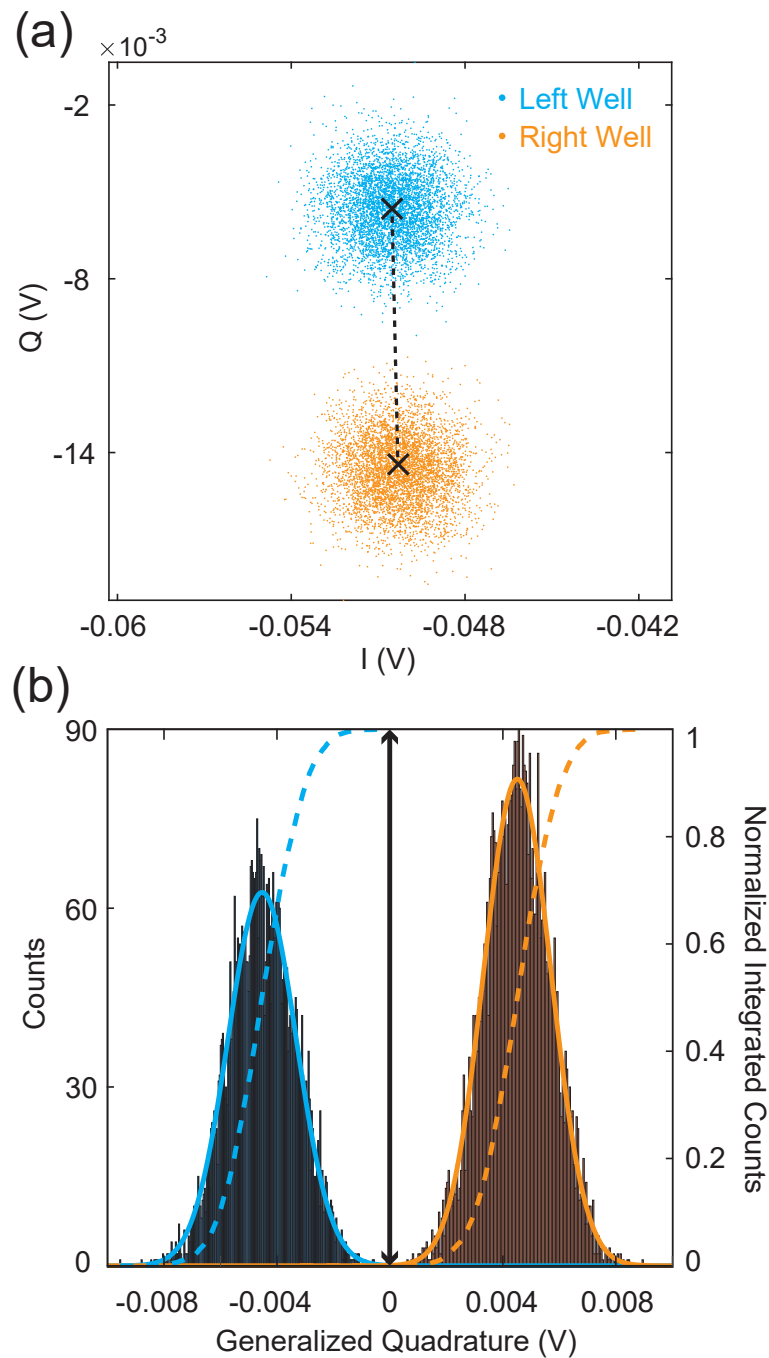


Figure B.4: Interrogation of JPM oscillation state. **(a)** Quadrature amplitudes measured in reflection from a JPM prepared in the two classically distinguishable oscillation states. Single-shot measurement results are projected along the line joining the centroids of the two distributions for the purposes of thresholding. **(b)** Histograms of the JPM readout results. Solid lines are Gaussian fits, and dashed lines are integrated histograms. Thresholding (double arrow) yields a single-shot fidelity of 99.9%; the separation fidelity [44] is 99.98%.

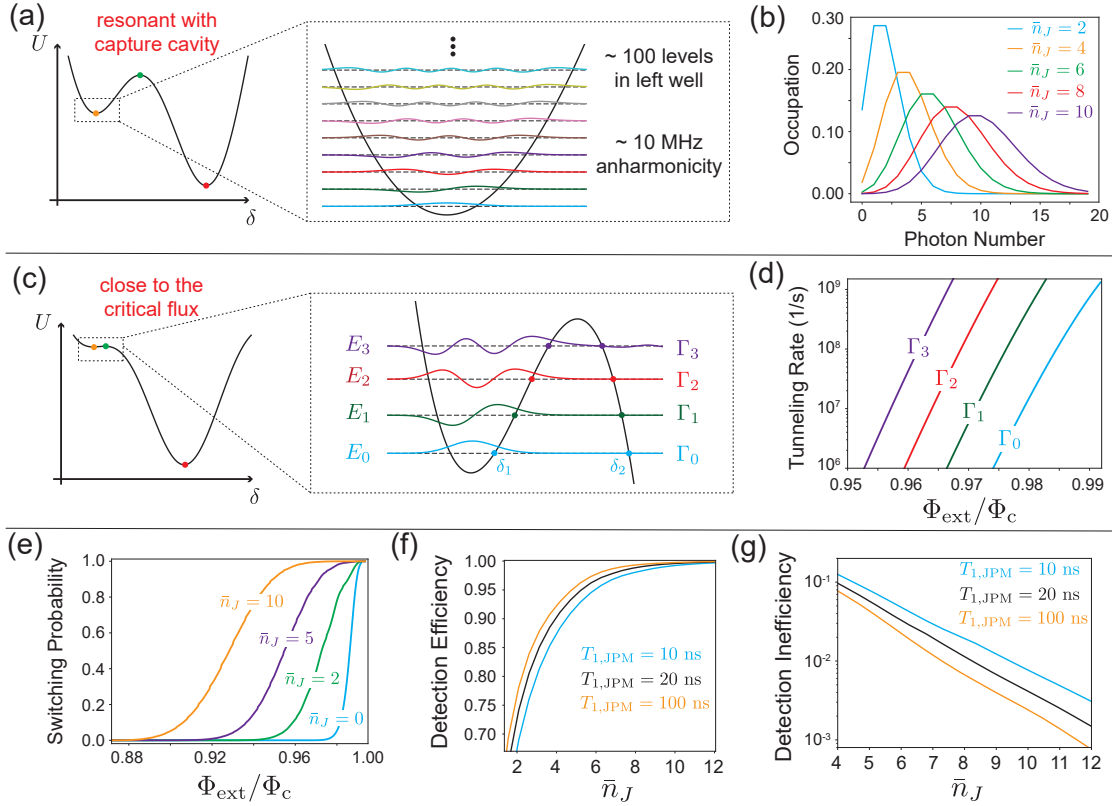


Figure B.5: Theoretically achievable detection efficiency. **(a)** Potential energy landscape of the JPM (with extrema marked as dots) when the plasma frequency of left well is resonant with the capture cavity. The zoomed-in view of the left well indicates that the JPM is a weakly anharmonic oscillator at this bias point. Following JPM interaction with capture cavity, we assume a coherent state with mean photon number  $\bar{n}_J$  is transferred into the JPM. **(b)** Photon state occupation represented in the Fock basis for various mean photon numbers  $\bar{n}_J$ . **(c)** When the JPM is tuned toward  $\Phi_c$ , only a handful of bound states exist in the left well and higher JPM excited states begin to tunnel at non-negligible rates. The classical turning points used to compute tunneling rates [see Eq. (B.6)] are shown as dots. **(d)** Calculated tunneling rates for the first four levels of the JPM as a function of  $\Phi_{\text{ext}}/\Phi_c$ . **(e)** Simulated JPM switching curves versus applied pulse height for various mean photon numbers  $\bar{n}_J$  transferred to the JPM. Switching probability is the fraction of population transferred to the right well after dynamically evolving the rate equations under the influence of an applied flux pulse. **(f)** JPM detection efficiency versus mean photon number  $\bar{n}_J$  for various JPM energy relaxation times. Detection efficiencies in excess of 99% are possible for our detector ( $T_{1,\text{JPM}} \sim 20$  ns) for  $\bar{n}_J \gtrsim 8$ ; for smaller photon occupation, the Poisson probability of occupying low lying states in the shallow left well precludes high fidelity measurement. **(g)** JPM detection inefficiency versus mean photon number  $\bar{n}_J$  for various JPM energy relaxation times. For fixed  $\bar{n}_J$ , improvements in  $T_{1,\text{JPM}}$  from 10 ns to 100 ns yield improvements in fidelity at the level of a few percent.

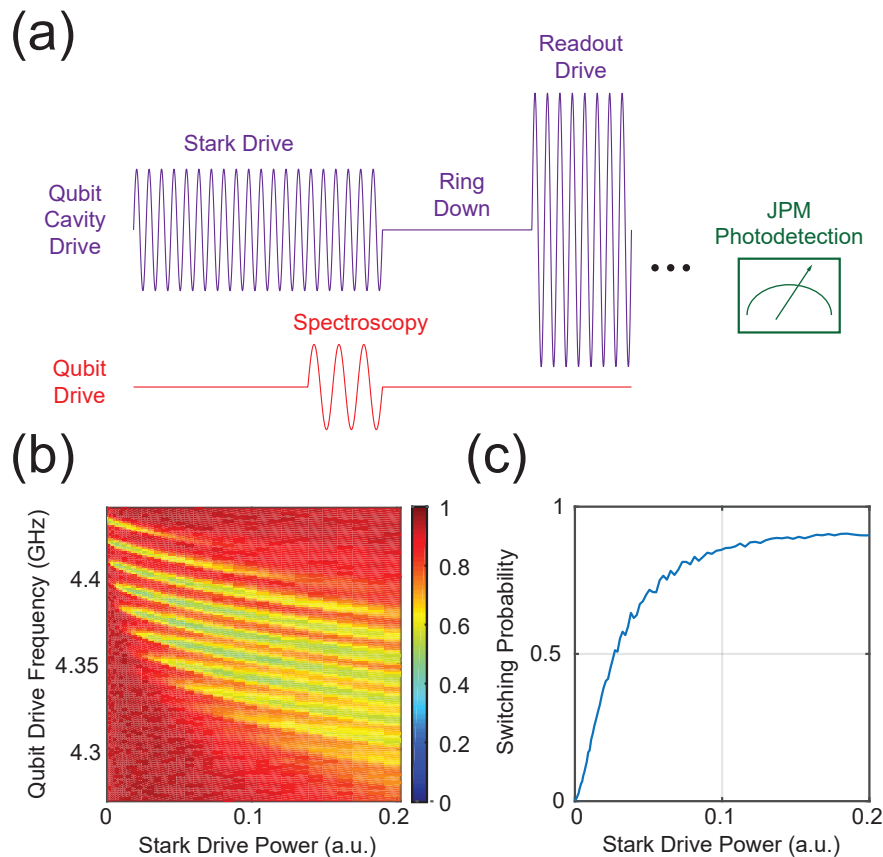


Figure B.6: Stark calibration of photon occupation. **(a)** Pulse sequence used for Stark spectroscopy. Stark drive on the qubit cavity builds up a steady-state photon occupation in that mode. After steady state is reached, a spectroscopy pulse with variable frequency is applied to the qubit. Following the spectroscopic pulse, we wait for the qubit cavity to ring down. Readout drive is then applied to the qubit cavity for pointer state preparation and subsequent JPM photodetection. **(b)** Qubit spectroscopy data versus Stark drive power. Each of the sloped yellow lines corresponds to a distinct photon number state in the qubit cavity. **(c)** JPM switching probability versus Stark drive power. Here we use the Stark drive for pointer state preparation (ring down, readout drive, and spectroscopy pulse are omitted). Parts (b) and (c) permit mapping of JPM switching probability onto photon occupation in the qubit cavity, allowing for an estimate of photon transfer efficiency during bright pointer state detection.



# Appendix C

## Supplementary Materials for JPM

### Experiment II

#### C.1 Sample Fabrication

These samples were fabricated on a high-resistivity ( $\gtrsim 10 \text{ k}\Omega\text{-cm}$ ) silicon substrate with 100 crystal orientation. Prior to base layer deposition, the substrate is dipped in dilute (2%) hydrofluoric acid for one minute to remove native oxide from the surface. We then load the substrate into a dc magnetron sputter tool and deposit a 70 nm-thick film of Nb. The first patterning step defines all Nb features including the control wiring, measurement resonators, qubit capacitors, and spiral inductors. This pattern is then transferred into the Nb using an inductively coupled plasma etcher with  $\text{Cl}_2/\text{BCl}_3$

chemistry. Next, we pattern the sample for liftoff and deposit the insulator used for crossover wiring and parallel-plate capacitors. The 180 nm-thick film of  $\text{SiO}_2$  is deposited using an electron beam evaporator at an oxygen partial pressure  $P_{\text{O}_2} = 10^{-5}$  Torr. In the final photolithography step, we pattern the sample for counterelectrode liftoff. We then deposit a 200 nm-thick Al counterelectrode using an electron beam evaporator after performing an *in situ* ion mill clean to ensure good metallic contact to the base wiring layer. Finally, the JPM and qubit junctions are formed using a Dolan-bridge process [104] involving an MMA/PMMA resist stack patterned using a 100 keV electron-beam writer. The Al- $\text{AlO}_x$ -Al junctions are shadow evaporated in an electron beam evaporator following an *in situ* ion mill clean. This completes the device. Circuit parameters for the chip are listed in Table C.1 with component labels indicated in Fig. 4.2(b).

## C.2 Measurement Setup

The wiring diagram for our measurement setup is shown in Fig. C.4. The waveforms for JPM readout (jr1/2), qubit excitation (xy1/2), and resonator drive are generated via single sideband mixing. Keysight M3202A arbitrary waveform generators (AWGs; 14 bit, 1 GS/s) produce intermediate frequency (IF) signals that are mixed with a local oscillator (LO) to generate shaped pulses at microwave frequencies. The qubit and JPM flux-bias waveforms (z1/2 and jz1/2, respectively) are directly synthesized

using the AWGs. Signal rise times  $\approx 1 - 2$  ns on the  $jz1/2$  waveforms are critical to the success of the qubit measurement sequence [see Fig. 4.4(a)]. The state of the JPM is read out in reflection using a directional coupler. The reflected signal is passed through several stages of isolation and filtering prior to amplification by a high electron mobility transistor (HEMT) amplifier at the 3 K stage of the cryostat. Following additional room temperature amplification, the signal is sent to the RF port of an IQ mixer where it is down converted and digitized using an AlazarTech ATS9870 analog-to-digital converter (ADC; 8 bit, 1 GS/s). Further signal processing and thresholding are performed in software in order to extract the amplitude and phase of the reflected signal. The fidelity with which we measure the flux state of the JPM is better than 99.99%; see Fig. 4.3(b).

### C.3 Stark Calibration

We use the ac Stark effect [58, 59] to estimate photon occupation of the bright and dark pointer states; the pulse sequence is shown in Fig. C.1(a). First, we prepare the qubit in  $|1\rangle$  ( $|0\rangle$ ) through the application of an  $X$ -gate ( $I$ -gate). Next, we drive the measurement resonator at the optimal frequency and power found in Fig. 4.5 but for a variable amount of time, populating the measurement cavity with a mean number of photons  $\bar{n}_r$ . At the end of the Stark drive, a low-power, 500 ns-long Stark spectroscopy pulse is applied to determine the qubit frequency shift  $\Delta\omega_q \equiv \omega_q(\bar{n}_r) - \omega_q(\bar{n}_r = 0)$ . Because the

photon lifetime in the readout cavity is relatively long  $\sim 1.5 \mu\text{s}$ ,  $\bar{n}_r$  can be considered static on the timescale of the spectroscopy experiment. We then reset the resonator using the JPM to deplete the remaining photon occupation (see Appendix C.5). Finally, we measure the qubit using the sequence described in Fig. 4.4. The results are shown in Fig. C.1(b, c). We find that the bright pointer state corresponds to a mean photon occupation of  $\bar{n}_r \approx \Delta\omega_q/2\chi = 27$  photons, where  $\Delta\omega_q/2\pi \approx -200$  MHz at the optimal drive time ( $t_d = 105$  ns) and  $2\chi/2\pi = 7.4$  MHz is the Stark shift per photon. Similarly, the dark pointer acquires a maximum photon occupation  $\bar{n}_r \approx 4$  photons halfway through the drive pulse, but at the end of the resonator drive it returns to a state that is very close to vacuum. For this qubit operation point, the critical photon number  $n_{\text{crit}} = (\Delta_{q,r}/g_{q,r})^2/4 \simeq 13$  photons. We note that these estimates of photon occupation neglect the effect of photon loss during the Stark spectroscopy pulse and the dependence of  $\chi$  on  $\bar{n}_r$ .

## C.4 Fidelity Budget

The nonvanishing  $P(1|0)$  contains contributions both from qubit initialization errors and from imperfect dark pointer state preparation. In order to separately quantify these errors, we performed a series of measurements following active reset of the qubit with resonator drive amplitude swept from its optimal value down to zero [Fig. C.2(a)]; for comparison with Fig. C.1, the calibration described in that figure was performed

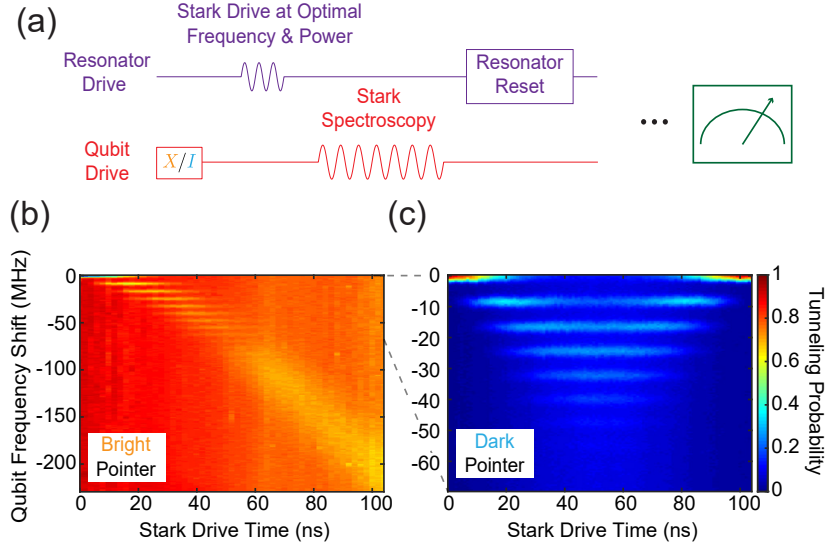


Figure C.1: Stark calibration of pointer states. **(a)** Pulse sequence used for pointer-state calibration. These experiments were performed at the optimal resonator drive amplitude 0.885 arb. units (see Fig. 4.5). For details concerning resonator reset, see Appendix C.5. **(b)** Qubit frequency shift versus Stark drive time for the bright pointer state. **(c)** As in (b), but for the dark pointer state.

at a drive amplitude of 0.885 arb. units. As a result, we can be sure that for drive amplitude  $\lesssim 0.4$  arb. units, the maximum photon occupation of the dark pointer is less than one photon, which is much less than  $n_{\text{crit}}$  over the entire course of driven evolution; at this level of cavity occupation, the dressed resonance corresponding to the qubit  $|0\rangle$  state is well approximated by a linear mode. Therefore, we can attribute all of the tunneling at low resonator drive amplitude to excess  $|1\rangle$  population alone, eliminating contributions caused by the Kerr nonlinearity of the resonator that occur at full drive strength. In Fig. C.2(b, c), we show linear fits to the data of Fig. C.2(a) for resonator drive amplitudes ranging between 0.25-0.4 arb. units. The ratio of the

slopes extracted from these fits gives an estimate of excess  $|1\rangle$  population of 0.3% for nominal preparation of the  $|0\rangle$  state. We attribute the remaining contribution to  $P(1|0)$  to imperfect dark pointer preparation, with infidelity 0.6%.

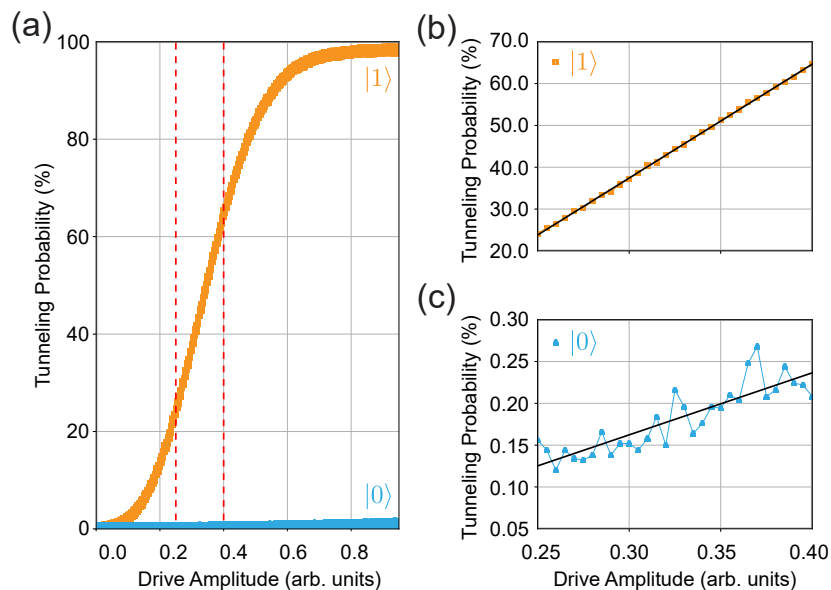


Figure C.2: Estimating excess  $|1\rangle$  population. **(a)** JPM tunneling probability versus resonator drive amplitude for qubits initialized in states  $|0\rangle$  (blue) and  $|1\rangle$  (orange). Based on our Stark calibration at the optimal drive amplitude 0.885 arb. units, we know that for drive amplitudes  $\lesssim 0.4$  arb. units, the maximum photon occupation of the dark pointer is less than one photon ( $\ll n_{\text{crit}}$ ). Therefore, the dressed resonance corresponding to the qubit  $|0\rangle$  state is well approximated by a linear mode during driven evolution. **(b)** Linear fits of JPM tunneling probability versus resonator drive amplitude over the range from 0.25-0.4 arb. units with the qubit prepared in  $|1\rangle$ . **(c)** As in (b), but with the qubit prepared in  $|0\rangle$ .

## C.5 JPM-Assisted Resonator and Qubit Reset

The intrinsic damping of the JPM provides an efficient method for the rapid reset of the resonator and qubit modes. This is accomplished by simply biasing the JPM into resonance with the mode of interest for a brief period of time. The data shown in Fig. C.3(a, b) demonstrate reset of the measurement resonator. In Fig. C.3(a) we plot JPM tunneling probability following photodetection of the bright pointer state after a variable ring-down delay. We observe that passive resonator reset requires  $\simeq 10 \mu\text{s}$  to complete, a consequence of the high- $Q$  measurement resonator used in our design. To accelerate resonator reset, we bias the JPM into resonance with the measurement resonator during the ring-down delay, as shown in Fig. C.3(b). With the JPM and resonator fully hybridized, the energy decay time of the mode is suppressed to around 10 ns, allowing for rapid on-demand depletion of the measurement resonator. We find that JPM-assisted resonator reset is accomplished in under 100 ns.

We extend this idea to qubit reset in the experiments described in Fig. C.3(c, d). In each of these datasets, qubit  $|1\rangle$  occupation is measured after the application of an  $X$ -gate followed by a variable delay. We find that passive reset based on qubit  $T_1$  relaxation requires approximately  $20 \mu\text{s}$ . However, when the JPM is biased into resonance with the qubit during reset, accurate qubit initialization is accomplished in under 100 ns. Throughout the experiments described in this manuscript, JPM-assisted qubit reset was used to suppress excess  $|1\rangle$  state population from a baseline value of

4% to 0.3%.

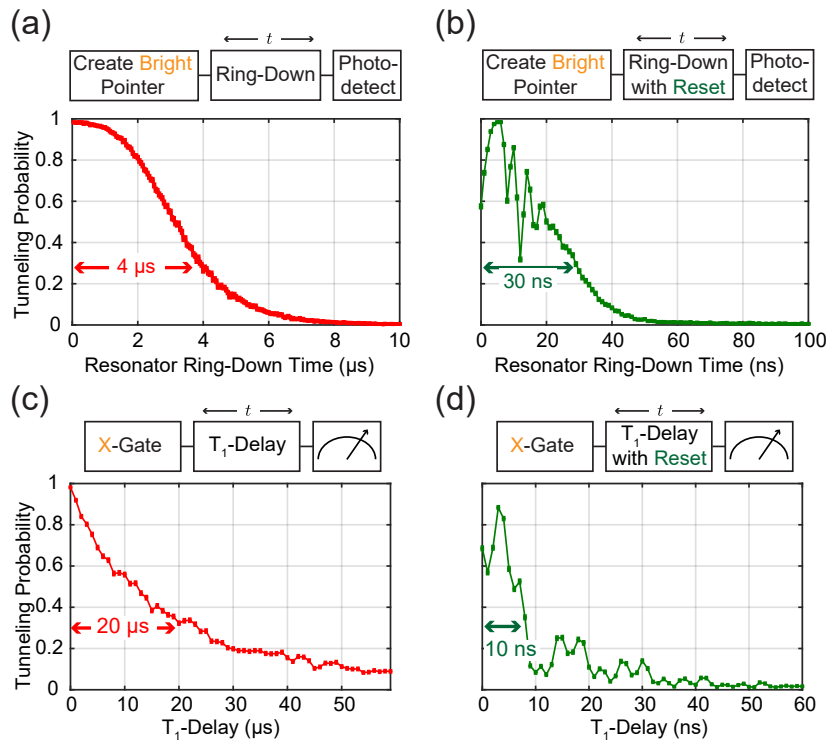


Figure C.3: JPM-assisted resonator and qubit reset. **(a)** JPM photodetection of the bright pointer state after a variable ring-down delay. Passive resonator reset requires around  $10 \mu\text{s}$ , which is too slow for the surface code cycle. **(b)** As in (a), but with the JPM biased into resonance with the resonator  $\omega_r = \omega_j$  during the ring-down delay. Active resonator reset is performed in under 100 ns. **(c)** Qubit  $T_1$  experiment. Passive qubit reset based on intrinsic relaxation processes requires a time of order  $20 \mu\text{s}$ . **(d)** As in (c), but with the JPM and qubit biased into resonance with the measurement resonator ( $\omega_r = \omega_j = \omega_q$ ) during the  $T_1$ -delay. Active qubit reset is performed in under 100 ns.

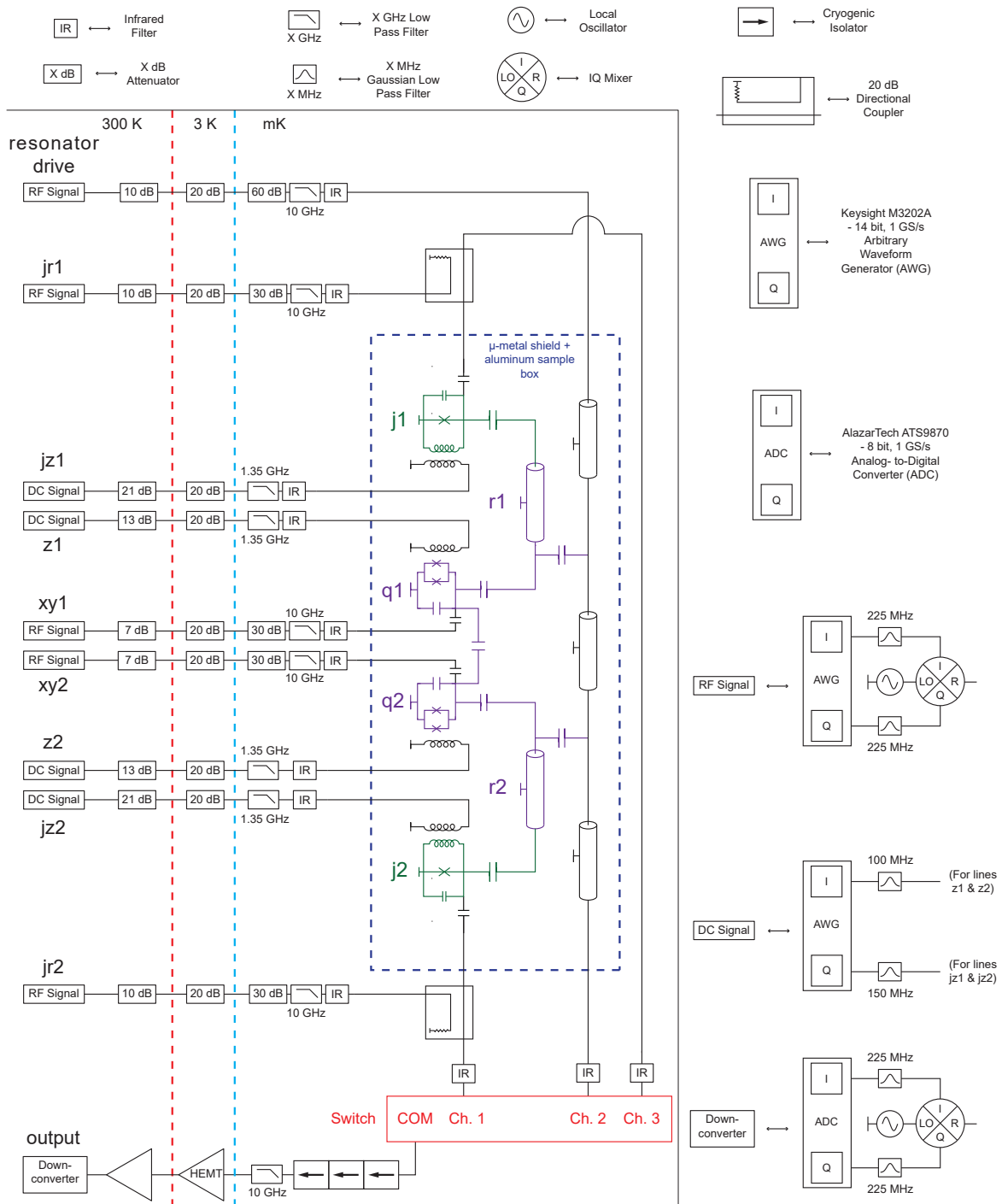


Figure C.4: Wiring diagram of the experiment. Vertical dashed lines divide temperature stages. Circuit components are defined above and to the right. All components within the  $\mu$ -metal shield are made of non-magnetic materials.

Label	Description	Value	Method of Determination
$g_{j_1}/2\pi$	JPM-resonator coupling strength for j1-r1	62 MHz	JPM spectroscopy versus flux
$g_{j_2}/2\pi$	JPM-resonator coupling strength for j2-r2	63 MHz	JPM spectroscopy versus flux
$g_{q_1}/2\pi$	Qubit-resonator coupling strength for q1-r1	90 MHz	Qubit and resonator spectroscopy
$g_{q_2}/2\pi$	Qubit-resonator coupling strength for q2-r2	92 MHz	Qubit and resonator spectroscopy
$\omega_{r_1}/2\pi$	Bare frequency for resonator r1	5.693 GHz	High power resonator spectroscopy with j1 maximally detuned
$\omega_{r_2}/2\pi$	Bare frequency for resonator r2	5.825 GHz	High power resonator spectroscopy with j2 maximally detuned
$\kappa_{r_1}$	Total energy decay rate of resonator r1	$1/(1.53 \mu\text{s})$	VNA measurements with j1 maximally detuned
$\kappa_{r_2}$	Total energy decay rate of resonator r2	$1/(1.51 \mu\text{s})$	VNA measurements with j2 maximally detuned
$g_{q_1, q_2}/2\pi$	Qubit-qubit coupling strength	16 MHz	Qubit spectroscopy about the avoided level crossing (degeneracy at 5.1 GHz)
$T_{1,j}$	Energy relaxation time of the JPM	5 ns	VNA measurements with the JPM detuned from the resonator
$L_j$	Geometric inductance of the JPM	1.3 nH	JPM spectroscopy versus flux
$C_j$	Self-capacitance of the JPM	2.2 pF	JPM spectroscopy versus flux
$C_{jr}$	Reflection capacitor of the JPM	33 fF	JPM spectroscopy versus flux
$I_{0j}$	Critical current of the JPM	$1.4 \mu\text{A}$	JPM spectroscopy versus flux and 4-wire resistance measurements of cofabricated test junctions
$M_j$	Mutual inductance between the JPM and external bias circuitry	4.8 pH	JPM spectroscopy versus flux
$I_{0q}$	Total critical current of the transmon dc SQUID loop	43 nA	Qubit spectroscopy versus flux
$M_q$	Mutual inductance between the qubit and external bias circuitry	1.4 pH	Resonator spectroscopy versus qubit flux
$\eta/2\pi$	Qubit anharmonicity	-225 MHz	Qubit spectroscopy of the $ 0\rangle \rightarrow  1\rangle$ and $ 1\rangle \rightarrow  2\rangle$ transitions
$C_{xy}$	Qubit excitation capacitance	40 aF	Sonnet simulation

Table C.1: Circuit parameters for chip #1. Labels can be found in Fig. 4.2(a, b).

# Bibliography

- [1] J. M. Martinis, K. B. Cooper, R. McDermott, M. Steffen, M. Ansmann, K. D. Osborn, K. Cicak, S. Oh, D. P. Pappas, R. W. Simmonds, and C. C. Yu, *Phys. Rev. Lett.* **95**, 210503 (2005).
- [2] J. Gao, M. Daal, A. Vayonakis, S. Kumar, J. Zmuidzinas, B. Sadoulet, B. A. Mazin, P. K. Day, and H. G. Leduc, *Appl. Phys. Lett.* **92**, 152505 (2008).
- [3] A. Bruno, G. de Lange, S. Asaad, K. L. van der Enden, N. K. Langford, and L. DiCarlo, *Appl. Phys. Lett.* **106**, 182601 (2015).
- [4] A. Dunsworth, A. Megrant, C. Quintana, Z. Chen, R. Barends, B. Burkett, B. Foxen, Y. Chen, B. Chiaro, A. Fowler, R. Graff, E. Jeffrey, J. Kelly, E. Lucero, J. Y. Mutus, M. Neeley, C. Neill, P. Roushan, D. Sank, A. Vainsencher, J. Wenner, T. C. White, and J. M. Martinis, *Appl. Phys. Lett.* **111**, 022601 (2017).
- [5] R. Barends, J. J. A. Baselmans, S. J. C. Yates, J. R. Gao, J. N. Hovenier, and T. M. Klapwijk, *Phys. Rev. Lett.* **100**, 257002 (2008).
- [6] I. Nsanzineza and B. L. T. Plourde, *Phys. Rev. Lett.* **113**, 117002 (2014).
- [7] L. Grünhaupt, N. Maleeva, S. T. Skacel, M. Calvo, F. Levy-Bertrand, A. V. Ustinov, H. Rotzinger, A. Monfardini, G. Catelani, and I. M. Pop, *Phys. Rev. Lett.* **121**, 117001 (2018).
- [8] B. Sarabi, A. N. Ramanayaka, A. L. Burin, F. C. Wellstood, and K. D. Osborn, *Phys. Rev. Lett.* **116**, 167002 (2016).
- [9] J. D. Brehm, A. Bilmes, G. Weiss, A. V. Ustinov, and J. Lisenfeld, *Appl. Phys. Lett.* **111**, 112601 (2017).
- [10] S. E. de Graaf, A. A. Adamyan, T. Lindström, D. Erts, S. E. Kubatkin, A. Y. Tzalenchuk, and A. V. Danilov, *Phys. Rev. Lett.* **118**, 057703 (2017).

- [11] D. M. Pozar, *Microwave Engineering*, 4th ed. (Wiley, 2011).
- [12] K. C. Gupta, R. Garg, I. Bahl, and P. Bhartia, *Microstrip lines and slotlines*, 2nd ed. (Artech House, 1996).
- [13] R. N. Simons, *Coplanar waveguide circuits, components and systems*, 1st ed. (Wiley, 2001).
- [14] M. Göppl, A. Fragner, M. Baur, R. Bianchetti, S. Filipp, J. M. Fink, P. J. Leek, G. Puebla, L. Steffen, and A. Wallraff, *J. Appl. Phys.* **104**, 113904 (2008).
- [15] A. Megrant, C. Neill, R. Barends, B. Chiaro, Y. Chen, L. Feigl, J. Kelly, E. Lucero, M. Mariantoni, P. J. J. O'Malley, D. Sank, A. Vainsencher, J. Wenner, T. C. White, Y. Yin, J. Zhao, C. J. Palmstrøm, J. M. Martinis, and A. N. Cleland, *Appl. Phys. Lett.* **100**, 113510 (2012).
- [16] D. Esteve, M. H. Devoret, and J. M. Martinis, *Phys. Rev. B* **34**, 158 (1986).
- [17] A. A. Houck, J. A. Schreier, B. R. Johnson, J. M. Chow, J. Koch, J. M. Gambetta, D. I. Schuster, L. Frunzio, M. H. Devoret, S. M. Girvin, and R. J. Schoelkopf, *Phys. Rev. Lett.* **101**, 080502 (2008).
- [18] C. C. Gerry and P. L. Knight, *Introductory quantum optics* (Cambridge Univ. Press, 2008).
- [19] S. M. Girvin, Circuit qed: Superconducting qubits coupled to microwave photons, in *Quantum Machines: Measurement and Control of Engineered Quantum Systems* (Oxford University Press, 2014) pp. 113–239.
- [20] M. Hofheinz, E. M. Weig, M. Ansmann, R. C. Bialczak, E. Lucero, M. Neeley, A. D. O'Connell, H. Wang, J. M. Martinis, and A. N. Cleland, *Nature* **454**, 310 (2008).
- [21] M. Hofheinz, H. Wang, M. Ansmann, R. C. Bialczak, E. Lucero, M. Neeley, A. D. O'Connell, D. Sank, J. Wenner, J. M. Martinis, and A. N. Cleland, *Nature* **459**, 546 (2009).
- [22] A. Barone and G. Paternò, *Physics and Applications of the Josephson Effect* (Wiley, 1982).
- [23] V. V. Schmidt, *The Physics of Superconductors: Introduction to Fundamentals and Applications* (Springer Berlin Heidelberg, 1997).
- [24] M. Tinkham, *Introduction to Superconductivity*, 2nd ed. (Dover Publications, 2004).

- [25] M. Devoret, Quantum fluctuations in electrical circuits, in *Fluctuations Quantiques* (Elsevier, 1997) pp. 351–385.
- [26] U. Vool and M. Devoret, *Int. J. Circ. Theor. App.* **45**, 897 (2017).
- [27] J. Koch, T. M. Yu, J. Gambetta, A. A. Houck, D. I. Schuster, J. Majer, A. Blais, M. H. Devoret, S. M. Girvin, and R. J. Schoelkopf, *Phys. Rev. A* **76**, 042319 (2007).
- [28] B. G. Christensen, C. D. Wilen, A. Opremcak, J. Nelson, F. Schlenker, C. H. Zimonick, L. Faoro, L. B. Ioffe, Y. J. Rosen, J. L. DuBois, B. L. T. Plourde, and R. McDermott, *Phys. Rev. B* **100**, 140503 (2019).
- [29] R. Barends, J. Kelly, A. Megrant, D. Sank, E. Jeffrey, Y. Chen, Y. Yin, B. Chiaro, J. Mutus, C. Neill, P. O’Malley, P. Roushan, J. Wenner, T. C. White, A. N. Cleland, and J. M. Martinis, *Phys. Rev. Lett.* **111**, 080502 (2013).
- [30] J. M. Martinis and A. Megrant, *Ucsb final report for the csq program: Review of decoherence and materials physics for superconducting qubits* (2014), [arXiv:1410.5793](https://arxiv.org/abs/1410.5793) .
- [31] E. M. Levenson-Falk, F. Kos, R. Vijay, L. Glazman, and I. Siddiqi, *Phys. Rev. Lett.* **112**, 047002 (2014).
- [32] P. V. Klimov, J. Kelly, Z. Chen, M. Neeley, A. Megrant, B. Burkett, R. Barends, K. Arya, B. Chiaro, Y. Chen, A. Dunsworth, A. Fowler, B. Foxen, C. Gidney, M. Giustina, R. Graff, T. Huang, E. Jeffrey, E. Lucero, J. Y. Mutus, O. Naaman, C. Neill, C. Quintana, P. Roushan, D. Sank, A. Vainsencher, J. Wenner, T. C. White, S. Boixo, R. Babbush, V. N. Smelyanskiy, H. Neven, and J. M. Martinis, *Phys. Rev. Lett.* **121**, 090502 (2018).
- [33] F. W. Strauch, P. R. Johnson, A. J. Dragt, C. J. Lobb, J. R. Anderson, and F. C. Wellstood, *Phys. Rev. Lett.* **91**, 167005 (2003).
- [34] J. M. Martinis and M. R. Geller, *Phys. Rev. A* **90**, 022307 (2014).
- [35] R. Barends, J. Kelly, A. Megrant, A. Veitia, D. Sank, E. Jeffrey, T. C. White, J. Mutus, A. G. Fowler, B. Campbell, Y. Chen, Z. Chen, B. Chiaro, A. Dunsworth, C. Neill, P. O’Malley, P. Roushan, A. Vainsencher, J. Wenner, A. N. Korotkov, A. N. Cleland, and J. M. Martinis, *Nature* **508**, 500 (2014).
- [36] C. Müller, J. H. Cole, and J. Lisenfeld, *Rep. Prog. Phys.* **82**, 124501 (2019).
- [37] Z. Chen, *Metrology of Quantum Control and Measurement in Superconducting Qubits*, *Ph.D. thesis* (2018).

- [38] M. Khezri, *Dispersive Measurement of Superconducting Qubits*, **Ph.D. thesis** (2018).
- [39] A. Opremcak, I. V. Pechenezhskiy, C. Howington, B. G. Christensen, M. A. Beck, E. Leonard, J. Suttle, C. Wilen, K. N. Nesterov, G. J. Ribeill, T. Thorbeck, F. Schlenker, M. G. Vavilov, B. L. T. Plourde, and R. McDermott, **Science** **361**, 1239 (2018).
- [40] A. G. Fowler, M. Mariantoni, J. M. Martinis, and A. N. Cleland, **Phys. Rev. A** **86**, 032324 (2012).
- [41] A. Blais, R.-S. Huang, A. Wallraff, S. M. Girvin, and R. J. Schoelkopf, **Phys. Rev. A** **69**, 062320 (2004).
- [42] I. Siddiqi, R. Vijay, F. Pierre, C. M. Wilson, M. Metcalfe, C. Rigetti, L. Frunzio, and M. H. Devoret, **Phys. Rev. Lett.** **93**, 207002 (2004).
- [43] F. Mallet, F. R. Ong, A. Palacios-Laloy, F. Nguyen, P. Bertet, D. Vion, and D. Esteve, **Nat. Phys.** **5**, 791 (2009).
- [44] E. Jeffrey, D. Sank, J. Y. Mutus, T. C. White, J. Kelly, R. Barends, Y. Chen, Z. Chen, B. Chiaro, A. Dunsworth, A. Megrant, P. J. J. O'Malley, C. Neill, P. Roushan, A. Vainsencher, J. Wenner, A. N. Cleland, and J. M. Martinis, **Phys. Rev. Lett.** **112**, 190504 (2014).
- [45] J. Kelly, R. Barends, A. G. Fowler, A. Megrant, E. Jeffrey, T. C. White, D. Sank, J. Y. Mutus, B. Campbell, Y. Chen, Z. Chen, B. Chiaro, A. Dunsworth, I. C. Hoi, C. Neill, P. J. J. O'Malley, C. Quintana, P. Roushan, A. Vainsencher, J. Wenner, A. N. Cleland, and J. M. Martinis, **Nature** **519**, 66 (2015).
- [46] J. M. Martinis, **npj Quantum Inf.** **1**, 15005 (2015).
- [47] D. Sank, Z. Chen, M. Khezri, J. Kelly, R. Barends, B. Campbell, Y. Chen, B. Chiaro, A. Dunsworth, A. Fowler, E. Jeffrey, E. Lucero, A. Megrant, J. Mutus, M. Neeley, C. Neill, P. J. J. O'Malley, C. Quintana, P. Roushan, A. Vainsencher, T. White, J. Wenner, A. N. Korotkov, and J. M. Martinis, **Phys. Rev. Lett.** **117**, 190503 (2016).
- [48] J. E. Johnson, C. Macklin, D. H. Slichter, R. Vijay, E. B. Weingarten, J. Clarke, and I. Siddiqi, **Phys. Rev. Lett.** **109**, 050506 (2012).
- [49] C. Macklin, K. O'Brien, D. Hover, M. E. Schwartz, V. Bolkhovskiy, X. Zhang, W. D. Oliver, and I. Siddiqi, **Science** **350**, 307 (2015).

- [50] T. Walter, P. Kurpiers, S. Gasparinetti, P. Magnard, A. Potočnik, Y. Salathé, M. Pechal, M. Mondal, M. Oppliger, C. Eichler, and A. Wallraff, *Phys. Rev. Applied* **7**, 054020 (2017).
- [51] D. Ristè, J. G. van Leeuwen, H.-S. Ku, K. W. Lehnert, and L. DiCarlo, *Phys. Rev. Lett.* **109**, 050507 (2012).
- [52] D. Ristè, M. Dukalski, C. A. Watson, G. de Lange, M. J. Tiggelman, Y. M. Blanter, K. W. Lehnert, R. N. Schouten, and L. DiCarlo, *Nature* **502**, 350 (2013).
- [53] L. C. G. Govia, E. J. Pritchett, C. Xu, B. L. T. Plourde, M. G. Vavilov, F. K. Wilhelm, and R. McDermott, *Phys. Rev. A* **90**, 062307 (2014).
- [54] Y.-F. Chen, D. Hover, S. Sendelbach, L. Maurer, S. T. Merkel, E. J. Pritchett, F. K. Wilhelm, and R. McDermott, *Phys. Rev. Lett.* **107**, 217401 (2011).
- [55] M. D. Hutchings, J. B. Hertzberg, Y. Liu, N. T. Bronn, G. A. Keefe, M. Brink, J. M. Chow, and B. L. T. Plourde, *Phys. Rev. Applied* **8**, 044003 (2017).
- [56] M. Steffen, M. Ansmann, R. McDermott, N. Katz, R. C. Bialczak, E. Lucero, M. Neeley, E. M. Weig, A. N. Cleland, and J. M. Martinis, *Phys. Rev. Lett.* **97**, 050502 (2006).
- [57] J. Wenner, Y. Yin, Y. Chen, R. Barends, B. Chiaro, E. Jeffrey, J. Kelly, A. Megrant, J. Y. Mutus, C. Neill, P. J. J. O'Malley, P. Roushan, D. Sank, A. Vainsencher, T. C. White, A. N. Korotkov, A. N. Cleland, and J. M. Martinis, *Phys. Rev. Lett.* **112**, 210501 (2014).
- [58] D. I. Schuster, A. Wallraff, A. Blais, L. Frunzio, R.-S. Huang, J. Majer, S. M. Girvin, and R. J. Schoelkopf, *Phys. Rev. Lett.* **94**, 123602 (2005).
- [59] D. I. Schuster, A. A. Houck, J. A. Schreier, A. Wallraff, J. M. Gambetta, A. Blais, L. Frunzio, J. Majer, B. Johnson, M. H. Devoret, S. M. Girvin, and R. J. Schoelkopf, *Nature* **445**, 515 (2007).
- [60] K. B. Cooper, M. Steffen, R. McDermott, R. W. Simmonds, S. Oh, D. A. Hite, D. P. Pappas, and J. M. Martinis, *Phys. Rev. Lett.* **93**, 180401 (2004).
- [61] R. McDermott, R. W. Simmonds, M. Steffen, K. B. Cooper, K. Cicak, K. D. Osborn, S. Oh, D. P. Pappas, and J. M. Martinis, *Science* **307**, 1299 (2005).
- [62] A. P. Sears, A. Petrenko, G. Catelani, L. Sun, H. Paik, G. Kirchmair, L. Frunzio, L. I. Glazman, S. M. Girvin, and R. J. Schoelkopf, *Phys. Rev. B* **86**, 180504 (2012).

- [63] F. Yan, S. Gustavsson, A. Kamal, J. Birenbaum, A. P. Sears, D. Hover, T. J. Gudmundsen, D. Rosenberg, G. Samach, S. Weber, J. L. Yoder, T. P. Orlando, J. Clarke, A. J. Kerman, and W. D. Oliver, *Nat. Commun.* **7**, 12964 (2016).
- [64] D. T. McClure, H. Paik, L. S. Bishop, M. Steffen, J. M. Chow, and J. M. Gambetta, *Phys. Rev. Applied* **5**, 011001 (2016).
- [65] A. Lupascu, C. J. M. Verwijs, R. N. Schouten, C. J. P. M. Harmans, and J. E. Mooij, *Phys. Rev. Lett.* **93**, 177006 (2004).
- [66] A. Herr, A. Fedorov, A. Shnirman, E. Il'ichev, and G. Schön, *Supercond. Sci. Tech.* **20**, S450 (2007).
- [67] K. G. Fedorov, A. V. Shcherbakova, M. J. Wolf, D. Beckmann, and A. V. Ustinov, *Phys. Rev. Lett.* **112**, 160502 (2014).
- [68] R. McDermott, M. G. Vavilov, B. L. T. Plourde, F. K. Wilhelm, P. J. Liebermann, O. A. Mukhanov, and T. A. Ohki, *Quantum Sci. Technol.* **3**, 024004 (2018).
- [69] A. Opremcak, C. H. Liu, C. Wilen, K. Okubo, B. G. Christensen, D. Sank, T. C. White, A. Vainsencher, M. Giustina, A. Megrant, B. Burkett, B. L. T. Plourde, and R. McDermott, High-fidelity measurement of a superconducting qubit using an on-chip microwave photon counter (2020), [arXiv:2008.02346](https://arxiv.org/abs/2008.02346) .
- [70] J. Heinsoo, C. K. Andersen, A. Remm, S. Krinner, T. Walter, Y. Salathé, S. Gasparinetti, J.-C. Besse, A. Potočnik, A. Wallraff, and C. Eichler, *Phys. Rev. Applied* **10**, 034040 (2018).
- [71] J. Y. Mutus, T. C. White, R. Barends, Y. Chen, Z. Chen, B. Chiaro, A. Dunsworth, E. Jeffrey, J. Kelly, A. Megrant, C. Neill, P. J. J. O'Malley, P. Roushan, D. Sank, A. Vainsencher, J. Wenner, K. M. Sundqvist, A. N. Cleland, and J. M. Martinis, *Appl. Phys. Lett.* **104**, 263513 (2014).
- [72] K. M. Sliwa, M. Hatridge, A. Narla, S. Shankar, L. Frunzio, R. J. Schoelkopf, and M. H. Devoret, *Phys. Rev. X* **5**, 041020 (2015).
- [73] F. Lecocq, L. Ranzani, G. A. Peterson, K. Cicak, R. W. Simmonds, J. D. Teufel, and J. Aumentado, *Phys. Rev. Applied* **7**, 024028 (2017).
- [74] B. J. Chapman, E. I. Rosenthal, J. Kerckhoff, B. A. Moores, L. R. Vale, J. A. B. Mates, G. C. Hilton, K. Lalumière, A. Blais, and K. W. Lehnert, *Phys. Rev. X* **7**, 041043 (2017).

- [75] T. Thorbeck, S. Zhu, E. Leonard, R. Barends, J. Kelly, J. M. Martinis, and R. McDermott, *Phys. Rev. Applied* **8**, 054007 (2017).
- [76] B. Abdo, N. T. Bronn, O. Jinka, S. Olivadese, A. D. Córcoles, V. P. Adiga, M. Brink, R. E. Lake, X. Wu, D. P. Pappas, and J. M. Chow, *Nat. Commun.* **10**, 3154 (2019).
- [77] A. Eddins, J. M. Kreikebaum, D. M. Toyli, E. M. Levenson-Falk, A. Dove, W. P. Livingston, B. A. Levitan, L. C. G. Govia, A. A. Clerk, and I. Siddiqi, *Phys. Rev. X* **9**, 011004 (2019).
- [78] A. Wallraff, D. I. Schuster, A. Blais, L. Frunzio, J. Majer, M. H. Devoret, S. M. Girvin, and R. J. Schoelkopf, *Phys. Rev. Lett.* **95**, 060501 (2005).
- [79] F. Motzoi, J. M. Gambetta, P. Reberntrost, and F. K. Wilhelm, *Phys. Rev. Lett.* **103**, 110501 (2009).
- [80] E. Lucero, J. Kelly, R. C. Bialczak, M. Lenander, M. Mariantoni, M. Neeley, A. D. O’Connell, D. Sank, H. Wang, M. Weides, J. Wenner, T. Yamamoto, A. N. Cleland, and J. M. Martinis, *Phys. Rev. A* **82**, 042339 (2010).
- [81] Z. Chen, J. Kelly, C. Quintana, R. Barends, B. Campbell, Y. Chen, B. Chiaro, A. Dunsworth, A. G. Fowler, E. Lucero, E. Jeffrey, A. Megrant, J. Mutus, M. Neeley, C. Neill, P. J. J. O’Malley, P. Roushan, D. Sank, A. Vainsencher, J. Wenner, T. C. White, A. N. Korotkov, and J. M. Martinis, *Phys. Rev. Lett.* **116**, 020501 (2016).
- [82] M. Khezri, E. Mlinar, J. Dressel, and A. N. Korotkov, *Phys. Rev. A* **94**, 012347 (2016).
- [83] M. Khezri and A. N. Korotkov, *Phys. Rev. A* **96**, 043839 (2017).
- [84] J. Gambetta, W. A. Braff, A. Wallraff, S. M. Girvin, and R. J. Schoelkopf, *Phys. Rev. A* **76**, 012325 (2007).
- [85] E. Magesan, J. M. Gambetta, B. R. Johnson, C. A. Ryan, J. M. Chow, S. T. Merkel, M. P. da Silva, G. A. Keefe, M. B. Rothwell, T. A. Ohki, M. B. Ketchen, and M. Steffen, *Phys. Rev. Lett.* **109**, 080505 (2012).
- [86] J. M. Martinis, S. Nam, J. Aumentado, K. M. Lang, and C. Urbina, *Phys. Rev. B* **67**, 094510 (2003).
- [87] J. Bylander, S. Gustavsson, F. Yan, F. Yoshihara, K. Harrabi, G. Fitch, D. G. Cory, Y. Nakamura, J.-S. Tsai, and W. D. Oliver, *Nat. Phys.* **7**, 565 (2011).

- [88] F. Yan, D. Campbell, P. Krantz, M. Kjaergaard, D. Kim, J. L. Yoder, D. Hover, A. Sears, A. J. Kerman, T. P. Orlando, S. Gustavsson, and W. D. Oliver, *Phys. Rev. Lett.* **120**, 260504 (2018).
- [89] C. K. Andersen, A. Remm, S. Lazar, S. Krinner, J. Heinsoo, J.-C. Besse, M. Gabureac, A. Wallraff, and C. Eichler, *npj Quantum Inf.* **5**, 69 (2019).
- [90] C. K. Andersen, A. Remm, S. Lazar, S. Krinner, N. Lacroix, G. J. Norris, M. Gabureac, C. Eichler, and A. Wallraff, *Nat. Phys.* (2020).
- [91] M. Lenander, H. Wang, R. C. Bialczak, E. Lucero, M. Mariani, M. Neeley, A. D. O’Connell, D. Sank, M. Weides, J. Wenner, T. Yamamoto, Y. Yin, J. Zhao, A. N. Cleland, and J. M. Martinis, *Phys. Rev. B* **84**, 024501 (2011).
- [92] J. Wenner, Y. Yin, E. Lucero, R. Barends, Y. Chen, B. Chiaro, J. Kelly, M. Lenander, M. Mariani, A. Megrant, C. Neill, P. J. J. O’Malley, D. Sank, A. Vainsencher, H. Wang, T. C. White, A. N. Cleland, and J. M. Martinis, *Phys. Rev. Lett.* **110**, 150502 (2013).
- [93] U. Patel, I. V. Pechenezhskiy, B. L. T. Plourde, M. G. Vavilov, and R. McDermott, *Phys. Rev. B* **96**, 220501 (2017).
- [94] R.-P. Riwar and G. Catelani, *Phys. Rev. B* **100**, 144514 (2019).
- [95] F. Arute, K. Arya, R. Babbush, D. Bacon, J. C. Bardin, R. Barends, R. Biswas, S. Boixo, F. G. S. L. Brandao, D. A. Buell, B. Burkett, Y. Chen, Z. Chen, B. Chiaro, R. Collins, W. Courtney, A. Dunsworth, E. Farhi, B. Foxen, A. Fowler, C. Gidney, M. Giustina, R. Graff, K. Guerin, S. Habegger, M. P. Harrigan, M. J. Hartmann, A. Ho, M. Hoffmann, T. Huang, T. S. Humble, S. V. Isakov, E. Jeffrey, Z. Jiang, D. Kafri, K. Kechedzhi, J. Kelly, P. V. Klimov, S. Knysh, A. Korotkov, F. Kostritsa, D. Landhuis, M. Lindmark, E. Lucero, D. Lyakh, S. Mandrà, J. R. McClean, M. McEwen, A. Megrant, X. Mi, K. Michielsen, M. Mohseni, J. Mutus, O. Naaman, M. Neeley, C. Neill, M. Y. Niu, E. Ostby, A. Petukhov, J. C. Platt, C. Quintana, E. G. Rieffel, P. Roushan, N. C. Rubin, D. Sank, K. J. Satzinger, V. Smelyanskiy, K. J. Sung, M. D. Trevithick, A. Vainsencher, B. Villalonga, T. White, Z. J. Yao, P. Yeh, A. Zalcman, H. Neven, and J. M. Martinis, *Nature* **574**, 505 (2019).
- [96] C. Howington, A. Opremcak, R. McDermott, A. Kirichenko, O. A. Mukhanov, and B. L. T. Plourde, *IEEE Trans. Appl. Supercond.* **29**, 1 (2019).
- [97] R. McDermott and M. G. Vavilov, *Phys. Rev. Applied* **2**, 014007 (2014).

- [98] E. Leonard, M. A. Beck, J. Nelson, B. G. Christensen, T. Thorbeck, C. Howington, A. Opremcak, I. V. Pechenezhskiy, K. Dodge, N. P. Dupuis, M. D. Hutchings, J. Ku, F. Schlenker, J. Suttle, C. Wilen, S. Zhu, M. G. Vavilov, B. L. T. Plourde, and R. McDermott, *Phys. Rev. Applied* **11**, 014009 (2019).
- [99] G. Burkard, R. H. Koch, and D. P. DiVincenzo, *Phys. Rev. B* **69**, 064503 (2004).
- [100] D. T. Sank, *Fast, Accurate State Measurement in Superconducting Qubits*, *Ph.D. thesis* (2014).
- [101] K. Likharev, *Physica B+C* **108**, 1079 (1981).
- [102] J. Lisenfeld, *Experiments On Superconducting Josephson Phase Quantum Bits*, *Ph.D. thesis* (2007).
- [103] R. Jozsa, *J. Mod. Opt.* **41**, 2315 (1994).
- [104] G. J. Dolan, *Appl. Phys. Lett.* **31**, 337 (1977).